Space Sci Rev (2021) 217:38
https://doi.org/10.1007/s11214-021-00814-x

Current Sheets, Plasmoids and Flux Ropes in the Heliosphere

Part I. 2-D or not 2-D? General and Observational Aspects

O. Khabarova[1,2] · O. Malandraki[3] · H. Malova[2,4] · R. Kislov[2] · A. Greco[5] · R. Bruno[6] · O. Pezzi[7,8,9] · S. Servidio[5] · Gang Li[10] · W. Matthaeus[11] · J. Le Roux[10] · N.E. Engelbrecht[12] · F. Pecora[5] · L. Zelenyi[2] · V. Obridko[1] · V. Kuznetsov[1]

Received: 7 October 2020 / Accepted: 3 March 2021

Abstract Recent accumulation of a critical mass of observational material from different spacecraft complete with the enhanced abilities of numerical methods have led to a boom of studies revealing the high complexity of processes occurring in the heliosphere. Views on the solar wind filling the interplanetary medium have dramatically developed from the beginning of the space era. A 2-D picture of the freely expanding solar corona and non-interacting solar wind structures described as planar or spherically-symmetric objects has dominated for decades. Meanwhile, the scientific community gradually moved to a modern understanding of the importance of the 3-D nature of heliospheric processes and their studies via MHD/kinetic simulations, as well as observations of large-scale flows and streams both in situ and remotely, in white light and/or via interplanetary scintillations. The new 3-D approach has provided an opportunity to understand the dynamics of heliospheric structures

✉ O. Khabarova
habarova@izmiran.ru

1 Pushkov Institute of Terrestrial Magnetism, Ionosphere and Radio Wave Propagation of the Russian Academy of Sciences (IZMIRAN), Moscow, 108840, Russia

2 Space Research Institute (IKI) RAS, Moscow, 117997, Russia

3 IAASARS, National Observatory of Athens, Penteli, Greece

4 Scobeltsyn Nuclear Physics Institute of Lomonosov Moscow State University, Moscow, 119991, Russia

5 Dipartimento di Fisica, Università della Calabria, 87036 Rende (CS), Italy

6 Istituto di Astrofisica e Planetologia Spaziali, Istituto Nazionale di Astrofisica (IAPS-INAF), Roma, Italy

7 Gran Sasso Science Institute (GSSI), Viale F. Crispi 7, 67100 L'Aquila, Italy

8 INFN, Laboratori Nazionali del Gran Sasso (LNGS), 67100 Assergi, L'Aquila, Italy

9 Istituto per la Scienza e Tecnologia dei Plasmi, CNR, Via Amendola 122/D, 70126 Bari, Italy

10 Center for Space Plasma and Aeronomic Research (CSPAR) and Department of Space Science, University of Alabama in Huntsville, Huntsville, AL 35805, USA

11 Department of Physics and Astronomy, University of Delaware, Newark, DE 19716, USA

12 Centre for Space Research, North-West University, Potchefstroom, 2522, South Africa

and processes that could not even be imagined before within the 2-D paradigm. In this review, we highlight a piece of the puzzle, showing the evolution of views on processes related to current sheets, plasmoids, blobs and flux ropes of various scales and origins in the heliosphere. The first part of the review focuses on introducing these plasma structures, discussing their key properties, and paying special attention to their observations in different space plasmas.

Keywords Current sheets · Plasmoids · Flux ropes · Magnetic islands · Magnetic reconnection · Particle acceleration

1 Introduction

This review discusses an important point of applicability of the established two-dimensional (2-D) views on heliospheric plasma structures to studies of current sheets and plasmoids, which are universal in their occurrence in all kinds of cosmic plasma (e.g., Gosling et al. 1977, 2004, 2005a, 2005b, 2006; Crooker et al. 2003, 2004; Owens et al. 2013). The heliosphere itself is an undoubtedly 3-D object, as well as its largest non-planar structures such as the heliospheric current sheet (HCS), interplanetary coronal mass ejections (ICMEs), and corotating or stream interaction regions (CIRs/SIRs). The last decade's fast growth in computational power and the development of improved numerical methods have allowed reconstructions of close-to-reality situations that occur in the interplanetary medium and provided new insights as to the importance of a 3-D consideration of heliospheric processes of different origins and scales.

Historically, the HCS, ICMEs and CIRs/SIRs became the first objects to which the 3-D approach was applied because of their large scales and obviously complex nature (Suess 1988; Gosling and Pizzo 1999; Odstrčil and Pizzo 1999; Gopalswamy et al. 2009; Kataoka et al. 2009; Owens 2009; Riley 2007; Vandas et al. 2010; Lugaz and Roussev 2011). Their earliest studies were mainly restricted to MHD theories downgraded to 2-D or even 1-D for the simplification (e.g., Oughton et al. 2017). A 2-D paradigm adopted by both theorists and observers suggested that all structures and flows/streams in the solar wind expand radially and freely, not interacting with each other. Therefore, the third dimension was thought not necessary to consider or mention since the large-scale structures were supposed to be either planar or spherically-symmetric. The corresponding 2-D sketches of observed solar wind structures either reflected an intuitive understanding of processes occurring in the heliosphere or referred to the dominant theories of the time. The insufficiency of the observational in situ data was critical in the beginning of the space era, and, as a result, the interpretation of observations in the solar wind had been governed by theory for decades. Large-scale ICME-ICME or ICME-SIR interactions, processes related to the significantly disrupted or rippled HCS, as well as dynamical processes associated with smaller-scale non-planar structures had not been satisfactorily studied before 2010th, as their occurrence and dynamics could not be described and sometimes even imagined in 2-D.

Nowadays, the 2-D approach co-exists with understanding of the necessity of detailed consideration of 3-D effects. Wide opportunities to explore the 3-D complexity and dynamics of both large- and smaller-scale objects observed in the heliosphere began to appear approximately 15 years ago owing to (i) accumulation of a critical mass of single-point observations in space, (ii) carrying on simultaneous multi-spacecraft in situ observations that allow for tracking of propagating plasma objects, and (iii) remote observations/tomography

of the interplanetary plasma through the analysis of interplanetary scintillations and heliospheric white light imagery (see Sect. 2.1.2).

It should be noted that new techniques, such as (iii), require time to be learnt and widely used in the community. Partially because of this, there is still a historically-grounded tendency to think of heliospheric processes in 2-D. The 2-D approximation is sometimes justified due to the scale and the topology or specific conditions of the particular processes studied. A minimal difference between the results of the 2-D and 3-D analysis is expected to be found in such cases. A notable example is a familiar use of a 2-D paradigm for magnetic reconnection in the simplest magnetic topologies, which can be useful for understanding related basic processes at the descriptive and valuation levels. Meanwhile, it has been found that Petschek- and/or Sweet–Parker magnetic reconnection rarely develops in real plasmas, quickly transforming into 3-D turbulent reconnection (Lazarian and Vishniac 1999; Uzdensky and Kulsrud 2000; Kowal et al. 2012; Lazarian et al. 2012, 2020; Wan et al. 2014; Uzdensky and Loureiro 2016; Bahauddin et al. 2020; Fleishman et al. 2020). Recent theoretical and observational studies in this area suggest that turbulent or stochastic magnetic reconnection dominates in space plasmas, analogous to processes observed in corresponding laboratory experiments (e.g., Gekelman et al. 2012, 2014, 2016, 2018; Lazarian et al. 2020).

The latter is not just a coincidence. It is known that although the difference between key plasma/magnetic field parameters in the heliosphere and laboratory can sometimes reach tens of orders of magnitude, the plasmas can be characterized by dimensionless parameters of surprisingly similar values (Vaivads et al. 2012). For example, the laboratory plasmas, the magnetopause, the magnetospheric plasma sheet, the outer corona, and the solar wind possess comparable ratios of the plasma frequency/gyrofrequency versus the thermal energy/magnetic energy (see Fig. 3 of Vaivads et al. 2012). This means that processes observed in space plasmas and laboratories can be described by the same theories, and we can learn from laboratory experiments, applying corresponding results to the interpretation of some effects in the heliospheric plasma, which will be discussed in this review.

One of these processes is the magnetic reconnection ubiquitously occurring in space and laboratory plasmas. Owing to magnetic reconnection, magnetic energy can be converted into other forms (waves, heat, and the energy of accelerated particles) (e.g., Guo et al. 2020). This makes magnetic reconnection the philosophers' stone that allows one to explain energy transfer and various dynamical effects associated with current sheets observed in the heliosphere. The main structures associated with this fundamental process in the solar wind and in the magnetospheres of planets are reconnecting current sheets and reconnection-borne plasmoids, blobs and flux ropes. The delicacy of the 2-D picture of reconnection in a 3D world becomes very clear when examining the relative behavior of field lines and current sheets in 3-D. When magnetic reconnection occurs at current sheets in the presence of a guide field, the condition for this is that the magnetic field components form an X-point. However, one finds that field lines and current sheets that coincide in one plane tend to systematically depart from one another in nearby planes further along the guide field (Wan et al. 2014; Rappazzo et al. 2017). This purely 3-D effect represents a weak departure from 2D, but strongly modulates reconnection rates (Wan et al. 2014).

It should be noted that the discussed objects can have a solar origin too. For example, plasmoids/blobs/magnetic bubbles/flux ropes as well as CME-associated current sheets can be formed in the solar corona and drift within the expanding solar wind further from the Sun (e.g., Bemporad 2008, 2011; Higginson and Lynch 2018; Lee et al. 2020), while the largest current sheet in the heliosphere, the heliospheric current sheet (HCS), is formed in the solar wind because of the dipole structure of the dominant magnetic field of the Sun

(e.g., Weber and Davis 1967; Wilcox 1968; Veselovsky et al. 2002; Czechovski et al. 2010). The difference between the solar- and local-borne structures observed in the solar wind is mainly in typical sizes (elongation) and life-times. Since the width of current sheets of different origin is the same (Malova et al. 2017), local dynamical processes such as magnetic reconnection and particle acceleration occur at them in the same manner.

Plasmoids/blobs/magnetic bubbles/flux ropes are 3-D structures that are often described in 2-D as magnetic islands. Most of current sheets are also non-planar at either large scales (because of their non-planar source at the Sun) or small-scales (because they are rippled and distorted by instabilities, magnetic reconnection and the consequent ongoing formation of plasmoids). However, all of them are predominantly treated as 2-D planar sheets in the literature. The question arises: Can we treat all these objects as 2-D knowing that those are actually 3-D? Can we successfully describe not only their properties but also effects associated with them, i.e. magnetic reconnection and particle acceleration, remaining within a framework of the 2-D paradigm, or will some important features be lost?

All the structures discussed possess a wide range of typical scales from the energy containing to kinetic ones, and dynamical processes occurring in them link the stream propagation, magnetic reconnection, particle energization and turbulence. The similarity of many effects associated with plasmoids/blobs/magnetic bubbles (in 3-D) or magnetic islands (in 2-D) and current sheets formed in very different plasmas but in similar topological configurations has been known for years (e.g., Lin et al. 2008; Vaivads et al. 2012; Zelenyi et al. 2020). This fact points to the common physical nature of their features and dynamical properties, which are still insufficiently studied.

This is the first part of the review, in which we describe the state of the art, and analyze perspectives of the 3-D approach. We discuss typical situations occurring in interplanetary space in which the structures of various scales are involved most frequently. We compare properties of 3-D current sheets, flux ropes/ blobs/plasmoids (or 2-D magnetic islands) observed in the solar wind, the magnetosphere, and laboratory plasmas. An overview of works illustrating the impact of the dynamics of non-planar magnetic objects of various scales on the solar wind properties is given, starting with current sheets associated with the HCS, ICMEs, CIRs/SIRs, and stream-stream interactions. We show how and why plasmoids (or 2D magnetic islands) are related to current sheets. Finally, the review is concluded with the discussion of the role of dynamical current sheets and plasmoids in turbulence and particle acceleration in the heliosphere. Conclusions on the applicability/non-applicability of the 2-D approach are made in each particular case.

2 Current Sheets, Flux Ropes, and Plasmoids

Current sheets, plasmoids/blobs/magnetic bubbles/flux ropes represent plasma structures often observed in conjunction with one another in space plasmas. This is determined by the development of a cascade of processes leading to the creation of morphologically-different but origin-linked objects in a finite region. Current sheets affected by various instabilities experience magnetic reconnection that in turn leads to many subsequent nonlinear effects, triggering the turbulent cascade, and the formation of plasma bubbles/plasmoids or flux ropes. The dynamics of all these structures are known to cause the acceleration of charged particles. Notably, these processes are observed from the corona to the outer heliosphere and may often be described by the same theories. We begin this section with the description of quasi-stable current sheets associated with the largest 3-D objects in the heliosphere,

followed by a discussion of views on formation and evolution of smaller-scale unstable current sheets, flux ropes and plasmoids in the heliosphere and effects associated with their dynamics.

2.1 Current Sheets in Space Plasmas

Current sheets, i.e. surfaces carrying the electric current, are ubiquitously formed at various scales in the solar corona, the solar wind and planetary magnetospheres as well as at boundaries of plasmas with dramatically different properties, discontinuities and separatrices. Thin current sheets (TCSs) with a thickness of about several proton gyroradii are often associated with turbulence or intermittency, as we show in detail in Part II of this review (see also Servidio et al. 2009, 2015; Matthaeus et al. 2015 and Sect. 2.1.4), while some TCSs are formed in quasi-laminar streams (see Sects. 2.1.1 and 2.1.2). Turbulence-borne TCSs are usually not only thin but also short and unstable (Tenerani et al. 2015). At the same time, some TCSs observed in the heliosphere are large-scale in terms of their elongation, and quasi-stable in terms of their life-time and spatial evolution. A notable example is the HCS, the best known quasi-stable current sheet (QSC) not associated with turbulence, that separates large-scale sectors of the interplanetary magnetic field (IMF) of the dominant positive/negative polarity (see Sect. 2.1.1). For a long time, the HCS has been thought to represent a unique extension of the solar magnetic equator, the only one of its sort in the heliosphere, although recent studies show that other QSCs of solar origin may appear at middle and high heliolatitudes, completing the heliospheric electric current chain. Large-scale QCSs are also formed at the borders of, and within, high-speed streams/flows in the solar wind (see Sect. 2.1.2). The other examples are the terrestrial magnetotail current sheet and the current sheet formed at the terrestrial magnetopause (see Sect. 2.1.3).

Secondary TCSs are formed in the vicinity of the HCS and similar QCSs as a result of magnetic reconnection (see Sect. 2.1.1). Despite repeating the form of the main current sheet and possessing practically the same characteristics, these meta-stable current sheets may be involved in the turbulent cascade. Therefore they play an important role in the formation of the heliospheric plasma sheet (HPS) and ensure the hierarchical transition from QCSs to unstable turbulence-borne current sheets.

There are several methods to identify current sheets in the solar wind (e.g., Ness and Burlaga 2001; Zhang et al. 2008; Li 2008; Li et al. 2011; Suess et al. 2009; Miao et al. 2011; Khabarova et al. 2015, 2016). For example, there are two modifications of the fully automated method proposed by Gang Li (Li 2008). The method is based on calculation of the angle between two magnetic field vectors measured at time 1 and time 2, which allows one to find temporal changes of the angle which correspond to spatial changes in the IMF topology. Details about steps to derive the location and width of current sheets can be found in Li (2008), Miao et al. (2011), and Li et al. (2011).

There are other automated methods identifying current sheets, which also consider either variations of the IMF vector direction and/or the IMF strength changes (Zhdankin et al. 2013; Podesta 2017; Azizabadi et al. 2020; Pecora et al. 2021). The methods are based on Taylor's hypothesis suggesting that current sheets are embedded in the solar wind flow and consist of particles moving with the structure. The approach is ideal for studies of properties of current sheets observed in the turbulent solar wind.

A simple visual inspection of current sheet crossings is often used instead of Li's or similar methods in case studies that do not require identifying a lot of current sheets for a statistical analysis (Zhang et al. 2008; Suess et al. 2009; Khabarova et al. 2015, 2016, 2017a, 2017b, 2018a, 2020; Khabarova and Zank 2017; Malova et al. 2017; Adhikari et al. 2019).

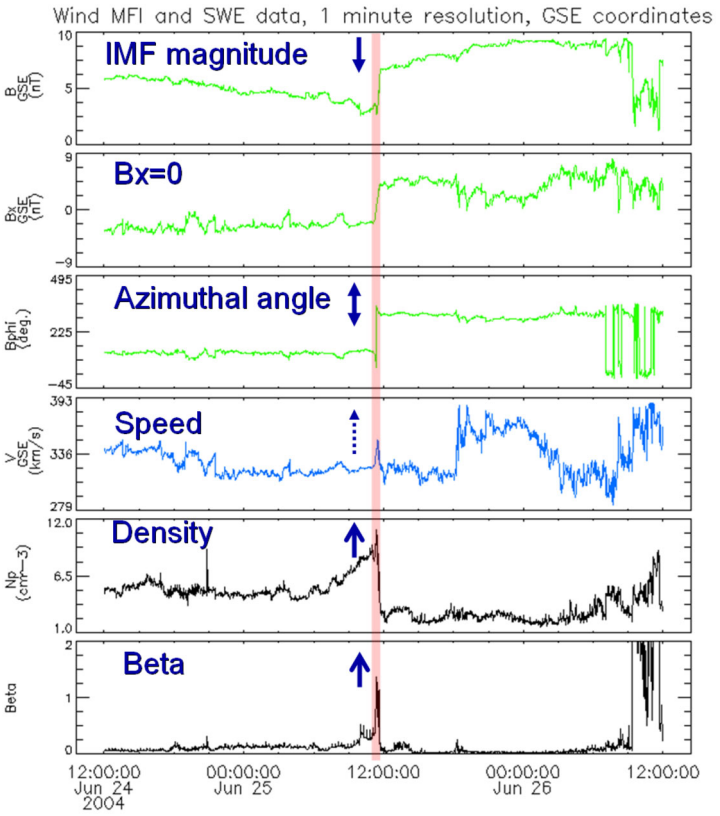

Fig. 1 Example of an uncomplicated crossing of a current sheet identified from the plasma and IMF data with a minute resolution observed by the Wind spacecraft at 1 AU on June 25, 2004. 1-minute resolution data from the WIND spacecraft are used. The HCS is shown by the pink stripe. From top to bottom: the IMF strength (B), the horizontal Earth-Sun-aligned IMF component (B_x), the azimuthal angle of the IMF (B_{phi}), the solar wind speed (V), the solar wind density (Np), and the plasma beta (the ratio of the plasma pressure to the magnetic field pressure). A classic HCS crossing is identified with the depression in the total B since at least one IMF component becomes zero at the neutral line (in the particular case it is B_x), the increase in Np, and the increase in the plasma beta are observed at the HCS position. Arrows show dynamics of the corresponding parameters at the current sheet. Typical signatures are as follows: the IMF strength drops, at least one of IMF components crosses zero value, the azimuthal IMF angle and/or clock angle change sharply, the solar wind density and the plasma beta increase sharply, while the solar wind speed may not change. The event is discussed in Zharkova and Khabarova (2012)

For example, current sheets observed by near-Earth spacecraft with a resolution better than one minute can be identified through finding the following features (see Fig. 1): (i) a dip in the IMF strength (since at least one of the IMF components is zero), (ii) a sharp change in the IMF azimuthal angle, which is often accompanied by similar changes in the clock IMF angle if a current sheet front is far from lying in the ecliptic plane, and (iii) a sharp density increase, which, in combination with the total magnetic field decrease, leads to an abrupt plasma beta (the ratio of the plasma pressure to the magnetic pressure) increase.

The solar wind speed is rather indifferent to the current sheet crossing, unless there is a Petschek-type reconnection occurring nearby. Then the speed shows a weak increase together with the temperature. At the same time, a significant drop in the Alfven speed to the solar wind speed ratio is often observed at current sheets.

The features listed above are used to build an automated current sheet indentifying method that considers both IMF and plasma variations to find current sheet positions with a one-second cadence (Khabarova et al. 2021). The corresponding multiyear database of current sheets identified at 1 AU can be found at https://csdb.izmiran.ru/index.html.

Meanwhile, the properties of current sheets listed above are insufficient if one wants to distinguish, for example, between a QCS and a secondary TCS. An investigation of this kind is often required for the analysis of crossings of the HPS, taking into account that the wide HPS surrounds the HCS and is filled with numerous secondary TCSs with properties similar to those of the HCS (e.g., Winterhalter et al. 1994; Crooker et al. 2004; Adhikari et al. 2019). Therefore, simple methods should sometimes be enhanced with an analysis of streams and structures in which current sheets are located. The position of current sheets should be compared with the location of coherent structures of all types, intermittency events and discontinuities (e.g., Bruno et al. 2001; Greco et al. 2009; Lion et al. 2016). The latter can be identified via the method called "Partial Variance of Increments" (PVI), detecting sharp changes in the IMF strength (see Greco et al. 2009, 2018; Tessein et al. 2013, 2015). An analysis of pitch-angle distribution (PAD) spectrograms characterizing spatial characteristics of suprathermal electrons near the object of interest is often employed as well (see Sect. 2.1.1). Overall, if a visual inspection is supposed, a combination of several methods gives the best results in terms of current sheet identification (e.g., Malandraki et al. 2019).

It is very important to note that since current sheets in the solar wind are subject to magnetic reconnection, each current sheet tends to be multi-layered, creating its own intermittent vicinity analogous to the HPS formed at both sides of the HCS (see Malova et al. 2017 and references therein). Interestingly, this feature appears down to the smallest scales, according to observations and their comparison with theoretical predictions (see also Lazarian et al. 2012, 2020; Kowal et al. 2012; Greco et al. 2016; Lion et al. 2016; and Part II of this review). An analysis of the fine structure of current sheets of different origins in the solar wind at 1 AU reveals their striking similarity in terms of forming a central thin current sheet along which the largest current flows. The central current sheet is found to be embedded into a much wider current layer with randomly distributed weaker currents. In Fig. 2, the normal direction to each current sheet is identified with help of the minimum variance analysis (Hu and Sonnerup 2003; Malova et al. 2017). The upper panels characterize current sheet crossings seen via profiles of their normalized magnetic field components in the maximum variance direction, and the lower panels show variations of the normalized current density through the current sheets.

All current sheets are grouped with regard to their origin indicated on the left of the panels. Panels a) stand for the HCS crossings, b) characterize strong current sheets (SCSs) observed within the HPS, and c) shows SCSs at the leading edge of a CIR (see details in Malova et al. 2017).

The main thin current density peak seen in each bottom panel occurs at the crossing of the central narrow current sheet. The irregular spikes correspond to currents flowing in the wider current sheets into which the thinner are embedded. Malova et al. (2017) concluded that the narrow current sheet is formed owing to the quasi-adiabatic motion of demagnetized protons, and a wider analog of the plasma sheet is supported by a thermal isotropic population of particles.

Therefore, current sheets of various origins observed in the solar wind possess practically the same fine-scale properties, having a width up to 10^5 km with a thinner central current sheet of 10^3–10^4 km (see Fig. 2). This means that the known difference in their dynamics and stability can be understood only under a larger-scale approach which considers the origin and properties of a particular current sheet. Considering such an approach, we first discuss the formation of QSCs within the largest-scale objects in the heliosphere.

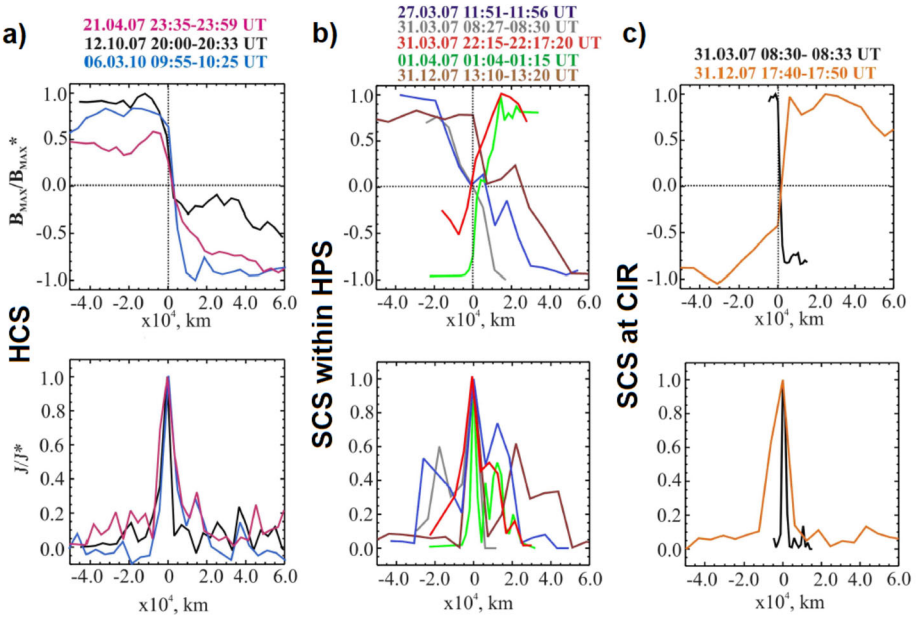

Fig. 2 Results of the minimum variance analysis for current sheets of different origins. **a**) Heliospheric current sheet; **b**) randomly picked current sheets observed in the HPS; **c**) current sheets at the leading edge of a CIR. Upper panels: the normalized magnetic field strength in the maximum variance direction; zero corresponds to the neutral plane along the normal direction to the current sheet front. Bottom panels: normalized current density. Adapted from Malova et al. (2017)

In Sect. 2.1.1, we attract the reader's attention to the most important observational facts about dynamical processes occurring at the HCS and in its vicinity, the HPS. A comparison of prior and recent interpretations of observations is given, and aspects of further development of the study of non-stationary processes associated with the HCS/HPS and similar strong current sheets in the heliosphere are discussed.

Section 2.1.2 focuses on QSCs associated with ICMEs, coronal holes (CHs) (both polar and cross-equatorial), CIRs and less stable SIRs, and their relation to flux ropes/plasmoids.

Section 2.1.3 is aimed at discussing studies of QSCs formed within planetary magnetospheres and their magnetotails, comets, and at interplanetary shocks. The discussion of properties of current sheets in the heliosphere is closed by Sect. 2.1.4, which is about unstable TCSs associated with intermittency and turbulence. We also provide an overview of recent advances in studies of the role of 3-D magnetic reconnection as a process linking current sheets and plasmoids/flux ropes/magnetic islands.

2.1.1 The Heliospheric Current Sheet (HCS), the Heliospheric Plasma Sheet (HPS) and Similarly Strong Current Sheets of the Solar Origin

This section discusses key observational aspects of the HCS dynamics and effects associated with crossings of the HCS embedded in the one-order wider HPS. The evolution of views on the HCS nature and associated effects will also be shown. For a long time, the HCS has been considered as a "ballerina-skirt"-like structure twisted along the Parker spiral direction, separating differently-directed interplanetary magnetic field (IMF) lines, slowly waving and

passively interacting with solar wind fast streams or flows (Khabarova et al. 2020 and references therein). It has been supposed that a spacecraft crosses it as a planar discontinuity. However, there are many facts that cannot be easily explained within this approach. These are as follows: (i) the occurrence of numerous current sheets and coherent structures around the HCS, (ii) the unusual behavior of suprathermal electrons characterized by dropouts or double-directed streaming in pitch-angle distributions (PADs), (iii) observations of energetic particles near the HCS, or (iv) mismatches between the HCS identification through the IMF/plasma parameters and PADs.

The discovery of the HPS surrounding the HCS became the first step to a better understanding of the HCS dynamics. The next step was HCS modeling that revealed bending and kink waves as well as small-scale ripples on the HCS surface. The waving and rippled HCS/HPS system confines current sheets and small-scale magnetic islands (SMIs), which dramatically increases the effectiveness of stochastic magnetic reconnection and allows the acceleration of trapped energetic particles up to MeV energies. We will show below that it is possible to solve the problem of mismatches in the HCS identification, taking into account non-planarity of the HCS and the presence of smaller-scale locally-born structures produced by dynamical processes.

Formation and self-organization of current sheets is a natural consequence of the tendency of unidirectional currents to attract each other and merge in a form of a stable sheet (e.g., Zelenyi et al. 2008a, 2008b, 2011, 2020; Vaivads et al. 2012). TCSs occur in different plasmas, from the laboratory to interplanetary space. As noted above, they may be formed at small-scale discontinuities and appear as a result of turbulence and non-stationary processes (see Furno et al. 2005; Servidio et al. 2009, 2015; Valentini et al. 2016; Pezzi et al. 2017, 2018, 2019; Sorriso-Valvo et al. 2018; Gekelman et al. 2012, 2016, 2018 and Part II of this review). On the other hand, there is a distinct type of current sheets in the heliosphere: large-scale (elongated) TCSs. Some of them are of the solar origin (Kislov et al. 2019), and some of them are associated with high-speed plasma streams/flows (see Sect. 2.1.2). Among other current sheets of the solar origin, the HCS is known as the most stable, unique while yet poorly-investigated object playing a major role in the global system of currents flowing in the heliosphere.

We will begin with a discussion of points of views on the HCS as a large-scale structure. So far, it is known that the HCS is a rather thin layer, which carries the total azimuthal electric current of ~ 1 GA with a current density of $\sim 10^{-10}$ A/m^2 and has a typical size of several gyroradii, according to in situ observations (see Malova et al. 2017 and references therein) and theoretical estimations (Alfvén 1977; Kislov et al. 2015). Since the HCS can roughly be considered as an extension of the solar magnetic equator (Davis 1965; Wilcox and Ness 1965; Wilcox 1968; Svalgaard and Wilcox 1975; Bruno et al. 1982), it is not surprising to find that the HCS is embedded into at least one order wider heliospheric plasma sheet (HPS) (Winterhalter et al. 1994; Simunac et al. 2012) filled with remnants of coronal streamers surrounding the originating neutral line at the Sun. The other structures filling the HPS far from the Sun are products of local dynamical processes occurring at the HCS directly in the solar wind. The latter include various coherent structures, waves, secondary thinner current sheets, and plasmoids/magnetic islands (see Khabarova et al. 2015, 2016, 2017b, 2018a; Adhikari et al. 2019). The edges of the HPS also represent strong current sheets. Estimates show that the entire HCS-HPS conglomerate carries a much larger total azimuthal current (~ 25 GA) than the HCS alone (Kislov et al. 2015). The radial electric current is approximately two times smaller than the azimuthal current.

Historically, the existence of a line separating the IMF of different polarities was obvious from a purely theoretical point of view, since the dipole solar magnetic field should

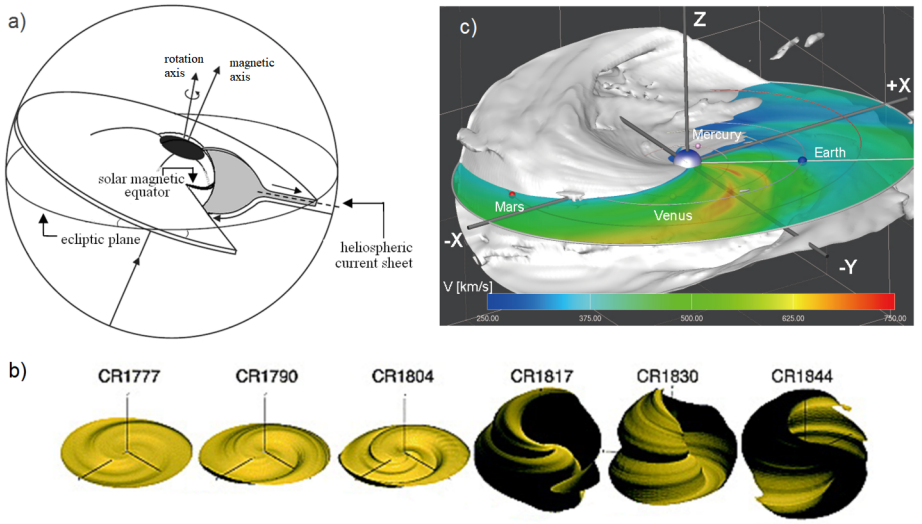

Fig. 3 Illustration of the evolution of views on the HCS form. **a**) Formation of the plain HCS as an extension of the solar magnetic equator with simultaneous impact of higher-latitude magnetic field lines – a sketch, modified from Hundhausen (1972); **b**) MHD simulation of the HCS shape out to 5 AU from solar minimum (1986) to solar maximum (1991), from left to right, respectively (adapted from Riley et al. 2002); **c**) Near real-time three-dimensional MHD modeling of the HCS shape (grey) and the solar wind speed (color) in the ecliptic plane on 26 October 2008, according to Shiota et al. (2014)

have a separator analogous to that in the terrestrial magnetotail (Davis 1965; Wilcox and Ness 1965; Wilcox 1968; Schatten 1971; Svalgaard and Wilcox 1975; Bruno et al. 1982). Therefore, the views and ideas about the HCS structure first naturally came from theoretical studies, and then the HCS was discovered from in situ observations. The first step was to understand the sector structure of the heliosphere in general, and the fine structure of the HCS and surrounding areas was a secondary question. Consequently, the approach to the HCS-associated effects was simplified, and the HCS was idealized. The first works considered the HCS as a very thin planar structure (see Fig. 3a).

It was a very important step forward to realize that IMF sectors are observed not only because the ecliptic plane is inclined to the solar magnetic equator plane but also because the HCS possesses a wavy form, which was called “a ballerina skirt” (Wilcox et al. 1980). At the next stage, a magnetohydrodynamic (MHD) modeling that considered real solar observations as boundary conditions was employed to study the HCS spatial properties and gave important information about the evolution of its wavy form with solar cycle (see an example in Fig. 3b).

According to simulations, the tilt of the HCS is smallest in solar minimum, and consequently, the amplitude of the waves is minimal during that phase, but the HCS is strongly inclined to the ecliptic plane during solar maximum, which makes the HCS “skirt” bouffant (see Riley et al. 2002 and references therein). Consequently, for a long time, the HCS has been considered either as plain or as slowly waving, depending on the specificity of the particular study (see, for example, Pizzo 1994; Riley et al. 2002; Veselovsky et al. 2002 and references therein).

Modern MHD simulations represent modifications of potential field source surface (PFSS) models and are based on solar observational data obtained in near real-time, which involves the processing of daily synoptic maps and gathering information about solar flares,

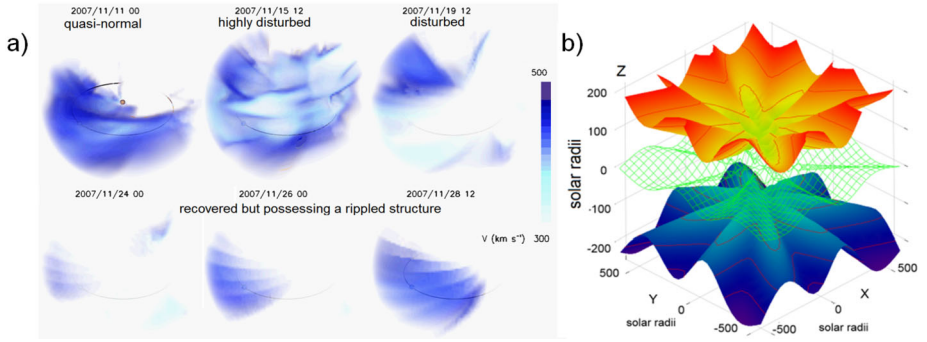

Fig. 4 Variable shape of the dynamical HCS. **a**) Several-day variations of the HCS shape reconstructed from observations of interplanetary scintillations (adapted from Khabarova et al. 2016). **b**) Three HCS-type current sheets in the heliosphere in the case of non-dipole solar magnetic field far from the solar minimum (adapted from Kislov et al. 2019)

coronal mass ejections (CMEs) and CHs (see, for example, Shiota et al. 2014 and references therein). The resulting pictures of the HCS in the inner heliosphere reveal numerous details and show the evolution of small-scale structures at the HCS, including the propagation of waves and formation of ripples at the HCS (see an example in Fig. 3c).

Observations of interplanetary scintillations allow for a better understanding of possible HCS shapes through reconstructions of the velocity profiles from the Sun up to 1.5 AU (Bisi et al. 2008, 2010; Jackson et al. 2009). Figure 4a shows the 3D tomographic plots of the solar wind velocity reconstructed by the Solar Terrestrial Environment Laboratory (STEL or STELab) from ground-based interplanetary scintillation observations (http://smei.ucsd.edu/new_smei/dataandimages/dataandimages.html). There is a well-known strong correspondence between solar wind velocity spatial profiles and the IMF profiles (Tokumaru 2013; Shiota et al. 2014; Tokumaru et al. 2017), therefore the restored velocity profiles are often used to estimate the HCS dynamics (at least approximately) for certain periods of observations. The HCS profiles in Fig. 4a vary from the smooth shape with large-scale waves corresponding to theoretical predictions of the ballerina-skirt HCS to the highly-disturbed multi-layer shape (the stratified HCS resembling rose leaves), and even to the plisse-skirt (the rippled HCS).

The multi-current sheet case may take place both after the passage of ICMEs, like it happened during the event shown in Fig. 4a (see Khabarova et al. 2016), and also if the solar magnetic field possesses strong non-dipole harmonics as shown in some MHD models (Kislov et al. 2019; Maiewski et al. 2020).

Figure 4b illustrates the possibility of the co-existence of the three large-scale HCS-type current sheets in the heliosphere (Kislov et al. 2019). The latter opens an opportunity for explanations of puzzling out-of-ecliptic observations, but this aspect will not be discussed here since features of crossings of all current sheets, including high-latitude ones, are identical.

Under hourly or daily averaging, the HCS-HPS system can be simply treated as the HCS or the sector boundary (SB), which means that it separates sectors of the IMF of the positive and negative polarities. The sectors represent large-scale regions with magnetic field lines directed either toward the Sun or away from it. In simple cases of SB crossings, the IMF direction is characterized by the azimuthal IMF angle (usually called B_{phi} or φ), which abruptly changes at sector boundary crossings (SBCs). A relatively stable IMF direction within a sector is typically observed at the Earth's position for days during solar minimum, but the IMF

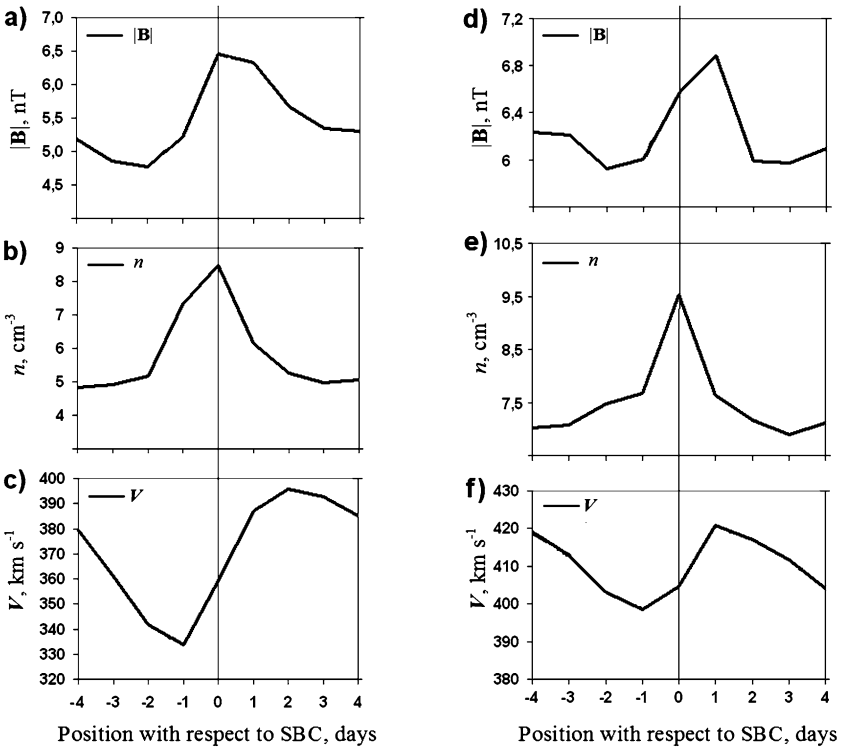

Fig. 5 Behavior of the key solar wind plasma and IMF parameters across the HCS (a unified SBC) at 1 AU as seen at large scales. Data resolution is one day. From top to bottom: modulus of the IMF strength $|B|$, the solar wind density n, and the speed V. Left panel shows results of the superposed epoch analysis of 1300 events from the Leif Svalgaard's SBC list, and the right panel shows the same for 149 events from the ISTP Solar Wind Catalogue. Adapted from Khabarova and Zastenker (2011)

polarity can be very unstable during the other phases of the solar cycle. Sometimes, a SBC lasts for several days while the IMF direction sharply varies from + (outward) to − (inward) and back (see Fig. 7 from Khabarova and Zastenker 2011 and an example of such a crossing to be seen in Fig. 1 from Malova et al. 2017). A picture of the IMF polarity changes shown in a color map form for the period from 1965 to the present with a daily resolution can be found at the OMNI website: https://omniweb.gsfc.nasa.gov/html/polarity/polarity.html. It can be used for an approximate estimation of the length of magnetic sectors.

Like all solar wind structures, the HCS properties are very different at different scales. The behavior of the key plasma and IMF parameters near SBCs at large scales is illustrated in Fig. 5, adopted from Khabarova and Zastenker (2011). A superposed epoch method is employed to show variations of the modulus of the IMF strength, the solar wind density and the solar wind speed across a unified SBC. All SBC days are treated as a zero day, and the corresponding averaged curves are shown with respect to zero day with a step of +/− one day. Daily averaged data are used here for the analysis of 1300 events from the SBC list compiled by Leif Svalgaard for 1964–2010 (the current list is available at https://www.leif.org/research/sblist.txt), as shown in Fig. 5a, b, c (the left panel). The same is obtained for a shorter (1994–2000) alternative list consisting of 149 events from the ISTP Solar Wind Catalogue of Candidate Events (https://

www-spof.gsfc.nasa.gov/scripts/sw-cat/grep-ls/SBC.html) and shown in Fig. 5 d, e, f (the right panel). Similar results were also obtained using a far smaller statistical database (Borrini et al. 1981).

One can find that both the IMF strength and the solar wind density increase on the days of SBCs, but that $|B|$ has a wider maximum, lasting for two days, and n peaks exactly on the day of the SBC. The strange behavior of the solar wind speed is still not satisfactorily explained. In particular, it was discussed by Zharkova and Khabarova (2012), who suggested that the asymmetric profile of the speed at least partially may be explained by the separation of charged particles to different sides of a strong reconnecting current sheet. The effect is predicted to be seen up to tens of gyroradii around the current sheet. If the cumulative impact of many current sheets is taken into account, the HCS/HPS system may potentially generate this effect throughout a rather wide area around the SBC.

This may be at least one of reasons, and the second reason is a purely statistical effect of the detecting of SBCs one day after the passage of trailing edges of ICMEs with the depressed speed and one day before the arrival of leading fast edges of CIRs or ICMEs (see Adhikari et al. 2019). Since the latter has not yet been properly checked, the effect may be considered as still not totally explained.

Notably, the Kp index of geomagnetic activity (see https://www.swpc.noaa.gov/products/planetary-k-index) possesses the same profile as the speed (see Khabarova and Zastenker 2011). The effect in Kp has been obvious from the beginning of the space era and was noted for the first time by Svalgaard and Wilcox (1975), who explained it by the variable geoeffectiveness of corresponding variations in the solar wind dynamical pressure, but the solar wind source of the feature remained unclear. According to Fig. 5, there is an impact of the HCS-HPS system on the surrounding plasma. Therefore, a study of the HCS properties and dynamics is very important for better understanding the solar-terrestrial couplings.

If one analyzes higher-resolution (at least one-minute) observations, it is easy to find that the typical features of SBCs are quite different from those shown in Fig. 5. If there are no multi-spacecraft observations that enable the calculation of the electric current to identify the HCS directly, the classic uncomplicated HCS crossing by a single spacecraft is associated with the behavior of the plasma and IMF parameters analogous to those seen in Fig. 1:

- the total IMF significantly drops for several minutes, sometimes to very low values, owing to the crossing of a zero line in at least one of the IMF components; the corresponding depression in the IMF strength is about 2 nT or larger;
- the solar wind density notably increases both in the nearest vicinity of the HCS and several hours around, having a peak at the HCS;
- the plasma beta parameter increases sharply above 1 exactly at the HCS and also jumps at all strong current sheets surrounding the HCS, therefore the HPS area is characterized by series of plasma beta peaks sometimes reaching 100 and above;
- If the solar wind speed and the temperature both increase, this may indicate the crossing of a site of the HPS actively reconnecting in a Petschek manner. Meanwhile, the solar wind speed may not change at the HCS at all or even slightly decrease; therefore the solar wind speed cannot be considered as a good indicator of SBCs.
- the IMF azimuthal (or clock) angle B_{phi} or φ, i.e. the angle which characterizes variations of the IMF sunward/anti-sunward direction along the ecliptic plane, changes between the 90–180 degrees (typical for the anti-sunward or positive polarity) and 270–360° (typical for the sunward or negative polarity). Variations in the IMF azimuthal angle are usually considered to be the simplest way to identify an HCS crossing from the IMF data, but sometimes a comprehensive analysis, taking into account all features listed above, is required.

– The IMF elevation (or cone) angle identifying the IMF vector variations in the plane perpendicular to the ecliptic usually changes simultaneously or even before the IMF, showing how the HCS plane is declined to the ecliptic plane. It is usually called B_{theta} or θ. It is important to analyze the behavior of this angle additionally to B_{phi} in unclear cases or complex SBCs.

The event shown in Fig. 1 above was analyzed by Zharkova and Khabarova (2012) in order to compare observations and particle-in-cell (PIC) simulations of the behavior of charged particles in the conditions typical for the reconnecting HCS and similar current sheets. The clear change in the azimuthal angle from the positive to negative IMF polarity in combination with other signatures suggest the presence of a SBC, i.e. the HCS surrounded by a very thin HPS crossed for a short period.

Note that the IMF strength sharply decreases at the HCS position, but roughly averaged data may not show this, and the one-day picture is always characterized by the increase in both the IMF strength and the density, which is a natural feature of the plasma/magnetic field behavior near strong currents, as shown in Fig. 5. Therefore, these characteristics of B near the HCS should not be considered as a contradiction.

It also should be noted that a crossing of any current sheet as strong as the HCS is characterized by the same changes in the key plasma and IMF parameters (Malova et al. 2017; Adhikari et al. 2019). A paradox is that knowing typical features of current sheet crossings suggests the possibility of an automatic identification of strong current sheets of any type (see, for example, Li 2008) but does not enable the creation of an automatic method to identify the HCS with a high resolution, since the HCS is often surrounded by many other similar structures within the HPS, and a visual inspection is always required, as noted above. The HCS can visually be distinguished from other current sheets within the HPS by finding the maximum of the solar wind density and the strongest current flow within the HPS region typically crossed for an hour or two (Khabarova and Zastenker 2011; Malova et al. 2018). The HCS is usually associated with the most prominent changes in the IMF angles.

In clear cases of SBCs, a passage through the HPS-HCS system takes minutes, but in some events it may take days (Crooker et al. 2004; Khabarova and Zastenker 2011), which contradicts the simplified description of the HCS as a plain or large-scale-waved structure.

One may suggest to explain unusually prolonged crossings of the HCS by its up/down flapping a whole. In magnetospheric physics, such flapping is often employed to explain multiple crossings of the terrestrial magnetotail (Rong et al. 2015), but the idea does not work well in the heliosphere since (i) the HCS is too large for the fast up/down motion that could explain observed minute-range sharp variations in the IMF direction sometimes lasting for hours or days, and (ii) flapping always suggests the detection of the same IMF/plasma peculiarities twice but in the reversed order: one time when a spacecraft crosses a current sheet on its way to the turning point, and the second time – on its way back.

This puzzle can be solved if one takes into account the existence of the wide HPS that the HCS is embedded in. This may satisfactorily explain many events, but sometimes such an interpretation is impossible since some HCS crossings are associated with variations of the azimuthal IMF angle having all the signatures of an upcoming SBC, but finally B_{phi} indicates a sector with the same polarity as in the beginning of the event. Such events cannot be explained easily; therefore the following question about the structure of the HCS as observed in the IMF features discussed above arises:

Q1: *Why are unusually prolonged crossings and, especially, incomplete crossings of the HCS observed?*

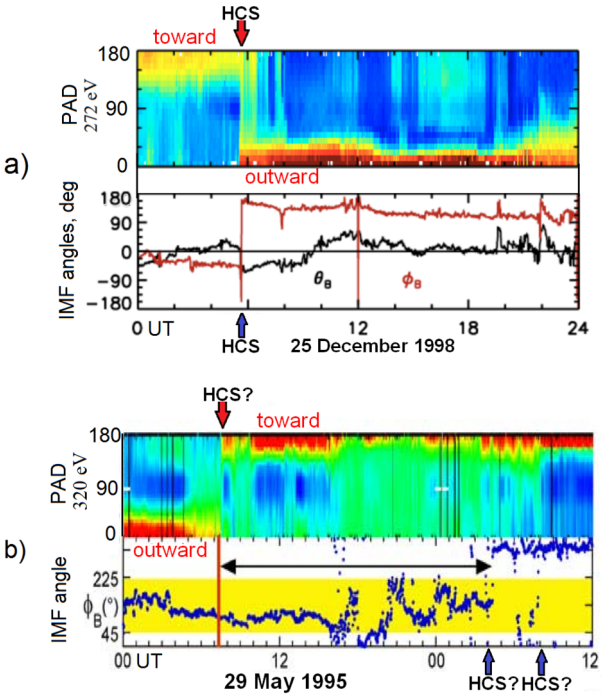

Fig. 6 Examples of easy and problematic identifications of the HCS in terms of coinciding/ not coinciding features in PADs and the IMF. **a**) Classic crossing. Upper panel: PAD of 272 eV suprathermal electrons. Lower panel: Azimuthal (red) and elevation (black) angles of the IMF. ACE data. Modified from Gosling et al. (2006). **b**) Crossing problematic for interpretation within a classic view on the HCS. Upper panel: PAD of 320 eV suprathermal electrons. Lower panel: azimuthal angle of the IMF. WIND data. Modified from Crooker et al. (2004). Red stripes in the PADs indicate the intense flow of strahl electrons in the dominant IMF direction. In **a**), the strahl flow direction change is fast and rather regular, and the azimuthal IMF angle sharp change coincides with the supposed position of the HCS identified from the PAD changes. Note that counterstreaming strahls (color stripes in the PAD both near 0° and 180°) are observed in the vicinity of the HCS. In **b**), changes in the PAD and the azimuthal angle are poorly correlated, the HCS identification is difficult, and counterstreaming strahls and omni-directional electrons are observed in a wide area around supposed HCS crossings

A second question related to Q1 has presented a major puzzle for the community for years. There is an alternative way to identify the HCS crossing at 1 AU, employing not the IMF parameters listed above but pitch-angle distributions (PADs) of suprathermal electrons with energies of ~ 70 eV and above (see Crooker et al. 2004 and references therein). The logic is as follows: the dominant paradigm says that suprathermal electrons are accelerated only in the solar corona and propagate along the main IMF direction either toward or away from the Sun, being too energetic and fast to "notice" local perturbations. Therefore, within the "planar and thin HCS directed along the Parker spiral" views, it is expected to find sharp changes in the IMF direction at the HCS reflected in suprathermal-electron-PAD spectrograms. Indeed, this is true in some events, but mismatches of an unclear nature between the HCS position identified from PAD changes and from B_{phi} variations are often seen in observations from all spacecraft that have ever crossed the HCS.

Two examples of PADs associated with the HCS crossing are given in Fig. 6. The changes in the suprathermal electron flow direction typical for HCS crossings seen are indicated by

the red arrow in the upper panel of Fig. 6a. In this particular case, PAD-specific signatures of the HCS crossing coincide with changes in the IMF azimuthal angle that usually characterise SBCs (shown by the dark blue arrow in the lower panel). In this sense, this particular HCS crossing is classic and undoubtful. This crossing was also chosen by Gosling et al. (2006) to demonstrate the presence of counterstreaming or bi-directional strahls (i.e., electron beams, streaming simultaneously both in the nearly 0° and 180° directions) often observed near the HCS in regions with signatures of rotating magnetic field vector. The latter was mentioned by Gosling et al. (2006) as an intriguing point that required an additional study.

The 320 eV suprathermal electron PAD in the upper panel of Fig. 6b shows the change in the strahl beam propagation direction from away to toward the Sun several hours before the azimuthal angle finally indicating that the WIND spacecraft is in the sector with a stable IMF polarity (see the horizontal arrow showing how prolonged the mismatch is). At this step, one can additionally notice that (i) the period of an uncertain direction of suprathermal electron motion actually lasts from the end of the red strahl "outward" stripe in the PAD to the last sharp change in the azimuthal IMF angle shown in Fig. 6b by the dark-blue vertical arrow below the bottom panel (see a several-hour-length green region) (ii) the outward/inward strahl beams (red stripes) coexist with bi-directional strahls and multi-directed electrons in wide areas, and (iii) there is a gap between the edges of the 0°/180° red PAD stripes showing the change of the strahl movement direction and the red arrow indicating one of the assumed positions of the HCS.

A classic crossing of the planar HCS suggests the detection of simultaneous changes in the inward-outward-direction of strahl motion and changes in the IMF direction, but Fig. 6b represents a complicated case which may be interpreted differently. There have been attempts to explain features shown in Fig. 6b by field-line footpoint motions in the solar atmosphere and/or bending of the IMF field lines back to the Sun, since the dominant paradigm formulated before 2010th was that strahls should ultimately be of solar origin and energetic suprathermal electrons are indifferent to local plasma/IMF structures (Crooker et al. 2003; Gosling et al. 2004; Baker et al. 2009 and references therein). The particular event was interpreted by Crooker et al. (2004) within the 2-D views on the HCS as a structure generally planar everywhere, except for rare points of bending. Crooker et al. (2004) assumed that the HCS could bend itself far back to the Sun (see the description of Fig. 9 below). Crooker et al. (2004) claimed that the method using the suprathermal electron PADs is a true identification of crossings of the HCS, while the classic method based on the analysis of the magnetic field vector changes is often incorrect.

However, this may also indicate far more complex dynamical processes occurring in the nearest vicinity of the HCS if one takes into account the existence of the HPS and 3-D topological features related to the distortion of the HCS. The event shown in Fig. 6b is exactly the case when a comprehensive analysis of the behavior of the key IMF and plasma parameters is required. First of all, one can find that there is a crossing of a strong current sheet occurring exactly at the assumed HCS position indicated in Fig. 6b by the red arrow, since the elevation angle B_{theta} sharply changes here simultaneously with the HCS-characteristic change in the PAD. The mismatch between the magnetic field behavior and PAD patterns noticed by Crooker et al. (2004) can be explained if one imagines the HCS 3-D front placed practically perpendicular to the ecliptic plane. In this case, the azimuthal angle B_{phi} analyzed by Crooker et al. (2004) shows no changes but, instead, the elevation angle B_{theta} changes indicate the HCS crossing. This means that mismatches between the HCS identification via suprathermal electron PADs and via the IMF properties can be solved under a 3-D approach if one suggests a complex behavior of the HCS and considers signatures of the sector boundary crossing altogether.

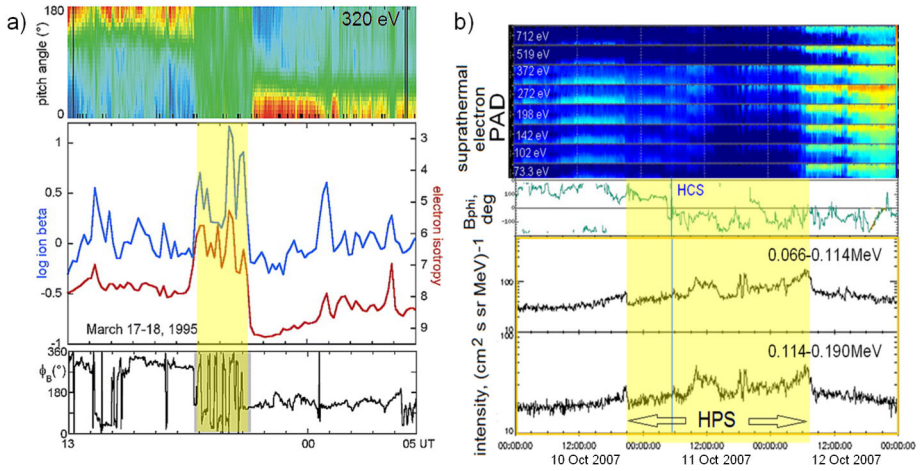

Fig. 7 Examples of scattering of suprathermal electrons within the HPS. **a**) Several-hour crossing of the HPS filled with numerous coherent structures. From top to bottom: PAD of 320 eV suprathermal electrons, the plasma beta and the electron isotropy index, and the azimuthal IMF angle. The angles of the electron flows are uncertain, the plasma beta is high, and the azimuthal angle varies quickly in the HPS area (marked by yellow stripe). WIND data. Modified from Crooker et al. (2003). **b**) ∼ 1.5 days of crossing of the HPS (yellow stripe) with the corresponding dropouts in PADs. From top to bottom: PADs in several energy channels indicated in the figure, the azimuthal angle, and two panels showing an elevated level of the energetic ion flux associated with the HPS crossing. ACE data. Adapted from Khabarova et al. (2018a)

Recent studies show that the PAD/IMF peculiarities discussed above are often observed when the HCS becomes displaced away of the ecliptic plane, standing almost perpendicular to it, when it is pushed and bent by an approaching high-speed stream. The corresponding illustrations of the process can be found in Adhikari et al. (2019), Figs. 22 and 31 below. It is easy to find from the list of CIRs and transient SIRs compiled by Lan Jian (Jian et al. 2006) that the HCS interacted with a SIR in the particular case discussed by Crooker et al. (2004), which caused the observed distortion of the HCS. We will discuss examples of such events in Sects. 2.1.4 and 3.1 below, considering the HCS as a 3-D object at all scales and suggesting the interpretation given above that does not require an unnatural bending of the HCS back to the Sun.

Two examples of even more complex behavior of suprathermal electrons at the HCS crossings are given in Fig. 7. Figure 7a is adapted from Crooker et al. (2003) and Fig. 7b is a modified version of Fig. 3 of Khabarova et al. (2018a). These are cases of defocused beams called heat flux dropouts (HFDs) or simply dropouts in PADs, when electrons experience scattering at some plasma structures.

In Fig. 7a, the width of the yellow stripe indicating the HPS with the typical sharp variations in the azimuthal angle (shown in the lower panel) is just several hours, and Fig. 7b shows the case of ∼ 1.5 day dropouts associated with the prolonged HPS crossing. Both heat flux dropouts and the dispersionless behavior of suprathermal electrons are observed near all strong current sheets (see the vertical lines in PADs in Fig. 7b). These are characterized by changes in the PAD intensities occurring simultaneously at all energies. The same features are also seen in ICMEs or CIRs, as noted in Gosling et al. (2004).

Therefore, the discussed PAD features may be considered as probable evidence for local dynamical processes occurring at small-scale plasma structures and impacting electron

PADs (Khabarova et al. 2020). We discuss the development of views on acceleration of electrons observed in the solar wind and their PAD features in Sect. 3.3.

Figure 7b also illustrates ion acceleration associated with the HCS/HPS crossing. The two bottom panels in Fig. 7b show an increase in the energetic ion flux for ions with energies from tens to hundreds of keV/nuc as observed by ACE. Pronounced energetic ion flux enhancements are also detected by STEREO A and STEREO B for the same HCS/HPS crossing (see Zharkova and Khabarova 2015 and Khabarova et al. 2018a). The event has been interpreted in the way that observations show local particle acceleration at the reconnecting HCS embedded in the HCS.

However, there is another point of view on such events. Following Gosling et al. (2005a) who claimed the absence of particle acceleration associated with reconnecting current sheets in the solar wind within the frame of the "plain, quiet, thin and passive HCS" paradigm, one may suggest the energetic particle enhancements are determined by solar sources. We discuss this aspect in Sects. 3.1 and 3.2.

Therefore, two more key questions arise:

Q2: *Why do observations often show increases in the energetic ion flux up to MeV/nuc near the HCS?*

Q3: *Suprathermal electrons with energies above 70 eV at 1 AU are assumed to originate from the Sun only and should quickly change the direction of their motion at the HCS. Why is the behavior of suprathermal electrons in the vicinity of the HCS so complex and different from what is predicted?*

According to the results discussed above, the full picture of processes occurring at the HCS and similar large-scale current sheets in the heliosphere can be enhanced by the study of associated plasma structures observed at both kinetic and MHD scales. First of all, those are waves. Ideas about the existence of MHD waves which may occur at the HCS owing to various instabilities have been developed in theoretical works in parallel with large-scale modeling of the HCS shape. It was known from theoretical studies that the occurrence of non-flapping waves generated by instabilities explains observations of the terrestrial magnetotail dynamics well (see Furth et al. 1963; Lui et al. 1978; Galeev et al. 1986; Zelenyi et al. 2011; Zelenyi and Artemyev 2013 and references therein), which stimulated researchers to investigate the impact of the same processes on the form and properties of the HCS in the solar wind.

The results of the first comprehensive study of the development of sausage, kink, and tearing instabilities in the HCS (Wang et al. 1988) showed the probability of the development of kink waves as well as of the formation of flux ropes (also called blobs, plasmoids or magnetic islands) at heliocentric distances from 0.5 AU to at least 1.5 AU. An analogy with the formation of flux ropes in the solar corona was noted. Typical sizes of the HCS-born plasmoids were found by Wang et al. (1988) to be $\sim 10^7$–10^8 km. Wang et al. (1988) first noted that plasmoids formed in the HCS should be ejected from the HCS and advected by the surrounding solar wind away from the originating current sheet. Taking into account real plasma beta values and magnetic configurations observed in the HPS, those might be $\sim 10^5$–10^6 km as well. The latter perfectly corresponds to modern observations of HCS/HPS-associated plasma/IMF variations and plasmoids possessing periods/sizes of a wide range, typically $\sim 10^5$–10^7 km (Cartwright and Moldwin 2010; Dai et al. 2014; Khabarova et al. 2015, 2016).

The properties of non-linear waves on the HCS, the associated development of instabilities, irregular (or stochastic) magnetic reconnection as well as the formation of magnetic islands in the HCS were studied later in several independent theoretical works, the most important of which were Musielak and Suess (1988), Ruderman (1990, 1998), and Yamauchi

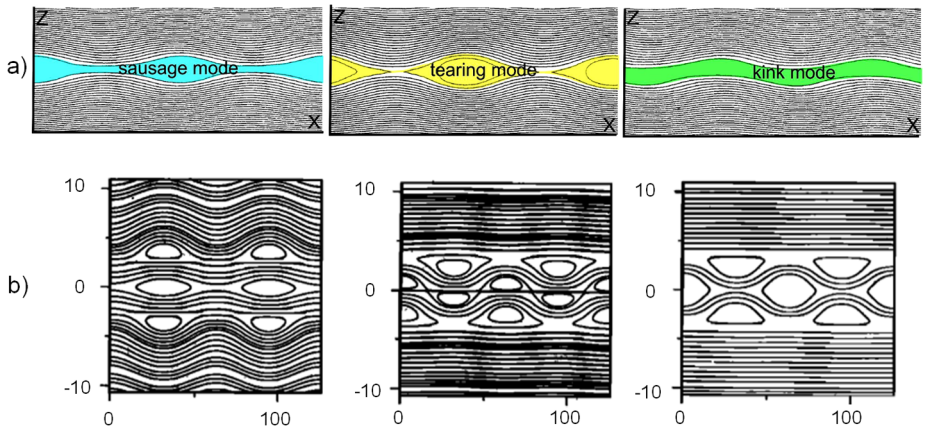

Fig. 8 Waves and plasmoids in the dynamical HCS. **a**) MHD modeling of the eigenmode structures of streaming sausage, kink, and tearing instabilities. Plasma is assumed to be compressible with a sheared flow. Adapted from Wang et al. (1988). **b**) Results of the modeling of unstable eigenmodes in the triple current sheet. The magnetic vector potential for the three main types of modes. Adapted from Dahlburg and Karpen (1995)

and Lui (1997). Modern numerical simulations suggest that a wavy form of the solar magnetic equator leads to the occurrence ripples at the HCS, which can be observed at 1 AU (Merkin et al. 2011). The latter was foreseen by Wilcox et al. (1980).

Figure 8a (the upper panel) shows three streaming modes of instabilities developing in the HCS, according to the pioneering work by Wang et al. (1988). Plasmoids may be formed as a result of instabilities occurring in a single current sheet. Since the HCS-HPS system consists of many aligned current sheets, there are even more opportunities for the creation of 3-D plasmoids (or 2-D magnetic islands) within the HPS. One may finds an analysis of stability of the system of three closely located current sheets in a study by Dahlburg and Karpen (1995).

The chosen topology imitated a situation typical for densely packed coronal streamers, which, as we know, take part in the formation of the HPS further downstream. Dahlburg and Karpen (1995) assume that the main magnetic field is slightly disturbed by an additional perturbation magnetic field, and solve the system of MHD Orr-Sommerfeld and Squire equations, modeling the behavior of the system. The three most probable configurations of the system resulting from the developed instabilities and formation of plasmoids are shown in Fig. 8b.

In the absence of very strong disturbances (such as ICME passages), Alfvénic turbulence has always been considered as the main source of the instabilities of the HCS. Malara et al. (1996) showed that Alfvénic fluctuations also lead to the enhancement of level of density perturbations around the HCS (see also Primavera et al. 2019).

Numerical modeling allows suggesting that there is one more important source of plasmoids/magnetic islands associated with dynamical processes at current sheets in the solar wind, which is magnetic reconnection (e.g., Eastwood et al. 2002, 2007; Drake et al. 2006, 2010; Greco et al. 2016; Huang et al. 2017; Zheng and Hu 2018). Numerous simulations and observations of reconnecting current sheets describe the creation of SMIs or plasmoids as a natural consequence of this dynamical process (e.g., Matthaeus and Lamkin 1985, 1986; Matthaeus et al. 1984, 2015; Wan et al. 2013; Xia and Zharkova 2018, 2020). Combining the knowledge of the variable topology of the HPS, and the complex structure of the HPS filled

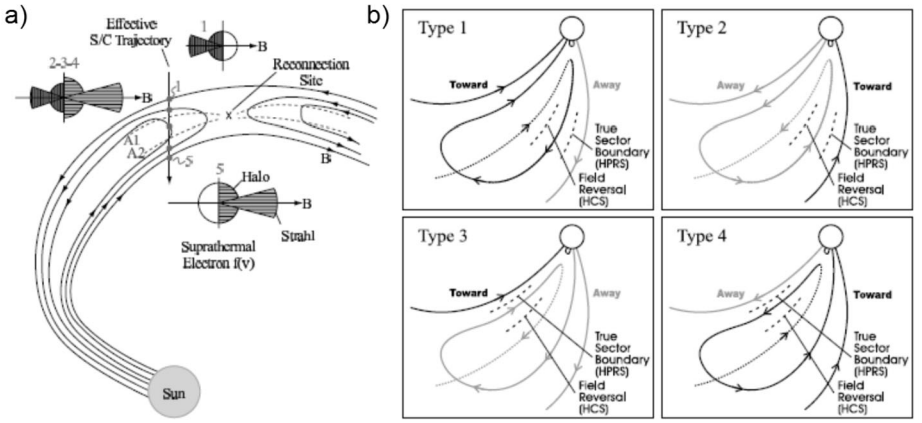

Fig. 9 Historical attempts to explain observations of closed magnetic field lines and the strange behavior of strahls near the HCS. **a**) Petschek-like reconnection at a single point and consequent tearing of the HCS. Adapted from Gosling et al. (2006); **b**) Entangling and bending of the HCS far back to the Sun according to Crooker et al. (2004). This was the way to explain events similar to that shown in Fig. 6b

with current sheets and magnetic islands with rotating magnetic field inside, one can reconstruct and explain features of the crossings of the HCS which were previously considered to be puzzling and required very complex interpretations.

It had been thought for a long time that magnetic reconnection occurs in the solar wind predominantly at singular sites of thin current sheets in a Petschek-like manner, which supposed consequent tearing, moving back to the Sun and restoration of the current sheet similar to the terrestrial magnetotail (e.g., Gosling et al. 2006). Generally, the HCS was not considered as a structure able to reconnect often, being too thick, too stable, and rarely displaying the typical features of a Petschek-type reconnection, such as the presence of narrow reconnection exhausts nearby (see, for example, Gosling et al. 2005a, 2005b, 2006 and references therein). Although the common occurrence of plasma/IMF structures with closed magnetic field lines and a time of crossing typical for magnetic islands was admitted in most of Petschek-type-reconnection studies, all attempts to explain the rotation of the magnetic field vector were fixed on connection of IMF structures to the Sun (see Fig. 9). Among different hypotheses, the following two were accepted as dominant: (i) tearing of the HCS and the moving of the formed huge loops back to the Sun and in the opposite direction (Fig. 9a), and (ii) the mentioned large-scale bending and entangling of the entire HCS or single loops produced by reconnection (Fig. 9b) (see for example, Crooker et al. 2004; Foullon et al. 2009; Owens et al. 2013 and references therein).

The common features of those hypotheses were that they repeatedly appeared in publications only in a form of sketches since there was no evidence found from modeling for such a behavior of the HCS.

Attempts to simulate such configurations of the IMF lead to loss of the suggested large-scale picture owing to instabilities immediately developing at a current sheet in the flowing solar wind and leading to tearing, pinching and breaking magnetic field lines at an early stage of simulations. Finally and even most importantly, extremely large scales suggested in the sketches did not correspond to relatively small-scale structures with closed field lines (crossed from minutes to 2 hours).

Meanwhile, in time, it has been realized that the HCS may not show Petschek-type reconnection features because the reconnection instead proceeds stochastically, which leads

to a dramatically different picture in observations. Numerical experiments and observations have shown that magnetic reconnection may occur at numerous places along the whole body of a reconnecting current sheet with a non-zero width and a complex fine structure, which consequently produces 3-D plasmoids (or magnetic islands in a 2-D cut). The idea that magnetic reconnection in cosmic plasmas is not steady but stochastic or turbulent was introduced in 2-D by Matthaeus et al. (1984) and Matthaeus and Lamkin (1985, 1986), and in 3-D by Lazarian and Vishniac (1999). Despite its closeness to reality and ability to explain observations, it took the community more than 20 years to accept the complexity of the nature of reconnection in space plasmas (e.g., Drake et al. 2006, 2010; Greco et al. 2010; Lazarian et al. 2012, 2020; Kowal et al. 2012; Markidis et al. 2013; Eriksson et al. 2014; Khabarova et al. 2015, 2016, 2018a, 2020; Lapenta et al. 2015, 2018; Pucci et al. 2017, 2018; Malova et al. 2017; Xia and Zharkova 2018; Adhikari et al. 2019). The 3-D way of reconnection seems to be the optimal and most realistic because (i) cosmic plasmas with large Reynolds numbers tend to be turbulent, which suggests a formation of X- or null-IMF points in all directions, and (ii) the large Reynolds number makes reconnection fast and allows the production of all the effects that are observed near reconnecting current sheets or within a chain of plasmoids/blobs/magnetic islands (see detailed explanations in Cassak et al. 2009; Lazarian et al. 2020).

Figure 10 illustrates the main achievements in the understanding of magnetic reconnection occurring in realistic space plasma conditions. It should be noted that numerical simulations have played the leading role in the development of this branch of space physics. In this particular area, observational studies and experimental confirmations followed the theoretical studies. Figure 10a shows the simulation of stochastic magnetic reconnection triggered by weak turbulence in the presence of the guide field (Kowal et al. 2012; Lazarian et al. 2012). Most importantly, magnetic field lines reconnect in a stochastic regime at many places simultaneously. Magnetic field lines tear up at the initial null points and do not go far from the initial reconnection site, but produce a cascade of reconnection events nearby, similar to interchange reconnection at the Sun and very far from shown in Fig. 10a (Edmondson et al. 2009; Higginson et al. 2017; Edmondson and Lynch 2017). The current density in the reconnecting current sheet is shown in the middle panel of Fig. 10a. The current flows through perturbations of the magnetic field (shown in the right panel of Fig. 10a). Lazarian et al. (2012) note that despite the approximate location of the main current sheet being near $B_x = 0$, its profile is very irregular.

This scenario is typical for all numerical simulations, and it has been convincingly explained from the theoretical point of view by Uzdensky and Kulsrud (2000) and Uzdensky and Loureiro (2016), who showed that (i) even if magnetic reconnection is initially Petschek-like, it evolves into the Sweet–Parker type within a few Alfvén times (Uzdensky and Kulsrud 2000), and, (ii) in turn, Sweet–Parker current sheets are very unstable owing to the development of the tearing instability generating a chain of plasmoids/magnetic islands (Uzdensky and Loureiro 2016).

Uzdensky and Loureiro (2016) conclude that Sweet–Parker current sheets cannot survive for a long time in real systems, which means that neither Petschek- nor Sweet–Parker magnetic reconnection can dominate in the real space plasma. This agrees very well with laboratory experiments (see Furno et al. 2005; Gekelman et al. 2012, 2016, 2018 and references therein). Also it means that experimental observations of Petschek-type reconnection exhausts are just the smallest part of signatures of a complex 3-D process occurring at reconnecting current sheets in the solar wind.

Figure 10b displays results of the numerical experiment based on a similar idea of the initial Harris-like current sheets experiencing the impact of weak turbulence in solar wind-like

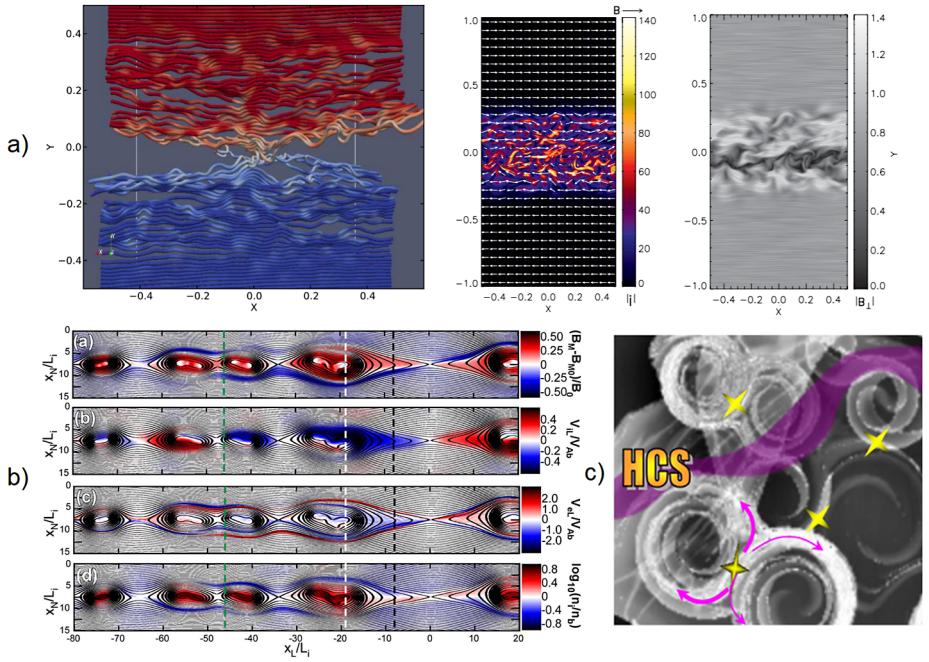

Fig. 10 Stochastic or turbulent magnetic reconnection and reconnection-borne magnetic islands. **a**) Results of modeling of a reconnecting current sheet affected by turbulence in the presence of the guide field directed perpendicular to the page (adapted from Lazarian et al. 2012 and Kowal et al. 2012). Left panel: magnetic field lines of the opposite direction (shown by blue and red colors) beginning to reconnect stochastically in many places. Central panel: intensity of the electric current (blue – minimal, and yellow – maximal) at the stage of the developed reconnection. Direction of the magnetic field lines is shown by small arrows. Right panel: Magnetic field at the reconnecting current sheet; corresponds to the middle panel. **b**) 2.5-dimensional fully kinetic implicit particle-in-cell (PIC) simulations explaining observations of magnetic islands and reconnecting current sheets in the solar wind (adapted from Eriksson et al. 2014). Simulations are made in the right handed orthogonal MNL system (M = N × L). From top to bottom: out-of-plane (M-component) magnetic field relative to a background finite guide field; L-component of the normalized ion velocity; L-component of the normalized electron velocity; Relative ion density. **c**) Sketch illustrating the presence of numerous reconnecting small-scale magnetic islands in the 2-D cut perpendicular the HCS. Adapted from Adhikari et al. (2019)

conditions, and quickly evolving into the chain of magnetic islands separated by smaller-scale current sheets. The numerical experiment carried out by Eriksson et al. (2014) was dedicated to the comparison of PIC modeling results with the first direct multi-spacecraft observations of magnetic islands associated with reconnecting current sheets in the solar wind. All prior in situ observations of magnetic islands were carried out in the magnetospheric plasma, sometimes in incredible detail unreachable in the solar wind far from the Earth, because of the inevitably single-spacecraft way of taking measurements in the heliosphere (e.g., Eastwood et al. 2007; Lui et al. 2008; Teh et al. 2010; Borg et al. 2012). Evidence for the occurrence of a flux rope near the HCS at 1 AU was first provided by Eastwood et al. (2002), and later Khabarova et al. (2015, 2016) and Enžl et al. (2017) analyzed the HCS crossings associated with magnetic islands.

Figure 10c is a sketch illustrating the idea that the HCS is surrounded by numerous dynamical magnetic islands (Adhikari et al. 2019). Following the logic of the presented material, there should be a population of magnetic islands drifting from the corona (see

Bemporad 2008 and Susino et al. 2013) and another population which originates from magnetic reconnection constantly occurring at numerous places on the HCS and/or simply comes from the development of instabilities in the HCS and surrounding current sheets (see above). Figure 10c shows the HCS as a purple stripe, and yellow diamonds indicate magnetic reconnection taking place at smaller-scale current sheets separating magnetic islands. Since the HCS is a part of the HPS system, and the edges of the HPS are strong current sheets too (Kislov et al. 2015), the area filled with plasmoids and secondary current sheets is even larger than the HPS. Therefore, one may conclude that observations of unusually prolonged crossings of the HCS/HPS system at 1 AU can be determined by (i) topological properties of the HCS/HPS system, i.e. its width, bending or rippling, and (ii) the properties of plasma structures filling and surrounding the HCS/HPS system, which, in turn, depend not only on the ambient plasma conditions and topology but also on the way, and how effectively, magnetic reconnection occurs at the HCS and within the HPS region.

Summarizing, the HCS and similar large-scale current sheets of the solar origin are unique objects since their source, the Sun (or, to be more exact, the main solar magnetic neutral line), never disappears. This, in particular, makes the HCS a very robust structure able to restore quickly after any large-scale impact such as the passage of ICMEs, CIRs/SIRs, and interplanetary shocks (e.g., Khabarova et al. 2015, 2016, 2017b, 2018a; Adhikari et al. 2019). Both in situ and indirect observations of the last several decades suggest that the HCS is rather a dynamical object than a simple passive plain or slowly waving plasma disk. The HCS carries bending waves, kink waves and ripples, experiences 3-D stochastic magnetic reconnection, accelerates particles and consequently produces a lot of effects that would not be possible to detect if the HCS was a simple large-scale discontinuity separating interplanetary magnetic field (IMF) of different polarities, as it was treated some time ago (see Lazarian et al. 2020; Khabarova et al. 2020, and references therein).

Twenty years ago, ideas appeared that the nature of many of the observed HCS/HPS properties was determined by several dynamical processes that might develop either simultaneously or in some combination. The processes have been supposed to be magnetic reconnection, instabilities, and formation of current sheets and magnetic islands. According to contemporary studies, these effects indeed exits and lead to enrichment of the HCS-HPS system and its vicinity with numerous plasmoids as predicted by simulations and observed in the solar wind (see Cartwright and Moldwin 2008, 2010; Khabarova et al. 2015, 2016, 2020; Maiewski et al. 2020 and references therein).

We conclude that question 1 (Q1) can be answered easily by combining the knowledge of the presence of the wide turbulent HPS surrounding the HCS and of the occurrence of plasmoids/flux ropes (often described as SMIs in 2-D) produced both in the corona and via dynamical processes within the HPS. It is obvious that it is possible to observe various types of crossings of the HCS, from fast to very prolonged, depending on the properties of the HPS, which are the HPS large-scale form, its inclination to the ecliptic plane, the level of disturbance, the consequent reconnection rate, and characteristics of magnetic islands and secondary current sheets associated with the HCS-HPS system. It should be noted that the occurrence of magnetic islands with closed magnetic field lines is crucial for the development of processes related to local acceleration and propagation of energetic particles in the solar wind. This will allow us to answer question 2 (Q2) and question 3 (Q3) below, after the discussion of the role of plasmoids (2-D SMIs) in particle acceleration.

2.1.2 *Quasi-Stable Current Sheets Associated with ICMEs, CHs and SIRs/CIRs, and Their Relation to Flux Ropes/Plasmoids*

Coronal mass ejections (CMEs) quickly evolve in the solar corona and propagate beyond it into the interplanetary space in the form of expanding ICMEs. It has been obvious from the very beginning that the shape, the internal structure and peculiarities of the eruption of a certain CME determine the properties of its interplanetary counterpart to a high degree. Therefore, knowledge of the dynamics of CMEs in the corona is very important. The understanding of the structure of solar prominences as 3-D plasma objects that experience twists, pinching, kinking, and finally, becoming subjects for magnetic reconnection and ejection involves employing an idea about so-called flux ropes, which represent a set of magnetic field lines forming an analyzed filament in the corona.

The twisting of magnetic tubes becomes obvious at the early stage of their rising from beneath the photosphere to the corona and may play a critical role in triggering the CME eruption (e.g., Kuznetsov and Hood 1997, 2000; Forbes et al. 2006). Figure 11a shows a filament experiencing twisting and kinking, as observed by the Solar Dynamics Observatory (SDO) in the transition region (see explanations about the SDO mission on https://www.nasa.gov/content/goddard/how-sdo-sees-the-sun). The corresponding movie is available from Helioviewer: https://helioviewer.org/.

Such a configuration of the magnetic field that finally leads to an eruption has been simulated numerically in many works (e.g., see Török and Kliem 2005; Bemporad 2011; Gibson 2018 and references therein). Aulanier et al. (2010) presented results of 3-D MHD numerical reconstructions of an evolving flux rope of a similar form within the framework of the so-called flux cancellation model. The system of magnetic field lines in the corona was initially built as current-free but finally it clearly showed an induction of the strong electric current in the central part of the twisting loop (see the black areas in Fig. 7 of Aulanier et al. 2010) owing to non-stationary processes impacting the flux rope rising to a critical height at which the reconnection and eruption occurred as a result of the torus instability. Aulanier et al. (2010) also indicate magnetic surfaces of zero current, separating regions of oppositely-directed currents, and show the temporal evolution of magnetic field lines within the flux rope. The same can be found in Fig. 11b for the case of a highly-twisted erupting flux rope, time evolution of which is shown in three panels, and Fig. 11c represents the corresponding map of the vertical velocity (Nishida et al. 2013).

Therefore, the existence of a strong current sheet inside ejected CMEs, and consequently, ICME magnetic clouds, has been known for a long time. It has also been confirmed that strong 3-D current sheets and blobs/plasmoids occur in the corona after a CME release, feeding its trailing part (e.g., Webb et al. 2003; Vršnak et al. 2009; Susino et al. 2013; Lin et al. 2015; Kwon et al. 2016; Kim et al. 2020; Lee et al. 2020).

The process of the transition of a CME into an ICME, and its subsequent propagation through the inner heliosphere, was unclear in the earliest years of the space era, but fortunately, it is visible nowadays owing to the combined analysis of coronagraphic and heliospheric imagers. One can enjoy comparing the images and movies while tracing CMEs/ICMEs from the corona to ~ 1.5 AU on many websites dedicated to space weather (see some examples below).

We can especially recommend the EIT MPEG Movies Archive at https://www.ias.u-psud.fr/eit/movies/, the Helioviewer at https://helioviewer.org/; 3-D density reconstructions from the Solar Mass Ejection Imager (SMEI) that observed the solar wind in white light (http://smei.ucsd.edu/new_smei/index.html); 3-D reconstructions of the key solar wind parameters based on the ground-based interplanetary scintillation (IPS) data provided by STELab or

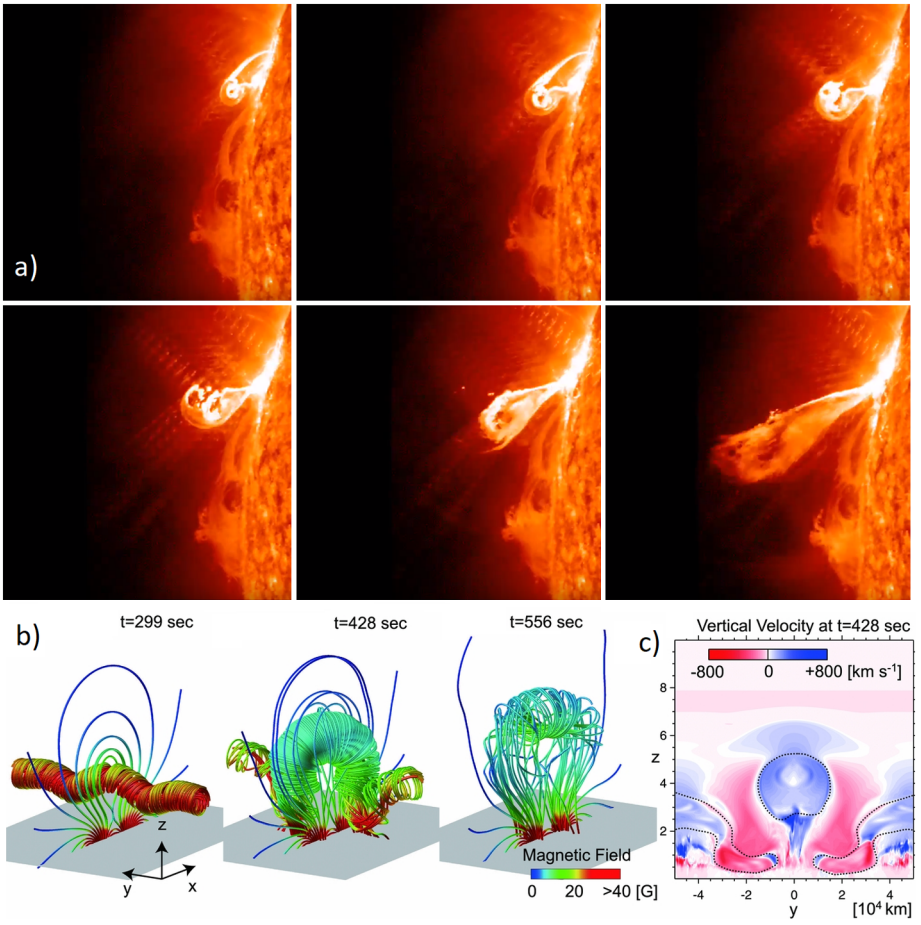

Fig. 11 Evolution of a prominence in the solar corona. **a**) Twisted and swirled flux rope observed during the course of M 3.6 class on February 24, 2011. Six snapshots from SDO AIA 304 Angstrom taken from 07:28:20 UT to 07:33:32 UT are available as a movie on https://helioviewer.org/. **b**) 3-D numerical reconstructions of magnetic field lines forming an erupting flux rope, shown at different stages of the eruption process. Magnetic field intensity is indicated by color from deep blue (zero G) to red. There is a magnetic separator in the middle of the flux rope. **c**) The corresponding map of the vertical velocity. Adapted from Nishida et al. (2013)

STEL at https://ips.ucsd.edu/ (also, see the key information on how the IPS technique works here: https://www.pstep.jp/news_en/nuggets23en.html); the STEREO images at the UK Solar System Data Centre: https://www.ukssdc.ac.uk/solar/stereo/data.html and the DREAMS by the University of Science and Technology of China at http://space.ustc.edu.cn/dreams/shm/index.php, and the mix of information from ENLIL reconstructions and white light observations from STEREO at the HelioWeather resource http://helioweather.net. The latter two resources represent useful tools, allowing one to quickly analyze movies from different data providers.

Since our view of the solar corona from the Earth is 2-D, there were long debates about whether CMEs/ICMEs represent 3-D domes preceded by a shock (Fig. 12a, left panel) or if those are expanding 2-D loops or 3-D flux ropes (Fig. 12a, right panel). Detailed expla-

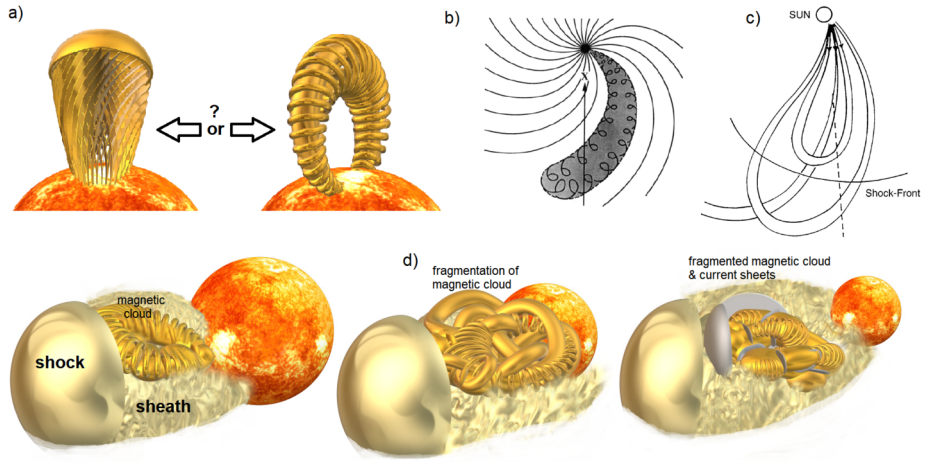

Fig. 12 Evolution of understanding of the 3-D nature of ICMEs and their substructure (in sketches). **a**) Illustration of views on a possible ICME structure (3-D version of Fig. 6 of Chen 2017 based on suggestions from Hundhausen 1999). Reflection of the prolonged discussion of 70th–90th of XX century: "Dome of twisted magnetic field lines vs loop". Later, the loop was replaced with a twisted flux rope as shown in the right panel. **b**) Helicity of the ICME magnetic cloud suggested by McComas et al. (1992). **c**) Multiple ICMEs co-existing in the interplanetary space (adapted from Malandraki et al. 2000). In both cases **b**) and **c**) the magnetic cloud is suggested to be an elongated flux rope. **d**) Fragmentation of kinking, twisting and writhed flux ropes into smaller-scale plasmoids leads to formation of current sheets, plasmoids and magnetic reconnection within ICMEs. From left to right: a typical view on the ICME structure; fragmentation of the magnetic cloud; formation of plasmoids with a complex magnetic helicity separated by small-scale current sheets (grey). Large quasi-stable current sheet is formed between the ICME sheath and the main body of the ICME

nations can be found in Chen (2017). So far, the view on this point is that since theoretical reconstructions of CMEs/ICMEs as toroidal magnetic flux ropes restore dynamics of the observed structures in the best way, CMEs are very likely 3-D flux ropes at least at the beginning of their journey, as shown in the right panel of Fig. 12a.

Two of numerous 2-D sketches illustrating the general understanding of the ICME topology observed at the Earth's orbit presented in the literature can be found in Fig. 12b and 12c. Figure 12b stresses the fact that magnetic field lines of the ICME main body are not simply aligned with the main axis direction of the flux rope, but twist and/or writhe, following the peculiarities of the helicity of the erupted CME (McComas et al. 1992). Figure 12c illustrates attempts to interpret a complex multi-ICME case, suggesting connection of the ICMEs to the Sun (Malandraki et al. 2000). Magnetic clouds are shown as loops in both Fig. 12b and 12c.

According to these views, it has been thought for years that under a rough and simplified approach, an ICME can be treated as an expanding nearly-round or slightly elongated flux rope formed by twisted magnetic field lines (e.g., Luhmann et al. 2020) as shown in the sketch in Fig. 12d, left panel. It may be deflected or compressed from one side because of the interaction with the slower ambient solar wind but the general form is suggested to repeat the ejected CME flux rope shape.

The inner part of an ICME or the flux rope is also called the "ICME magnetic cloud" in the community of observers. The flux rope is preceded by an ICME-driven interplanetary shock shown as the front semi-spherical cut in Fig. 12d. Interplanetary shocks are known as a source of strong turbulence in the heliosphere (e.g., Zank et al. 2015; Kuznetsov and Osin 2018, 2020). The turbulent wake is formed downstream of the shock, i.e. between the

shock and the magnetic cloud (see the cloudy area behind the shock in Fig. 12d). It is also called the "ICME sheath" because of its similarity to the planetary magnetosheath and the heliosheath (e.g., Siscoe and Odstrcil 2008; Richardson 2011). The undisturbed, initially formed flux rope is shown by gold in Fig. 12d, analogous to Fig. 12a.

The 2-D sketches of earlier works similar to those shown in Fig. 12b and 12c actually pointed out the 3-D properties of magnetic clouds, which have far-reaching implications. One of those is a formation of strong current sheets within ICMEs. First of all, even in the simplest case shown in Fig. 12b, a twist of magnetic field lines may lead to kinking and pinching of the magnetic cloud, which becomes fragmented into several large-scale plasmoids. Furthermore, ICMEs propagate into the medium with a variable density, filled with waves and intermittent structures. As a result, ICMEs experience numerous impacts, which often leads to the transformation of their shape into well-known "pancakes" (see, e.g., Odstrčil and Pizzo 1999; Shiota and Kataoka 2016 and references therein). If so, the internal part of the pancake flux rope with magnetic field lines of a dramatically different direction inevitably experiences magnetic reconnection. The same occurs if there is a large-scale writhe of the flux rope, which leads to formation of internal current sheets and, finally, magnetic reconnection of the internal parts of the flux rope, which initiates a cascade of reconnection events leading to further fragmentation of the magnetic cloud.

The increasing complexity of the propagating ICME with distance, that leads to fragmentation occurring in magnetic clouds of different topologies, is illustrated in the middle panel of Fig. 12d. As a result, flux ropes/magnetic bubbles/plasmoids separated by current sheets are formed within the main body of the ICME (see the right panel of Fig. 12d). The largest and strongest current sheet separates the ICME sheath from the fragmented flux rope (all current sheets are indicated by grey).

An idea about fragmentation of a single ICME flux rope into multiple flux ropes was clearly stated for the first time by Owens (2009), although prior studies had suggested pinching and distortion of magnetic clouds (e.g., Suess 1988) as well as formation of current sheets in different parts of ICMEs and even CMEs in the very beginning of CME propagation throughout the corona. Dasso et al. (2007) concluded that a quasi-stable current sheet should form around an entire CME flux rope; Moldwin et al. (1995) claimed that magnetic reconnection still occurs within an ICME far away from the corona; Foullon et al. (2007) reported observations of a strong current sheet between the edge of the ICME sheath and the magnetic cloud; Gosling et al. (2007) noted the occurrence of reconnecting current sheets in the trailing edge of an ICME, etc. (for more examples see Owens 2009, and references therein). Further investigations of the substructure of ICMEs confirmed the presence of current sheets and signatures of magnetic reconnection in all parts of ICMEs (Chian and Muñoz 2011; Steed et al. 2011; Xu et al. 2011; Zhou et al. 2011; Zharkova and Khabarova 2015; Khabarova et al. 2016, 2017b, 2018a; Kilpua et al. 2017; Khabarova and Zank 2017; Hosteaux et al. 2018; Wang et al. 2018; Adhikari et al. 2019; Zhou et al. 2019) as well as the occurrence of a twist and/or writhe of magnetic field lines in magnetic clouds, which is especially strong in the middle (e.g., Al-Haddad et al. 2011; Hu et al. 2014).

The twisted and writhed ICMEs are practically indistinguishable since the real 3-D form of magnetic field lines is very complex, and there still is no way to see all details in white light (Al-Haddad et al. 2019). More about theoretical aspects of magnetic helicity, twist and writhe of magnetic field lines, and measures of topological complexity can be found in Berger (2009). We would like to note that real conditions in which ICMEs propagate lead to far more complex magnetic cloud topologies than suggested by Owens (2009).

The 3-D simulations of the magnetic field topology and spatial evolution of key plasma parameters within ICMEs confirm the ultimately 3-D nature of ICMEs and, consequently,

the complexity of processes occurring in them (e.g., Kataoka et al. 2009; Vandas et al. 2010; Lugaz and Roussev 2011; Shiota and Kataoka 2016; Manchester and Van Der Holst 2017). Figure 13 shows examples of 3-D reconstructions of ICMEs initially defined as simple spheromak-type flux ropes propagating in the conditions close to those observed in the solar wind plasma.

Figure 13a depicts magnetic field lines of a spheromak-type ICME that reached the Earth orbit (Kataoka et al. 2009), Fig. 13b shows MHD simulations of the speed and magnetic field lines of an ICME impacted by Alfvenic turbulence 2 hours after the launch (Manchester and Van Der Holst 2017), and Fig. 13c reconstructs a sequence of two ICMEs, one of which passes the Earth's orbit (Shiota and Kataoka 2016). Despite different codes and different boundary conditions used in the simulations, it is clear that complex patterns and entangling of magnetic field lines suggest the formation of non-planar current sheets and the consequent occurrence of magnetic reconnection within ICMEs, although the studies do not focus on this particular aspect of the ICME propagation.

One of the most important recent reconstructions shows the evolution of an ICME as an object dynamical at all scales (Hosteaux et al. 2018). Hosteaux et al. (2018) reveal peculiarities of the formation of numerous magnetic islands and current sheets within the entire CME at different distances from the point at which shearing begins. Figure 13d, adapted from Hosteaux et al. (2018), illustrates this process, showing magnetic field lines and the current density within a single propagating CME.

The level of complexity of the internal structure of an ICME strongly depends on the history of its propagation in interplanetary space. In the beginning of the space era, ICMEs were treated as huge freely-expanding structures. However, high-speed streams and flows of different origins co-exist in the solar wind, strongly impacting each other, which often leads to non-radial trajectories of ICME propagation (e.g., Gopalswamy et al. 2009; Khabarova et al. 2016; Malandraki et al. 2019; Shen et al. 2019; Heinemann et al. 2019).

One can imagine the situation when one CME overtakes the other, previously-ejected but slower CME. In this case, the ICMEs merge into a conglomerate with an extended ICME sheath, an easily recognizable second shock within the sheath and a very complex fragmented main part as observed at 1 AU (Liu et al. 2014; Lugaz et al. 2017). Most ICMEs observed at farther distances represent very complex structures preceded by several shocks still distinguishable or completely merged into one beyond the Earth's orbit (Malandraki et al. 2019). This is how complex ICMEs filled with large-scale quasi-stable current sheets and rather large-scale magnetic islands can be formed.

One of the most frequently occurring situations in the solar wind are ICME-SIR interactions which also may happen at the early stages of the CME propagation which leads to the CME-CH flow interactions (e.g., Jian et al. 2008). It has been noticed more than ten years ago that this is likely the main source of the ICME deflection in the interplanetary space (see Gopalswamy et al. 2009; Wang et al. 2014 and references therein). Figure 14 gives a notable example of such an interaction which would be difficult to imagine within the frame of the 2-D paradigm of the freely expanding solar wind that carries non-interacting ICMEs and SIRs to farther distances.

Reconstructed density 3-D maps based on SMEI observations show in Fig. 14 the way in which a stable, long-lived SIR deflects two ICMEs one by one, not allowing them to expand and propagate freely in interplanetary space (to see the corresponding movies, click http://smei.ucsd.edu/new_smei/index.html, "Data and Images"–"Remote view"). As a result, both streams are deflected towards the Earth direction, which sometimes causes unexpected geomagnetic storms since there is no way to predict their behavior without an operative analysis of the situation between the Sun and the Earth.

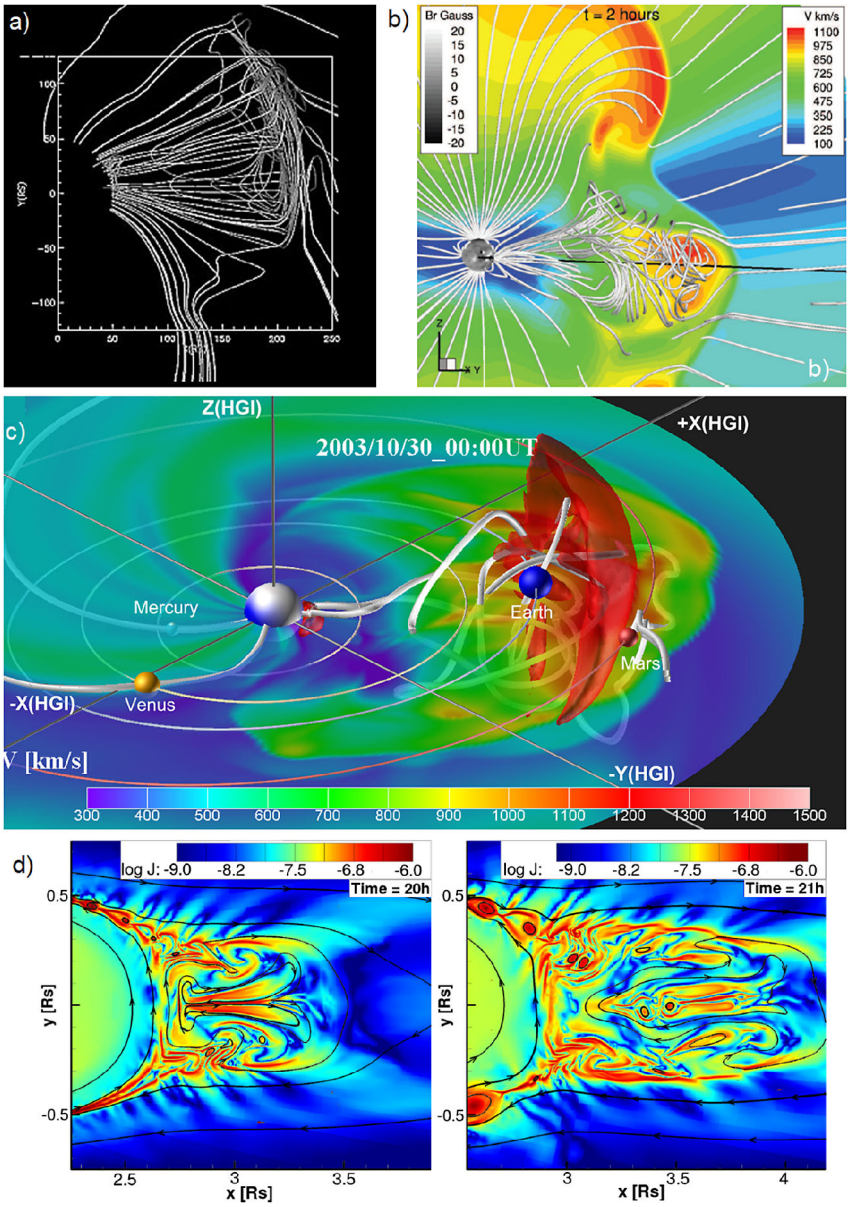

Fig. 13 MHD modeling of propagation of ICMEs in the inner heliosphere. **a**) One of the pioneering 3-D MHD modeling of ICMEs (adapted from Kataoka et al. 2009). The complexity of magnetic field lines is shown in the ecliptic plane (the Earth's position is $X = 215\ R_s$, where R_s is the solar radius). **b**) Formation of a complex flux rope within an ICME impacted by Alfvenic turbulence (adapted from Manchester and Van Der Holst 2017). The 2-hour-after-launch snapshot. Solar wind speed values are shown by different colors. **c**) SUSANOO solar wind modeling applied to ICME propagation (adapted from Shiota and Kataoka 2016). The solar wind speed is plotted analogous to **b**) in the projection onto the ecliptic plane. Magnetic field lines are grey ropes. **d**) Fractalization and formation of current sheets and magnetic islands within a CME as modeled for 20 hours (left) and 21 hours (right) after shearing begins (adapted from Hosteaux et al. 2018). Magnetic field lines are black and the current density values correspond to the color scale shown in the upper part of the panels

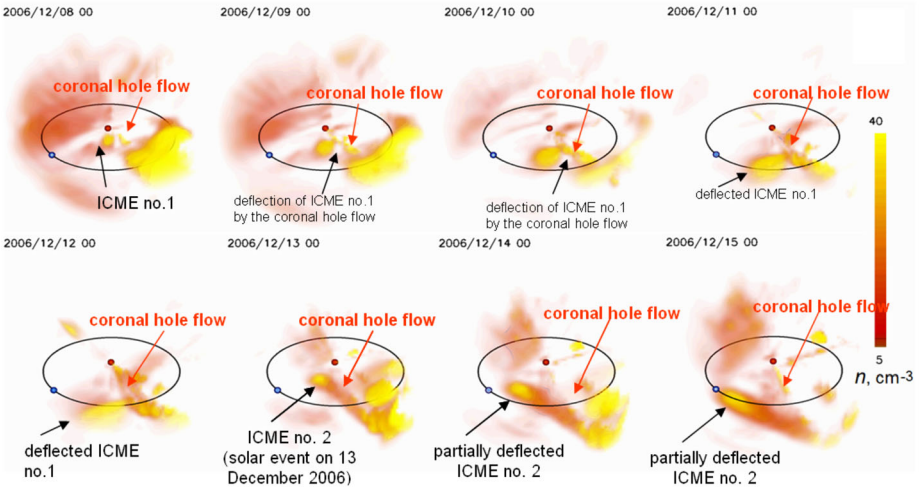

Fig. 14 Complex SIR-ICME interactions occurring in the interplanetary medium as observed by SMEI in white light SIR. Solar wind density (n) 3-D reconstructions show significant deflection of two ICMEs caused by the long-lived SIR. The streams and the flow are indicated by errors. The Sun is the red dot in the center, and the Earth is the blue dot. Adapted from Khabarova et al. (2016)

At the moment, such an opportunity exists either from IPS STEL reconstructions of the solar wind parameters or from STEREO A heliospheric imagers (see the links above). Overall, heliospheric imagery (observations in white light) and ground IPS observations are the most important tools for the analysis of the 3-D evolution of high-speed streams and flows. Altogether with computer simulations and the analysis of in situ observations of the corresponding streams/flows detected by different spacecraft, these facilities improve our understanding of details of the ICME-SIR interactions considerably (Asai et al. 1998; Jackson et al. 2009; Eyles et al. 2009; Bisi et al. 2010; Iwai et al. 2019; Barnes 2020).

Strong current sheets are formed at the edges of high-speed streams and flows (Chian and Muñoz 2011; Khabarova et al. 2016, 2017b, 2018a; Malandraki et al. 2019; Adhikari et al. 2019; Cécere et al. 2020). Since they represent magnetic walls, ICME-SIR interactions often lead to the formation of dynamically evolving closed or semi-closed magnetic cavities that play a significant role in the confinement of small-scale reconnecting current sheets, dynamical plasmoids and pre-accelerated (seed) particles filling the cavities. The confinement and compression occurring at least from one side of a magnetic cavity, in turn, increases a reconnection rate that leads to producing more current sheets and magnetic islands and excites local particle acceleration at least to MeV energies (see Sect. 3).

Another example of the stream-flow interactions can be seen in Fig. 15, showing density reconstructions from ENLIL (MHD simulations) based on the photospheric magnetic field data (Fig. 15a) and STEREO observations in white light (Fig. 15b). Figure 15a discussed by Daglis et al. (2021) represents the three subsequent screenshots of the corresponding animated reconstructions https://www.wired.com/images_blogs/wiredscience/2012/03/coronal-mass-ejection-forecast-march-5-8-2012-nasa.gif of the solar wind density predicted by ENLIL real-time MHD simulations according to the technique described by Odstrcil (2003).

The situation seen in Fig. 15a is typical for solar maximum because of the coexistence of ICMEs and SIRs interacting on their way from the Sun to 1.5 AU. The left panel is a view from the Solar North pole of the Sun, in the ecliptic plane, and the right panel is the

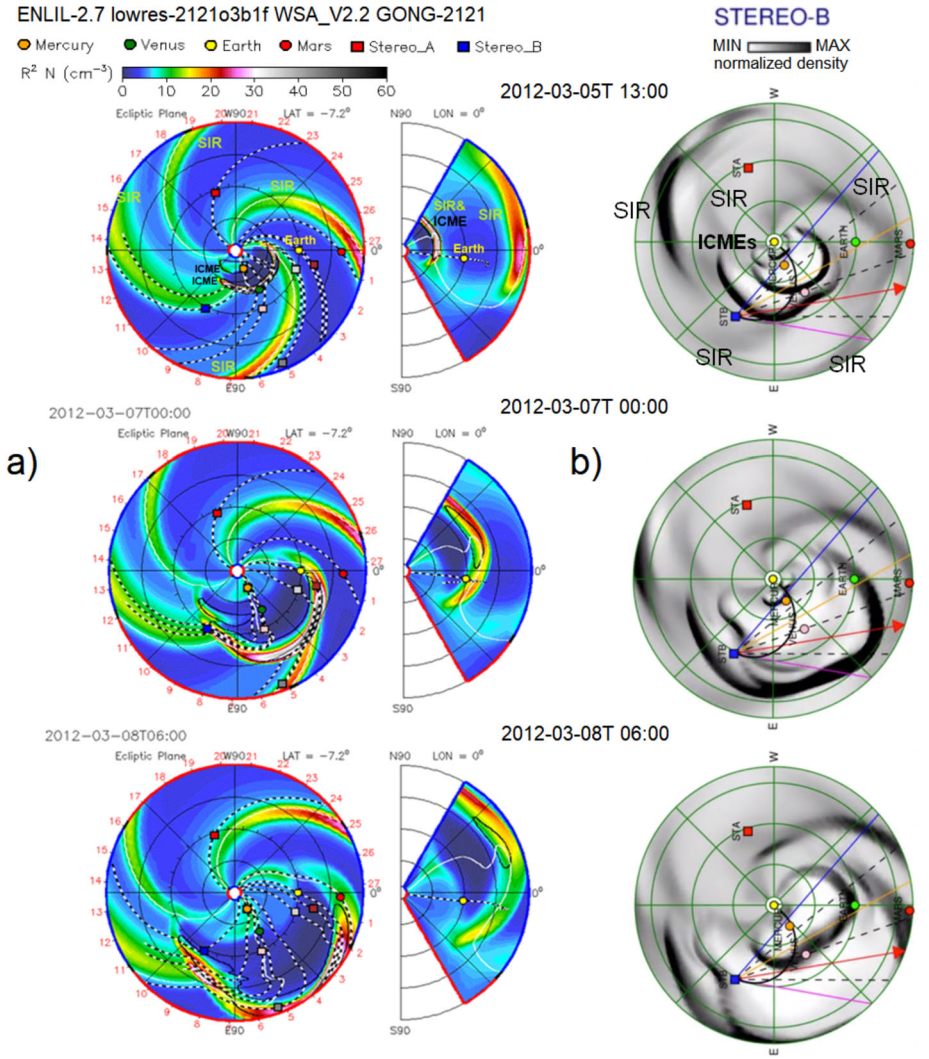

Fig. 15 Comparison of density reconstructions in the interplanetary space from the classic ENLIL MHD modeling based on the solar magentic field data and from ENLIL based on the analysis of STEREO heliospheric imager observations for the same period of March 5–8, 2012. (**a**) ENLIL modeling based on solar synoptic charts, and (**b**) STEREO B heliospheric imager observations in white light with the heliospheric imager. Adopted from Daglis et al. (2021)

longitudinal cut through the Earth position. SIRs rotate anti-clockwise, and ICMEs resemble expanding and nearly-radially propagating circles or half-circles. Figure 15a allows one to identify two ICMEs subsequently ejected, while there are also co-existing long-lived SIRs. The second ICME overtakes the first one and they merge beyond the Earth's orbit. The first ICME interacts with two SIRs, forming a complex enhanced front that is predicted to cross the Earth position, which is indicated by the yellow dot. The importance of the analysis of such simulations is in stating the fact that complex stream-flow interactions (i) lead to the formation of large-scale magnetic cavities formed by the leading edges of the streams/flows,

and (ii) may cause unexpected density enhancements and the formation of a complex and potentially geoeffective merged ICME-SIR sheath.

Note that the ENLIL reconstructions and IPS/heliospheric imagery confirm that the HCS is very elastic (see the evolution of the white line indicating the HCS in Fig. 15a). This explains the fact that an observer usually finds the first crossing of the HCS some time before an ICME or a CIR/SIR and the second crossing behind the stream/flow. However, in more complex cases, the relaxation time is not enough to allow the HCS return back to the quasi-undisturbed state, and the HCS gets pushed far away from the ecliptic plane and may not be observed by an in-ecliptic spacecraft for a long time.

Density reconstructions from the STEREO heliospheric imagers shown in Fig. 15b can be found as a movie at http://www.helioweather.net/archive/2012/03/stb1dej.html. The reconstructions based on observations of the solar wind in white light suggest that (i) the number of flows and streams seen in Fig. 15b is larger than predicted by ENLIL based on the solar data (Fig. 15a), (ii) their propagation and interaction is more complex than suggested by classic MHD modeling of the flows/streams shown in Fig. 15a, and (iii) the sequence of events develops faster than predicted by MHD modeling starting from the Sun. The accurateness of STEREO reconstructions can be checked by the comparison of the front arrivals to the Earth as seen in Fig. 15b and in situ observations (not shown). This, in particular, illustrates the fact that the same reconstruction method gives very different results being applied to different databases or based on different boundary conditions. ENLIL applied to the data obtained from the solar wind observations in white light becomes a very powerful and sensitive tool able to show a complex picture of propagation of streams and flows in the interplanetary medium.

Figure 15 illustrates the fact that various types of stream-stream and stream-flow interactions occur in the dynamical heliosphere. As noted above, the interaction of streams/flows with the HCS and each other is a way to form large-scale magnetic cavities. The latter are essentially 3-D structures bounded by strong current sheets having different shapes and moving with different speeds and in different directions. As noted above, the existence of dynamical magnetic cavities is important for the initiation of processes that finally lead to local particle acceleration because of the confinement of smaller-scale structures such as magnetic blobs/plasmoids and current sheets. Prevention of accelerated particles from leaking out of the volume ensures a higher effectiveness of all possible mechanisms of particle acceleration (from magnetic reconnection to Fermi mechanisms), which will be discussed in Sect. 3 and Part II of this review.

The evolution of CH flows and the consequent formation of CIRs/SIRs due the interaction of a rotating high speed flow with the slower ambient solar wind are far less understood and studied than the evolution of CMEs in the heliosphere. Partially, this can be explained by the larger common interest in ICMEs as important drivers of geomagnetic storms as well as them being easier to trace. Meanwhile, it is important to remember that high-speed flows from CHs and their compressed and turbulent leading part, associated with the compressed stream interface region, represent the major source of geomagnetic storms during solar minimum (e.g., Yermolaev et al. 2005). CH boundaries represent conic-like current sheets at which interchange reconnection is known to occur (Gonzalez et al. 1996; Dahlburg and Einaudi 2003; Raju et al. 2005; Edmondson et al. 2009, 2010; Gutiérrez et al. 2013; Wang et al. 2014). This topic is rather popular amongst solar physicists. There are both observations of the CH fine structure and simulations of processes occurring at CH boundaries. However, there is less interest in what happens to CHs further from away the Sun in the community. As a result, the total number of publications on this topic is considerably less than the number of articles devoted to the CME evolution. CIRs/SIRs formed in the solar wind at the

leading edge of rotating CH flows were recognized early as objects that by nature are 3-D (see Gosling and Pizzo 1999; Riley 2007; Richardson 2018).

Combining the knowledge of the facts about the CH boundary and the behavior of CH flows in the solar wind, one may suggest the view of a CH flow with a CIR/SIR forming at some distance from the corona as shown in Fig. 16a. Magnetic field lines are open and radially directed within the CH flow. Therefore, an electric current perpendicular to them occurs (black arrows). At the same time, the electric current flows along the HCS/HPS conglomerate (red arrows). CHs are known to rotate more rigidly than the surrounding corona, which means that those rotate faster than the surrounding solar wind. Furthermore, CH flows expand, and there is a velocity component perpendicular to the radial direction. As a result, SIRs/CIRs are formed mainly at the leading CH flow edge, which is obvious at 1 AU, but the opposite side SIR can be also seen, especially further from the Sun. Both structures are indicated by yellow in Fig. 16a. Importantly, the CH flow simultaneously interacts with the ambient solar wind and pushes the HCS/HPS that covers a large part of the CH flow and may be observed both very close to the SIR/CIR and rather far from it, depending on the topology of the crossing (e.g., Jian et al. 2009; Potapov 2018; Adhikari et al. 2019).

So far, the corresponding classic MHD ENLIL modeling of CH flow evolution can describe only general SIR/CIR features with the accuracy generally lower than that in the CME case (compare Jian et al. 2011 vs Wold et al. 2018). Modeling of fine structure of the turbulent region formed around the stream interface has not been performed yet. Meanwhile, it is known that all parts of high-speed flows from CHs, and especially SIRs/CIRs, contain discontinuities and high beta current sheets (e.g. Ho et al. 1996; Khabarova et al. 2018a; Potapov 2018). One can identify SIR/CIR-associated current sheets visually or use the current sheet database https://csdb.izmiran.ru to analyze properties of current sheets observed during events from the lists compiled by Lan Jian (Jian et al. 2006, 2009, 2019 see also http://www-ssg.sr.unh.edu/mag/JointMeet/Jian_SIRs.pdf).

Since CHs drift from polar regions during solar minimum to the solar equator in solar maximum, the situation shown in Fig. 16a is typical for the latter period. During solar minimum, one more important phenomenon occurs, namely, the formation of conic-like current sheets (CCSs) within polar CHs (Khabarova et al. 2017a). These current sheets practically represent large-scale magnetic tornadoes with twisted magnetic field lines protected from the ambient solar wind by an order larger current sheet at the CH boundary. In some sense, the high-latitude tornadoes resemble tornadoes observed at low latitudes (see Wedemeyer-Böhm et al. 2012) but the polar structures are far larger, created in different environment and magnetic field topologies, and live much longer (Khabarova et al. 2017a).

Ulysses in situ observations show that CCSs are characterized by a drop in the solar wind speed and a low plasma beta, i.e. they are governed by the magnetic field, and extend up to several AU at high heliolatitudes (Khabarova et al. 2017a). An analysis of the CCS fine structure suggests the existence of embedded thin CCSs in the main CCS. The sketch in Fig. 16b reflects this feature and shows the rotation of the IMF along the CCSs. These current sheets exist during solar minimum until CHs leave high latitudes. Khabarova et al. 2017a showed that Ulysses observations are in agreement with reconstructions of magnetic field lines in the corona, examples of which are shown in Fig. 16c and 16d. Small-scale (in comparison with the CH size) CCSs are indicated by blue arrows in Fig. 16c.

This view is typical for years near the solar minimum. It is easy to find, using any PFSS model (see https://ccmc.gsfc.nasa.gov/models/modelinfo.php?model=PFSS), that the indicated features at high heliolatitudes disappear when the role of the dipole magnetic field component decreases, i.e. in the periods far from solar minimum (compare Fig. 16c and 16d). Note that although the existence of the cone separatrix within polar CHs has been

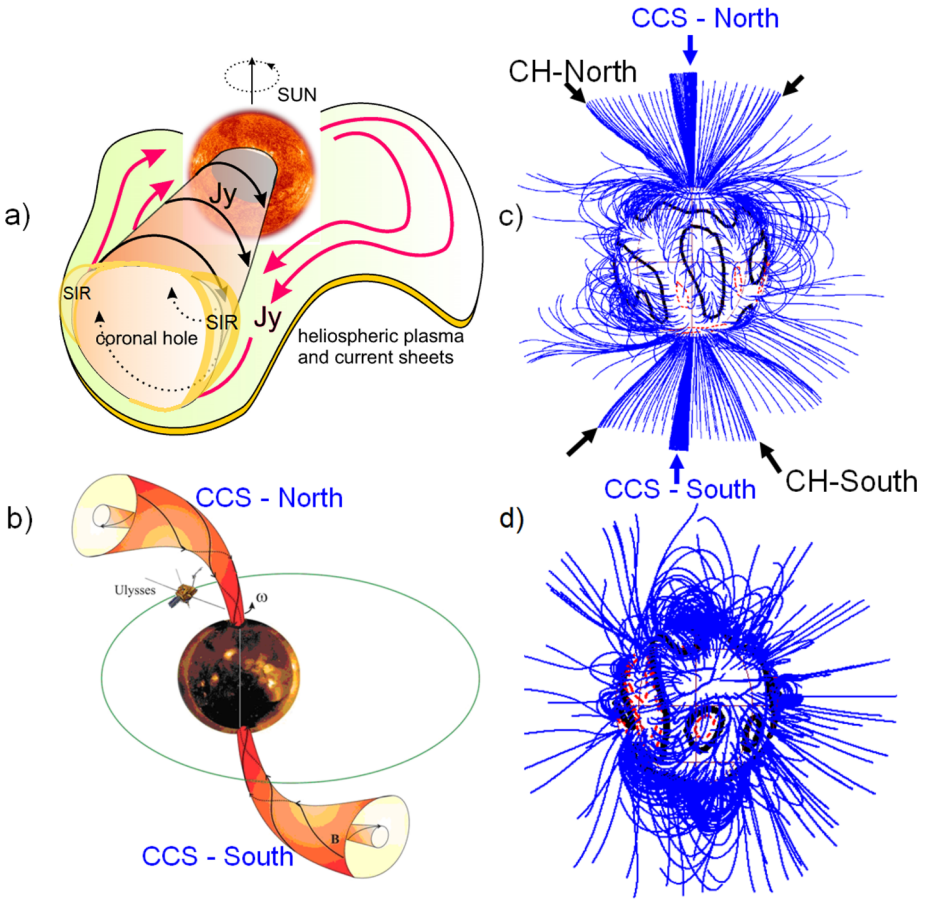

Fig. 16 Conic-like current sheet associated with CHs. **a**) Cross-equator CH flow and formation of the SIR primarily at the leading edge of the anticlockwise rotating flow in the solar wind. Situation is typical for solar maximum. Directions of dominant electric currents flowing through current sheets are shown by black and red arrows for the CH and the HCS/HPS, respectively. Modified from Riley (2007). **b**) Conic-like current sheets (CCSs) formed inside polar CHs in solar minimum as observed by Ulysses (modified from Khabarova et al. 2017a, 2017b). **c**) Example of reconstructed magnetic field lines in the corona near solar minimum, September 1994, and **d**) maximum, January 2000 (modified from Khabarova et al. 2017a, 2017b). Boundaries of CH current sheets are indicated by black arrows, and smaller CCSs inside those are indicated by blue arrows. Conic current sheets are not observed during solar maximum

predicted by Burger et al. (2008) a long time ago, recently-found polar CCSs are practically terra incognita, and a deeper understanding of their properties requires further intensive studies.

Summarizing this part, we conclude that the necessity of taking the 3-D nature of CMEs/ICMEs, CHs and CIRs/SIRs into account while interpreting observations and results of modeling gradually became one of the most actively-discussed topics of space physics (Bothmer and Schwenn 1998; Filippov 1997; Filippov et al. 2015; Antiochos et al. 1999; Russell and Mulligan 2002; Tokumaru et al. 2003; Forsyth et al. 2006; Vandas et al. 2010; Lugaz and Roussev 2011; Al-Haddad et al. 2011, 2019; Mulligan et al. 2013; Chen 2017; Slemzin et al. 2019; Georgoulis et al. 2019; Luhmann et al. 2020). Recent studies have revealed a complex

substructure of streams and flows containing current sheets and 3-D plasmoids of various scales in all their parts, which allows us to conclude that both interpretation of observations and modeling of processes associated with ICMEs/SIRs will benefit from the consideration of these structures as sources of many effects.

2.1.3 *Quasi-Stable Current Sheets in Magnetospheres, Comets and at Interplanetary Shocks*

Since the first satellite measurements around the Earth performed in the 1960s and 70s it has become evident that the Earth's dipole magnetic field actively interacts with the solar wind (Biermann and Schluter 1951; Parker 1958; Gold 1959; Gringauz et al. 1960), which leads to the formation of the giant magnetic cavity (magnetosphere) surrounding planets, inside which the solar wind plasma is deflected by the intrinsic or induced magnetic field. Normann Ness in Ness (1965) concluded from the available experimental data that the Earth's magnetosphere is a non-spherical object that can be described as a very compressed dipole at the dayside and an elongated magnetic structure at the Earth's nightside. The latter was called the "magnetotail", since it resembled a cometary tail. This simple view on the terrestrial magnetosphere is still valid, although many details were added to make the picture complete. A schematic view of the magnetosphere and its current sheet embedded in a wider plasma sheet, analogous to the HCS/HPS pair, at the magnetotail is shown in Fig. 17 in two projections.

The Earth's magnetotail is elongated at the Earth's night side to about 1000 R_E (where $R_E \approx 6400$ km is the Earth's radius). In its plane of symmetry, the electric currents of $\sim 10^6$ A are flowing in the equatorial plane from the dawn to dusk side. This large-scale current sheet self-consistently supports oppositely directed magnetic fields in a vast region named the "magnetotail lobes", and is closed over the magnetopause, representing a thin surface of shielding currents separating the planetary magnetic field from the solar wind (Sonett and Abrams 1963). At the nightside, the elongated magnetopause has a tendency to break up downstream and form a conic-like surface of a rotational paraboloid (Alexeev et al. 1996) as shown in Fig. 17a.

Observations showed that the thickness of the Earth's magnetotail current sheet depends on the state of the magnetosphere (Sergeev et al. 1993; Baker et al. 1996). In the quiet unperturbed state, the magnetotail current sheet is relatively thick, having a transverse scale of 1–2 R_E, which is far larger than the proton gyroradius ρ_i. Within a theoretical approach, it can be described as an MHD quasi-equilibrium, where the transverse magnetic inhomogeneity scales are much larger than ρ_i (Schindler 1972; Birn et al. 1975; Lembege and Pellat 1982). At the beginning of the global magnetic perturbation (called the "substorm"), when the IMF direction becomes southward and the solar wind magnetic field actively reconnects with the geomagnetic field at the dayside, the magnetotail current sheet becomes thinner to the extremely small transverse size of about one to several ρ_i (from ~ 250 to ~ 4000 km) (Sergeev et al. 1993; Baker et al. 1996; Runov et al. 2005; Zelenyi et al. 2011). This evolution from "thick" to "thin" states takes from 1/2 to 2 hours (Sergeev et al. 1996).

The final result of the current sheet evolution is the formation of the extremely thin current sheet in the Earth's magnetotail, as shown by the short red line in Fig. 17a at ~ 9–15 R_E at the earthward edge of the plasma sheet. This process plays a key role in the development of large-scale geomagnetic substorms (Zelenyi et al. 2011).

Although this TCS seems to be stable after its formation, after some time it can spontaneously be destroyed in an explosive way which is accompanied by the following processes:

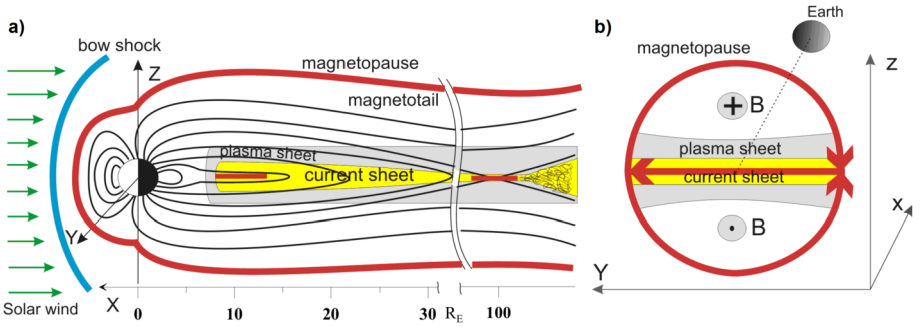

Fig. 17 Schematic view of the Earth's magnetosphere and large-scale current sheets in the XZ (**a**) and YZ (**b**) projections. Red lines are regions where satellites can observe TCSs. Flat magnetotail current sheet in the equatorial plane is closed over the conic-like magnetopause surface, creating so-called Chapman-Ferraro currents. One can identify three general regions of current sheet formation in planetary magnetospheres: bow shocks (standing waves in the foreshock region), magnetopauses and magnetotails, as shown by red lines. Hereafter, we use the standard Geocentric Solar Magnetospheric System (GSM), where the X-axis is directed from the Earth center toward the center of the Sun, the Z axis coincides with the direction of the Earth dipole and Y-axis is directed correspondingly from the dawn to dusk side

(1) magnetic reconnection (Hoshino et al. 1994; Baker et al. 2002; Runov et al. 2003; Wygant et al. 2005; Nakamura et al. 2006),
(2) the formation of a plasmoid with closed magneto-plasma configuration like the O-line between two X-lines (Murata et al. 1995; Baumjohann and Treumann 1996; Zelenyi et al. 2008a),
(3) high wave activity, and (4) the acceleration of plasma flows directed outward from this region (Ipavich et al. 1984; Zong et al. 1997; Nosé et al. 2000; Runov et al. 2006; Grigorenko et al. 2015; Parkhomenko et al. 2019). During the explosive phase, the energy of the solar wind, initially stored in the TCS, is released, which is followed by changes in the magnetic field topology and a formation of X-lines (Sharma et al. 2008).

Therefore, TCSs are triggers, switching the large-scale magnetotail dynamics regime from energy storage to its explosive release (Lui et al. 1992; Zelenyi et al. 2011). The consequent development of high wave activity after its destruction is usually accompanied by the occurrence of plasma and electromagnetic turbulence responsible for the strong plasma energization and transfer in the form of fast accelerated plasma flows along magnetic field lines (see Parkhomenko et al. 2019, and references therein).

Modern heliospheric missions (Messenger, Venus, Juno, the Voyagers and others) demonstrated that TCSs and flux ropes can be observed in the vicinity of practically all planets with the intrinsic magnetic field or without it (e.g. Slavin et al. 2007; Dubinin et al. 1991; Zhang et al. 2012a, 2012b, 2020; Arridge 2015). Generally, one can distinguish between two general sources of the magnetic field of planets:

1) The intrinsic large-scale magnetic field of the planet due to the planetary dynamo. In this category are Mercury, Earth, both giants – Jupiter and Saturn, and the distant planets (Uranus, and Neptune);
2) The external source from the induced electric current systems situated outside the planetary surface and its atmosphere. For example, there may be the ionosphere, the magnetopause, and the magnetotail current sheet determined by plasma flows originating solely from the solar wind (Siscoe et al. 2000; Lu et al. 2002; Kivelson and Bagenal

2007). Therefore, the external magnetic fields can form the induced magnetospheres of planets without or with too weak magnetic fields (e.g., Venus and Mars).

Although planetary magnetospheres are quite different in scale, their topologies are similar. It was suggested that a self-similarity scaling law could be applied for their comparison (Chapman and Ferraro 1931). Taking into account that the density of the solar wind decreases as the inverse square of the distance r from the Sun, one can estimate the relative stand-off solar wind distance:

$$\frac{D_p}{D_E} = \left(\frac{M_p R_p}{M_E r_E}\right)^{1/3} \tag{1}$$

Here, D_p, M_p, are, respectively, the subsolar radius and the dipole moment of planetary magnetospheres, D_E, M_E are the same for the terrestrial magnetosphere, and r_p is the heliocentric distance of the planet in AU ($r_E = 1$ AU). This scaling factor (1) has a universal character in the hierarchy of magnetospheric scales and might be applied also to estimate other spatial and temporal characteristics of magnetospheres of different planets for the comparison of results with observational data.

For example, the duration of substorms in the Earth's magnetosphere is usually from one to several hours, occurring approximately several times in a month. Substorm duration in the Mercurian magnetotail is about several minutes, and these happen many times in an hour (Slavin et al. 2008). About the structure one can say that the smaller the size of the planetary magnetic dipole, the simpler the magnetospheric structure and the thinner the magnetotail CS, and vice versa. The usual thickness of the current sheet in the Mercurian tail is estimated at 150 km, but for the Earth it is about 1000–4000 km (Runov et al. 2003). In the induced tails of Venus and Mars, the thickness is about 200 km and 5–300 km, respectively (Rong et al. 2014; Grigorenko et al. 2018, 2019). The TCS thickness at the Earth's magnetopause is approximately 150 km. The thicknesses of TCSs at bow shocks of planetary magnetospheres equals to several hundreds km, which is also comparable with solar wind ion gyroradii (Panov et al. 2008).

The shape of magnetotail current sheets depends on the angles of both the magnetic dipole and the rotational axis inclination with respect to the direction of the solar wind flow. Figure 18 allows one to compare typical shapes of planetary magnetospheres and their corresponding current sheets. Figure 18a shows (1) the flat magnetotail TCS formed in magnetospheres of Earth's-like planets and in magnetospheres with a small inclination angle of (0–15)°.

One can see that the magnetosphere shapes are almost similar among the inner planets of the Earth's group. The structure of the Earth's magnetosphere is the most complex among them. It has the ionosphere, the radiation belts and the ring current in the inner part (Ness 1965; Van Allen and Lin 1960; Vernov et al. 1962; Olsen 1982; Gonzalez et al. 1999). The magnetosphere of Mercury can be treated as very simple in comparison with terrestrial. It does not have the ionosphere, the ring current and the radiation belts. Because of a small dipole value, the size of the planet is relatively large and occupies almost all magnetospheric regions (Slavin 2004; Slavin et al. 2008).

The induced magnetospheres are also simpler and smaller in comparison with the terrestrial magnetosphere (Cloutier et al. 1999; Krymskii et al. 2000). They have very thin current sheets in their magnetotails, with expressed electron currents enriched by heavy oxygen ions entering the magnetotail due to following effects (Grigorenko et al. 2018, 2019): 1) photoionization of planetary atoms at the dayside be the SW; 2) mass loading of the solar wind flow by planetary ions; 3) the draping of the IMF field lines at the dayside (Zelenyi and

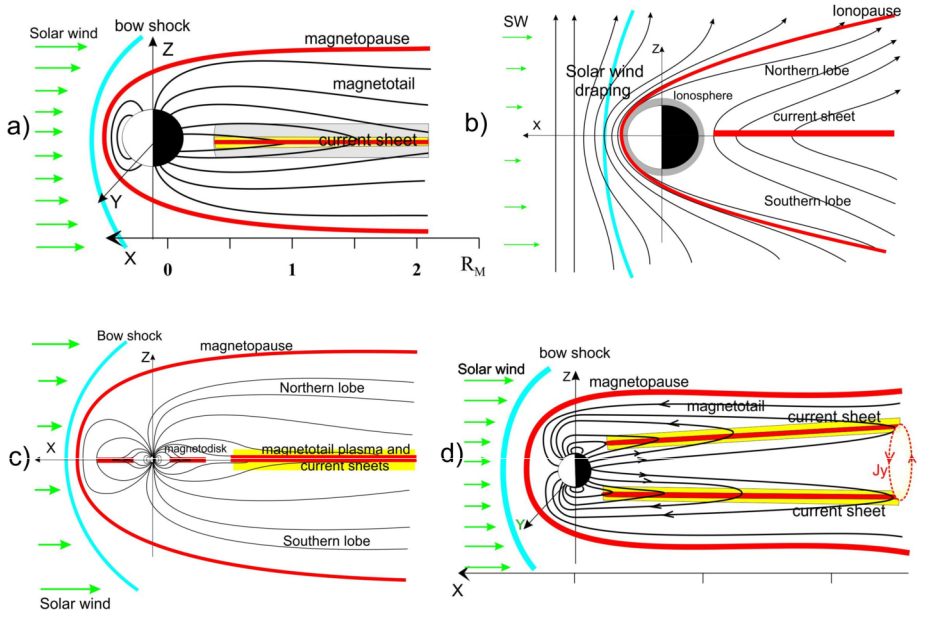

Fig. 18 Scheme of different shapes of planetary magnetospheres in the solar system: (**a**) Mercury's magnetosphere (as an example, see also Fig. 17 with the Earth's magnetosphere), characteristic for Earth's kind of planets having the proper magnetic field; (**b**) induced magnetospheres of Venus and Mars that do not have the own magnetic fields. Red lines show the possible localizations of thin current sheets. Contrary to the Mars the Venusian magnetosphere, shown in figure, has an ionosphere due to its intensive atmosphere and ionopause; (**c**) magnetospheres of giant planets (Jupiter and Saturn) that have the most complex structure among others with a thin magnetodisk in the inner part (Saturnian magnetodisk is thickened far from planet); (**d**) Magnetospheres of ice planets (Uranus and Neptune) are asymmetric due to a quite strong relative contribution of a quadrupole magnetic field; they have strongly tilted magnetic dipoles. In comparison with Uranus magnetic dipole is situated in a stable pole-on position relatively SW. The rotational axis of Neptune is tilted to about 47 degrees from the ecliptic plane, as a result every 8 hours Neptunian magnetosphere acquires the position or pole-on (Fig. 18d) or transversal to the ecliptic plane as the Earth one (Figs. 17 and 18a). In the pole-on position magnetotail current sheet has a characteristic conic (or cylindrical) shape with the closed circular current

Vaisberg 1982); and 4) the transfer of the loaded magnetic flux to the nightside, with the consequent formation of the magnetotail from IMF lines bended due to the differential mass loading (Dubinin et al. 2011).

Figure 18b depicts the characteristic shapes of magnetospheres of giant planets, namely, Jupiter and Saturn, having magnetic dipoles several orders of magnitude larger than those of terrestrial planets. Both planets have magnetotails with dynamics and magnetic substorms similar to those observed at the Earth's magnetotail, but the inner parts of magnetospheres in the proximity of the planets themselves are far more complex. Their magnetic structure is not controlled by the solar wind but is influenced by active planetary satellites, e.g. Io in the proximity of Jupiter, and Enceladus near Saturn, that enrich the inner space with ionized substances (Bagenal 2001). For fast-rotating Jupiter, with a strong intrinsic magnetic field, the processes of corotation (generation of the electric field due to planetary rotation which involves the plasma surrounding the planet to co-rotate with the same angular velocity) and the presence of small satellites as strong sources of plasma besides the solar wind could play a significant role in the formation of specific axis-symmetrical magnetodisk configurations

with a strong ring electric current of $\sim (90–160) \cdot 10^6$ A at a distance from about 20 to 50 R_J (Bagenal 1991; Khurana et al. 2004). The fine structure of the magnetodisk current in the equatorial plane of the planet cannot be described fully in the frame of the MHD approach because of the small transversal disk thickness (Zimbardo 1989; Kislov et al. 2013).

This magnetodisk current can also be a kind of TCS of a cylindrical shape considered as a tangential discontinuity under the MHD consideration. Meanwhile, there is some difference: Io contributes to the formation of a narrow ($\sim 0.1\ R_J$) magnetodisk current near Jupiter, but in Saturn's environment, the large hammer-shaped region of the trapped plasma (also called magnetodisk) is formed due to its satellite's activity (Jackman et al. 2014a; Yao et al. 2017; Sorba et al. 2018).

At the Jovian and Saturnian nightsides, the magnetotails with the flat current sheet are formed in a manner resembling those of the Earth. Note that the magnetodisk represents another kind of axially symmetric magneto-plasma quasi-equilibrium configuration in comparison with flat current configurations (Vasko et al. 2013).

Figure 18c shows also another shape of the "pole-on" dipole configuration, where the magnetic dipole lies almost in the equatorial plane and coincides with the direction of the streamlining solar wind. In this case, the conic (or cylindric) shape of a current sheet is formed with a closed current flowing over the surface of the cone. This current circuit is characteristic for distant planets with non-symmetrical magnetic fields, with a strong quadrupole component and the rotational axis deflected under a large angle with respect to the normal vector to the equatorial plane. This configuration is characteristic for distant planets of the solar system: Uranus, Neptune, and also the small planet Pluto (McNutt 1991; Bagenal 1991, 2001). Neptune's magnetosphere is the most interesting among the above-mentioned, because of the large tilt of the rotation axis of that planet. Every 8 hours its magnetic dipole-quadrupole moment takes the position or "pole-on" or transverse to the ecliptic plane (Bagenal 1991, 2001; Hofstadter et al. 2019). Thus, every 8 hours the system of magnetotail currents evolves and acquires, correspondingly, a cone-like or flat shape.

The majority of magnetospheric magnetotail CSs, except for distant planets, usually have flat configurations with reversed magnetic lines in the neutral plane (Kivelson and Bagenal 2007; Zelenyi et al. 2019). Their dimensional scales are much larger than characteristic particle trajectories near the neutral plane. A schematic representation of a flat current sheet with the proton trajectory is shown in Fig. 19.

One can see elongated and reversed magnetic field lines with corresponding trajectories of particles demagnetized in the neutral plane. The normal component of the magnetic field B_z is almost constant in the entire extent of the current sheet, while the tangential component B_x changes its direction in the neutral plane. After the current sheet crossing, initially magnetized protons go along a serpentine-like orbit in the neutral plane, after which they move away and become magnetized again. These open trajectories are called quasi-adiabatic. In the neutral plane, where the sign of the tangential magnetic component reverses, the magnetic field line curvature radius R is minimal ($R = R_{min}$) and comparable with the maximum proton gyroradius $\rho = \rho_{max}$. Particle motion in this region is governed by the adiabaticity parameter $k = (R_{min}/\rho_{max})^{1/2}$ (Büchner and Zelenyi 1989), which is less than 1 for quasi-adiabatic protons and larger than 1 for magnetized electrons.

Therefore, in planetary magnetospheres, the inherent properties of TCSs are the following:

- Thicknesses of several proton gyroradii.
- The large value of the electric current density, which might be 10–20 times larger than the background (~ 10 nA/M^2 for the Earth).

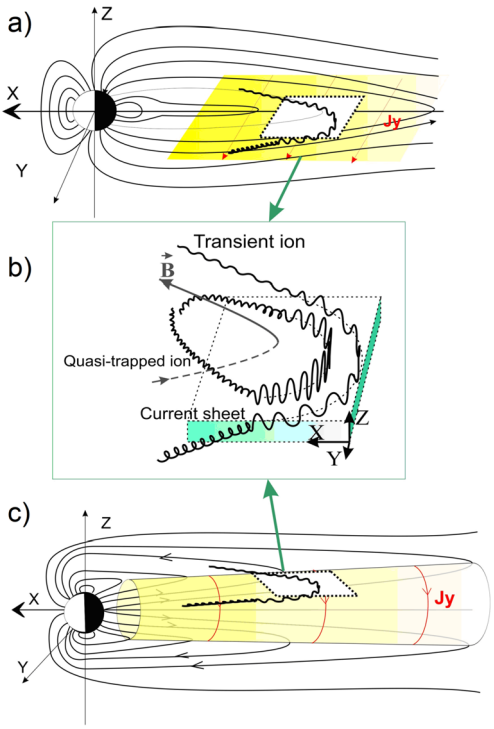

Fig. 19 Quasi-adiabatic regime of the motion of transient and quasi-trapped protons supporting thin current sheets of different shapes in planetary magnetotails: (**a**) flat configuration (terrestrial magnetosphere); (**b**) two kinds of quasi-adiabatic trajectories – transient and quasi-trapped; (**c**) possible configuration in the cylindrical magnetosphere (Neptunian, as an example)

- Very stretched shape of magnetic field lines, with the ratio of the normal to tangential magnetic components as follows: $B_z/B_x \sim 0.1$.
- Ions with serpentine-like orbits are usually the main carriers of the electric current across the sheet (Zelenyi et al. 2011, 2016). Quasi-trapped ions shown in Fig. 19 do not contribute to the total cross-tail current, but can redistribute the current density profile, leading to the current sheet thickening and formation of double-humped current configurations (Zelenyi et al. 2011). Electron currents, presumably produced by drift currents, can dominate in the narrow region of the neutral plane (Zelenyi et al. 2004). Protons following almost closed particle trajectories (called quasi-trapped) do not contribute to the total electric current. This population can only redistribute the current density (Zelenyi et al. 2002).
- Current and plasma density spatial profiles usually do not coincide, i.e. a TCS is embedded in a thicker plasma sheet (Zelenyi et al. 2011).
- TCSs can possess both classical bell-shape current profiles and have peaks or be bifurcated, triply splitted, asymmetrical etc. (Runov et al. 2006).
- TCSs are metastable structures, i.e. they may remain stable for quite a long time, but can suddenly be explosively destroyed. This leads to particle thermalization and acceleration as well as to significantly enhanced wave activity and increased turbulence (see Zelenyi et al. 2008a, 2008b; Zelenyi et al. 2011, 2016; Grigorenko et al. 2017; Parkhomenko et al. 2019 and references therein).

More details on the behavior of particles at planetary current sheets can be found in the beginning of the theoretical part (Part II) of this review.

Below, as an example of the large-scale resemblance of properties of magnetospheric and solar wind current sheets, we show Fig. 20 that allows us to compare the disk-like

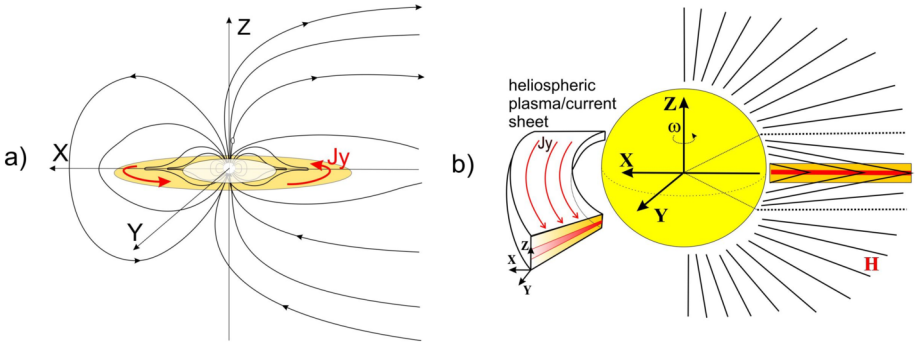

Fig. 20 Comparison of disk-like current sheets of the Jupiterian magnetodisk in the inner magnetospheric region (**a**) and the HCS (**b**). (Modified from Kislov et al. 2015)

Jovian magnetosphere called the magnetodisk (Fig. 20a) and the HCS (Fig. 20b). In a rough approximation, the similarity of these disk-like current sheets as MHD configurations can be seen despite the fact that the fine structure of the HCS is far more complex than that of the Jovian magnetodisc (Gosling et al. 1977; Borrini et al. 1981; Feldman et al. 1981; Wang et al. 1997; Blanco et al. 2006; Foullon et al. 2009).

Since the solar wind energy spectrum has a high-energy tail, the HCS can be treated as a thin structure for the dynamics of the most energetic particles for which their gyroradii are comparable with the size of the magnetic inhomogeneity. It was shown that the adiabaticity parameter for some protons with energies usual for the solar wind should be less than 1 (Malova et al. 2017). As a result, the quasi-adiabatic particles can support the existence of a TCS embedded in the thicker CS, as the HCS is embedded in the HPS. An important point is that the formation of both magnetospheres supposes the mechanism of the unipolar induction and violation of plasma corotation far from the planet/the Sun (Kislov et al. 2015, 2019).

One may notice the similarity of conic (cylindric) magnetospheric current sheets with conic current sheets associated with CHs as shown in Fig. 21 (see also Figs. 18d and 19c above). In thin configurations (with thickness about several proton gyroradii), a current sheet is supported by serpentine motion of particles along the boundary surfaces separating the solar wind plasma from magnetospheric plasma along magnetopauses and planetary bow shocks or along neutral magnetic surfaces with small field line curvature radii, e.g., magnetotails of Uranus and Neptune in the pole-on positions (Willis 1971; Olsen 1982; Glazyrin et al. 2016; Dong et al. 2018; Zelenyi et al. 2011, 2019).

As an example we consider the Chapman-Ferraro currents on the surface of the Earth's magnetopause (Fig. 21a). The thickness of the corresponding current layer is estimated as less than 300 km (Panov et al. 2008). The external surfaces of planetary bow shocks interacting with the solar wind flow also represent curved TCS structures (e.g., Cao and Paty 2017; Romashets et al. 2010; Comeron and Kaper 1998; Schwartz et al. 2011, and references therein). In the Earth's magnetotail, after the formation of the X-line in the explosive phase of substorms, giant magnetic traps (plasmoids) with plasma inside are formed, as schematically shown in Fig. 21b.

Plasmoids are structures often observed in planetary magnetotails. For example, plasmoid formation in the Venusian magnetotail is described by Zhang et al. (2012a, 2012b) (Fig. 21d). Plasmoids in the magnetospheres are similar to blobs and plasmoids observed in the solar corona and the solar wind. These represent finite closed or semi-closed surfaces.

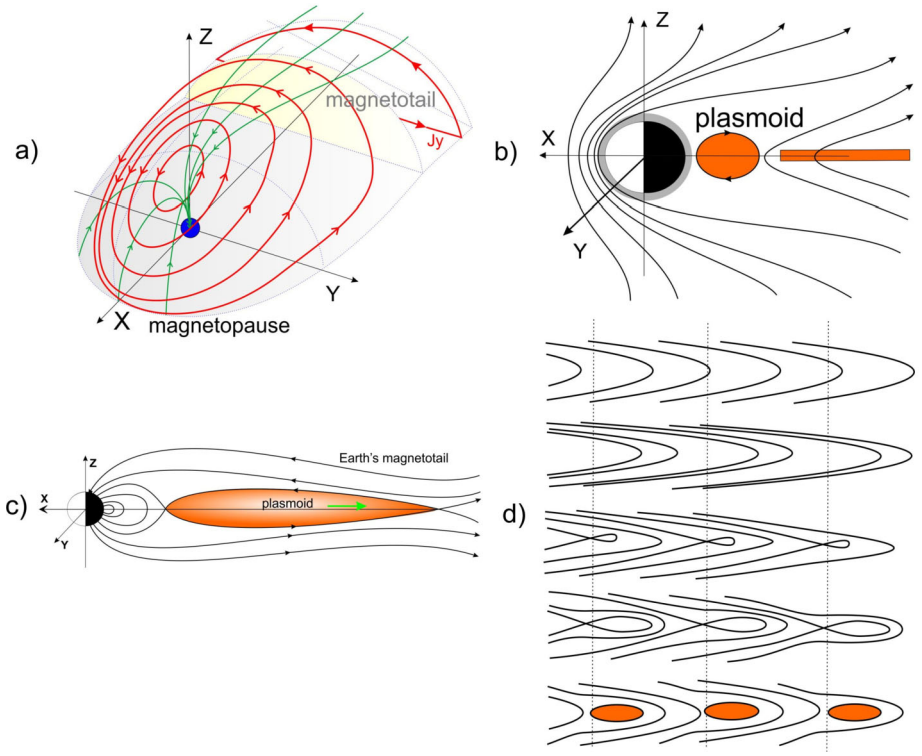

Fig. 21 Examples of formation of electric currents flowing along curved conical, cylindrical and other closed magnetospheric surfaces. (**a**) Earth's magnetopause currents; (**b**) Closed plasmoid in the Venusian magnetotail (according to Zhang et al. 2012a, 2012b); (**c**) Earth's magnetotail current sheet formed during substorms that acquires the shape of a giant magnetic bubble (plasmoid); (**d**) Possible scenario of plasmoid formation in the magnetotail configuration owing to of the development of TCS instability under tearing wave mode

In the process of their propagation, the guide magnetic field may appear, and plasmoids can take a form of elongated flux ropes. The "thick" conic-like current configurations with the transverse scale much larger than the proton gyroradius may be formed due to particle gradient currents flowing within the cusp-like magnetic field with a circular distribution of magnetic gradients like what is shown in Fig. 21a. This kind of magneto-plasma configurations can appear also as a result of closed coronal neutral lines/magnetic separators at the Sun. In the CH case (see Sect. 2.1.2) quasi-stable large-scale current sheets should occur in the solar corona as separators of the dipole and multipole solar magnetic fields (Kuijpers et al. 2015; Stevenson et al. 2015).

Although there is no information on their stability farther from the Sun, theoretically this may lead to co-existence of several conic-like current sheets at different heliolatitudes far from solar minima (Kislov et al. 2019).

QCSs analogous to magnetospheric current sheets are formed around comets, in cometary comas, and plasma tails (e.g., Yi et al. 1996; Cravens and Gombosi 2004; Volwerk et al. 2017). Interestingly, the intersection of the HCS and the cometary plasma tail was the only way to visualize the HCS in the sky before the space era. That was possible because the interaction of strong current sheets produces explosive magnetic reconnection and makes both objects visible in the radio-wave range and even in white light (e.g.,

see https://pwg.gsfc.nasa.gov/istp/events/halebopp/disconnect/, https://www.aeronomie.be/en/comet-gas-solar-radiation-forms-plasma-tail and Niedner and Brandt 1978; Brandt et al. 1992, 1997; Yi et al. 1996; Jones et al. 2000; Voelzke 2005; Jia et al. 2007; Buffington et al. 2008).

This phenomenon has been called the "disconnection event" (since a cometary plasma tail is cut off by the HCS). One can see a spectacular image of a Comet Hyakutake disconnection event in the news on 25.03.1996 at http://www.kometen.info/1996b2.htm, also described by Snow et al. (2004), and a more recent disconnection event at http://www.astrostudio.at/2_Bright%20Comets.php?img=images/2_Bright%20Comets/553_2020F8_Mosaic_04_05.jpg. Unfortunately, the effect is almost forgotten nowadays in the community of solar wind plasma physicists, and the topic is not popular anymore although it could be useful to diagnose properties of the HCS and similarly strong QCS at different heliolatitudes and distances. Note that the fact of the occurrence of current sheets in cometary comas is very important since it may explain long-debated peculiarities of the evolution of suprathermal electrons associated with comets (Khabarova et al. 2020).

TCSs are also formed at shocks in space plasmas, since the jumps in key MHD parameters at the shock front lead to creation of the cross-shock potential, and the electric current begins to flow (Cohen et al. 2019). Current sheet formation at shocks can also be enhanced due to the ion-beam Weibel instability (Matsumoto et al. 2015). Electric currents flowing along collisionless shock waves may play a role in distribution of currents in the heliosphere because both interplanetary and planetary bow shocks are very large-scale objects. This phenomenon is well-known in the magnetospheric physics for bow shocks (see Tang et al. 2009; Hamrin et al. 2018; Cohen et al. 2019; Ramstad et al. 2020 and references therein), and recently it has become obvious for interplanetary shocks as well (Cohen et al. 2019).

The latter is especially important for understanding the interplanetary shock–magnetosphere interaction process. It has been thought that a sharp intensification in magnetospheric currents during such interactions is determined only by a sharp increase in the solar wind dynamic pressure at interplanetary shocks, i.e. simply by the occurrence of a compression or pressure pulse (see Oliveira and Samsonov 2018 for a review). Taking into account additional effect of the current-current interaction may improve results of modeling considerably.

Interestingly, high-resolution measurements of the 3-D electric current, the magnetic field and plasma parameters from the Magnetospheric Multiscale (MMS) spacecraft reveal the multi-layered fine structure of interplanetary shocks (Cohen et al. 2019) as predicted by Matsumoto et al. (2015) from 3-D supercomputer simulations. As noted above, the formation of multi-layered Chinese box/nested Russian doll-like structures at kinetic scales is found to be one of the key intrinsic features of current sheets as well (Malova et al. 2017; Zelenyi et al. 2020).

Summarizing, we can stress the fact that key properties of QCSs of planetary magnetospheres, comets and shocks generally resemble properties of current sheets observed in the solar wind. Indeed, they possess similar forms, their typical width is about several proton gyroradii, their fine structure suggests existence of the electron and proton electric current layers, they are embedded in a wider plasma sheet, and finally, they are subjects of instabilities and magnetic reconnection, which may lead to various dynamical effects from plasmoid formation to particle acceleration. Therefore, we can apply our knowledge of processes occurring at planetary current sheets over a wide range of scales to current sheets in the heliosphere (e.g., Lin et al. 2008; Vaivads et al. 2012).

2.1.4 *Meta-Stable and Unstable Thin Current Sheets and Their Connection to Turbulence and Intermittency*

According to Sects. 2.1.2 and 2.1.3, the formation of secondary smaller scale current sheets at/near any strong current sheet in space plasmas is a ubiquitous process. Observations of quasi-stable current sheets in the solar wind, planetary magnetospheres and the solar corona suggest that any instability makes the current sheet broader, leads to its filamentation, and triggers turbulent or stochastic magnetic reconnection, which agrees with theoretical studies very well (see Sects. 2.1.1–2.1.3 and Che et al. 2011; Daughton et al. 2011; Eyink et al. 2011; Moser and Bellan 2012; Nishida et al. 2013; Eyink 2015; Zweibel and Yamada 2016; Srivastava et al. 2019). The latter brings even more effects, dramatically expanding the area with increased intermittency in the vicinity of the main current sheet, producing more TCSs, plasmoids and waves, and leading to local particle acceleration.

Modern views on this topic accept the idea of the 3-D nature of magnetic reconnection in space plasmas as proposed by Lazarian and Vishniac (1999), since this is supported by both observations and simulations in the most convincing way. For this process in the corona, one may find the key information about reconnection-borne structures, including plasmoids, in the series of studies by Edmondson et al. (2009, 2010); Nishida et al. (2013); Janvier et al. 2014; Edmondson and Lynch (2017).

One of the most important simulations of recent years shows that if magnetic reconnection occurs in the solar wind conditions in 3-D, it leads to broadening of the reconnection region and formation of numerous current sheets that increase intermittency within the region (Lalescu et al. 2015). Another remarkable result is about formation of 3-D plasmoids/blobs associated with the HCS at low heliolatitudes and torsional Alfven waves at high heliolatitudes (Higginson and Lynch 2018). The most comprehensive study demonstrating the necessity of considering 3-D magnetic reconnection is the recent review by Lazarian et al. (2020). Here we provide three most important arguments:

(i) 3-D magnetic reconnection is much faster than reconnection of any other type, which allows explaining observations in various plasmas.
(ii) Properties of dynamical flows in 3-D considerably differ from those in 2-D, and the exclusion of one dimension from simulations changes the course of all events dramatically, in particular, changing the direction of energy flows.
(iii) Observations show that Alfvénic turbulence induces the magnetic field wandering, which, in turn, is a key for 3-D magnetic reconnection. Meanwhile, magnetic field wandering cannot be taken into account properly in 2-D, which means that in 2-D we lose a lot of information.

Thin dynamic and short-lived TCSs can appear both via magnetic reconnection at thick quasi-stable current sheets discussed above and as a result of well-developed turbulence occurring far from structures such as the HCS and the planetary magnetotails. Current sheets evolve quickly in turbulent plasmas being involved in the turbulent cascade that suggests both generation of waves and the development of magnetic reconnection acting at many points stochastically (e.g., Greco et al. 2009; Zweibel and Yamada 2016; Kumar et al. 2017; Fleishman et al. 2020). Magnetic reconnection associated with turbulence is often considered under the 2-D approach, which sometimes is doubtful. This point is discussed in Part II of this review. Note that Oishi et al. (2015) claimed that the 3-D MHD consideration of processes shows fast magnetic reconnection as an intrinsic feature of space plasma which requires neither specific kinetic effects nor turbulence to develop.

Knowing all above mentioned, one can explain prolonged crossings of the HPS discussed in Sect. 2.1. Firstly, a wide region of magnetic reconnection-borne structures surrounds the HCS. As a result, the HPS becomes filled with boundaries that also represent two strong current sheets, and prevent TCSs and small-scale plasmoids from expanding too far from the HCS (Kislov et al. 2015). The other source of current sheets and plasmoids in the HPS is the corona, or more specifically, the streamer belt (Bavassano et al. 1997; Milovanov and Zelenyi 1994; Roberts et al. 2005; Maiewski et al. 2020). Although steamers practically do not survive to 1 AU in their original shape (DeForest et al. 2016, 2018), they feed local processes and induce the formation of current sheets along the HCS farther from the corona. Larger scale plasmoids/blobs from the corona also contribute to the HPS formation (see Sect. 2.2). Therefore, this HCS-HPS system is a self-organized structure possessing specific properties that depend on both coronal source and local processes.

Secondly, the HCS/HPS shape is sensitive to the impact of high-speed streams and flows (see Sects. 2.1 and 3 below). In situ observations show that the HPS/HCS dynamically responds to their passage or approach. As a 3-D structure, the HCS forms ripples and folds in the way of high-speed streams and after their passage (e.g., see Khabarova et al. 2015, 2016; Adhikari et al. 2019). Since the HPS is filled with current sheets and plasmoids/blobs, the region corresponding to the non-planar HCS/HPS can be crossed for hours and even days, which answers *Question 1* of Sect. 2.1.1.

In the case of the ICME-SIR interaction, the HPS can be found between them as shown in Fig. 22. Figure 22a shows typical observations of the HCS disrupted by high-speed streams/flows. The co-existence of an active region that produced the ICME and the cross-equator narrow CH in the period of the interest can be easily checked at https://helioviewer.org. The Wind spacecraft crosses the flank or trailing edge of the ICME first and then occurs within the region of the folded HPS/HCS for almost a day. The right edge of the purple stripe in Fig. 22a is the stream interface at which the density drops and the speed begins to grow within the CH flow. Then a weak SIR arrives pushed by a CH flow interrupted by the ICME, which is a typical situation caused by ICME-SIR interactions as shown in Figs. 15 and 22b, c.

Figure 22b and 22c depict the solar wind speed real-time reconstructions from ENLIL in the ecliptic plane and give an idea of the scenario for events of this kind. The flows and streams are indicated directly in the pictures, expanding ICMEs can be identified by both increased solar wind speed and the black croissant-like contours propagating almost radially, while high-speed CH flows rather remain as rotating and expanding sleeves. The red dashed line shows a cross-way of a virtual spacecraft that would observe a picture analogous to that shown in Fig. 22a. The HPS/HCS, indicated by the white line, quickly recovers after the ICME passage. A sharp increase in the solar wind density, intense variations in the azimuthal IMF angle, a drop in the IMF module, and restructuring the PAD of suprathermal electrons are expected to be observed exactly as shown in Fig. 22a. These features characterize the entrance of the spacecraft into the HPS region. Three intersections of the HPS folds, corresponding to changes in the direction of the strahl suprathermal electron flux, are indicated by numbers 1–3 in Fig. 22a and 22b, c. In Fig. 22a, multiple drops in the IMF module and variations in the azimuthal angle of the IMF are detected by the spacecraft passing through the HCS/HPS folds, inside which the PAD features indicate a change in the IMF direction $(+/-)$. Such sharp variations in the IMF parameters characterize the crossings of strong current sheets shown by vertical red lines in Fig. 22a, some of which may represent borders of plasmoids inside the HPS (see Sect. 3).

An interpretation of complex intersections (see Fig. 22) had represented a significant problem for a long time since the HCS was considered to be flat and single-layered (see

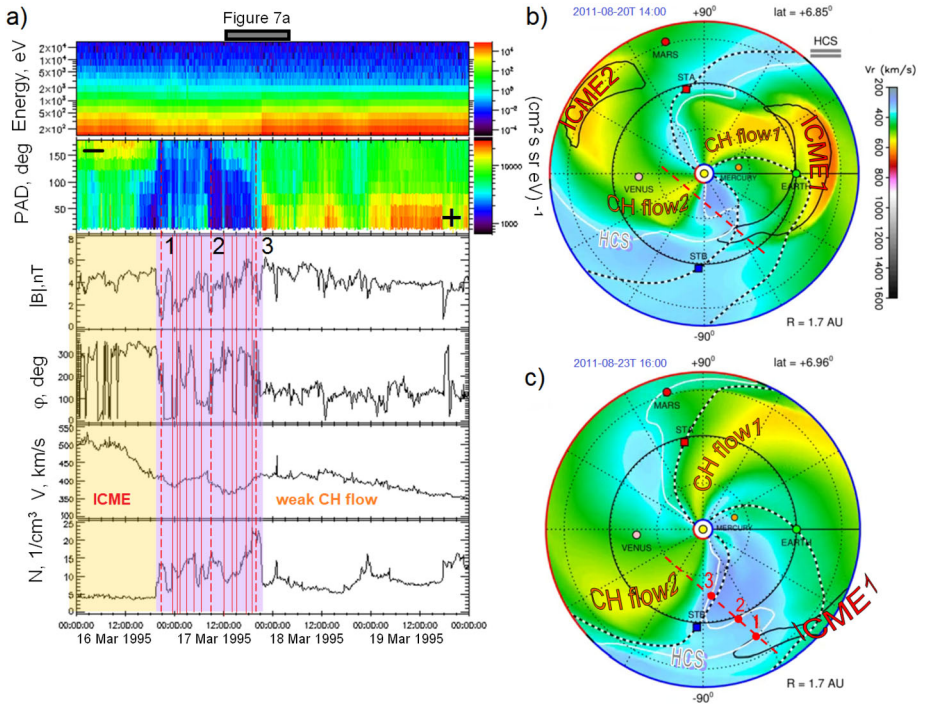

Fig. 22 Observation of the double-folded HCS/HPS filled with TCSs between the trailing edge of the ICME and the weak CH flow. **a**) Example of in situ one-spacecraft observations at 1 AU. From top to bottom: electron energy (spectrogram), pitch angle distribution (PAD) spectrogram of suprathermal electrons (255 eV), IMF module, azimuthal angle of the IMF, solar wind speed and density (data from the Wind spacecraft). Trailing part of the passing ICME is designated brown-yellow, the HPS zone is purple. The event is partially studied by Crooker et al. (2003) as an example of strange variations in the IMF and the PAD during the HPS crossing. The time period considered by Crooker et al. (2003) in corresponding Fig. 7a is shown by the black-and-grey bar above the upper panel. The HCS/HPS folding is characterized by the typical PAD changes. The sequence of crossings of the HCS/HPS folds is indicated by numbers. Multiple current sheets are observed inside the HCS/HPS system (indicated by red lines). Crooker et al. (2003) considered only crossing 3, omitting the analysis of the entire event. **b**) Solar wind speed reconstructions according to the ENLIL model for a typical CH flow – ICME interaction led to the HCS deformation (from the HelioWeather webpage: http://helioweather.net/archive/2011/08/vel3e1.html). Flows from two CHs and two ICME streams are indicated directly on the panels. HCS is indicated by white line. Red dashed line is a possible way of crossing of the double-folded HCS/HPS by a spacecraft. **c**) Analogous to **b**) but three days later. Numbers indicate the HCS crossings, by a virtual spacecraft similar to **a**). The HPS is restored after the passage of the ICME but pressed by SIR/CH flow2, forming folds across the red section line of the spacecraft

Sect. 2.1). In the most innovative studies, the presence of the flat HPS repeating the HCS shape was assumed, but attempts to present its 3-D configuration and dynamics were not successful due to the lack of alternative methods of reconstructing a 3-D picture of the studied object (see the introduction to the problem in Adhikari et al. 2019). For example, Crooker et al. (2003) considered only one of the three crossings of the HPS/HCS (namely, crossing 3 in Fig. 22a) as a single HCS crossing, which was presented as a sharp change in the presumably stable and prolonged picture of the IMF direction (see Fig. 15a). The left part of the whole picture, with multiple changes in the IMF direction for many hours, was ignored by Crooker et al. (2003) as being too complex. The period discussed by Crooker et al. (2003) is shown by the grey stripe in Fig. 22a.

Meanwhile, statistical studies show that HPS crossings can last several days mostly because of the complex behavior of the HCS/HPS affected by passing ICMEs and SIRs (Khabarova and Zastenker 2011). The longest of the crossings are obviously related to the HCS/HPS topology, an example of which is shown in Fig. 22. It is noteworthy that current sheets embedded in the HPS generally repeat the shape of the HCS, bending along with the main neutral plane.

A short summary of this section is that TCSs and plasmoids/flux ropes/blobs can be formed either near the HCS and similarly strong large-scale current sheets via magnetic reconnection or far from QCSs via turbulence. In the HCS case, there is also a population of relatively large plasmoids/blobs coming directly from the solar corona. Observations support the idea of 3-D magnetic reconnection in space plasmas. The consideration of the HPS/HCS as a 3-D structure eases the interpretation of observed events.

2.2 Flux Ropes, Plasmoids, Blobs and 2-D Magnetic Islands

The occurrence of current sheets in real plasmas inevitably leads to the development of magnetic reconnection, and, in turn, an initialization of magnetic reconnection leads to creation of magnetic bubbles/plasmoids as 3-D structures or 2-D magnetic islands representing a section of the 3-D structures. As discussed in Sect. 2.1.3, this paradigm is supported by many researchers studying physical mechanisms responsible for magnetic island/flux rope formation in space plasmas. It has been claimed that flux ropes/plasmoids/plasma bubbles occur over a wide range of plasma conditions "*wherever current sheets exist*" (Linton and Moldwin 2009). Let us discuss the terms themselves since these are sometimes used arbitrarily which may lead to misunderstanding or misinterpretation of the results of related studies.

2.2.1 Plasmoids, Magnetic Bubbles, and Plasma Blobs

Plasmoids/magnetic bubbles/plasma blobs are isolated 3-D objects with closed magnetic field lines, formed in space and laboratory plasmas (e.g., Cargill et al. 1986; Hughes and Sibeck 1987; Zhukov et al. 2000; Lin et al. 2008). In other words, plasmoids occur under nearly-relaxed conditions of magnetic helicity conservation. Under a rough approximation, they may be spherical, possess a bubble-shape, have a ring/loop or elongated cylindrical form (see Fig. 23 and Jackman et al. 2014b). Note that in the latter case they become unstable in real plasmas and experience pinching and fragmentation into plasmoids of a smaller size determined by the ambient solar wind properties. Modern numerical simulations and laboratory experiments show that plasmoids are intrinsically 3-D structures produced by 3-D magnetic reconnection. Therefore, the form of magnetic field lines inside and outside plasmoids may possess a very complex topology (e.g., Gekelman et al. 2018; Zhu et al. 2019). Figure 23a shows formation of the elongated cylindrical-type plasmoid in the magnetosphere of Saturn as modeled by Jia et al. (2012).

Contours of the vertical component of the magnetic field and field-aligned currents in the ionosphere are shown by colors indicated in the corners of the panel. Plasma density contours are shown in the equatorial plane. Another example is a so-called "field-reversed plasmoid" with a rather complex magnetic field line pattern created and observed in laboratory experiments (e.g., Slough et al. 2011; Lampasi et al. 2016). One may refer to Kirtley et al. (2011) for details. Although these structures cannot be observed visually in the magnetosphere and the near-Earth solar wind, contemporary 3-D simulations allow restoring processes leading to their formation in the magnetosphere, taking into account the Hall effect and fast magnetic reconnection (Lu et al. 2015). For example, it is found that small-scale

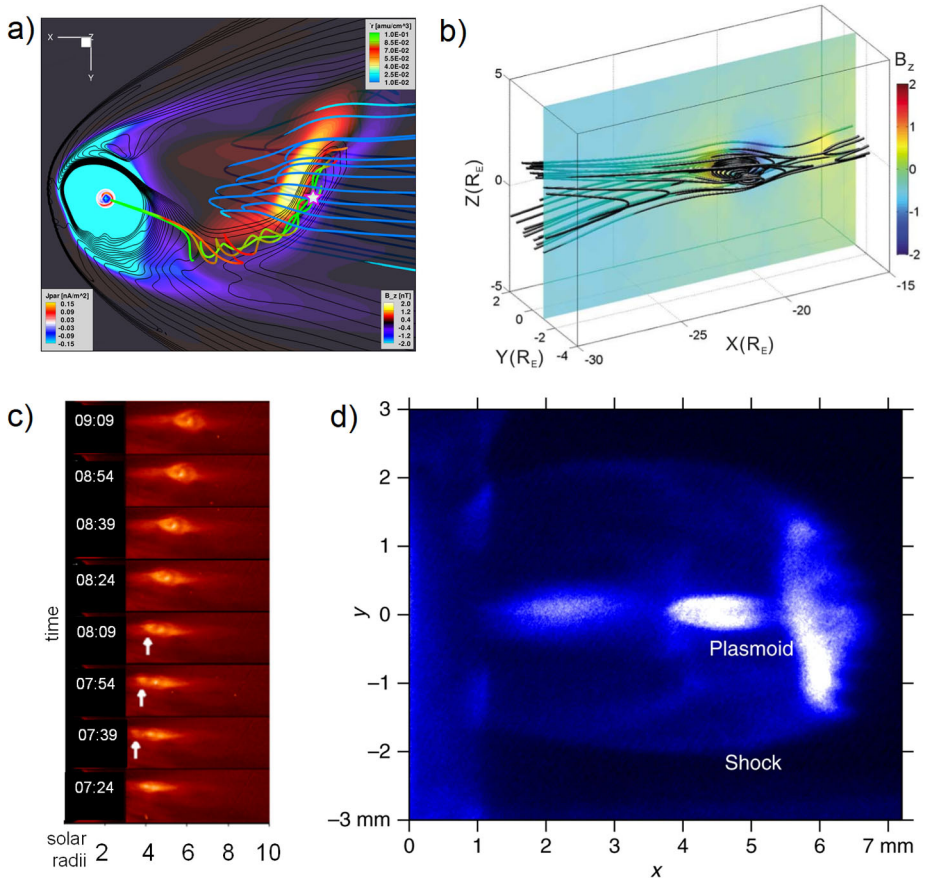

Fig. 23 Plasmoids in different plasmas. **a**) Plasmoid formation in the tail of Saturn, according to Jia et al. (2012). **b**) 3-D modeling of a plasmoid in the magnetotail representing an anti-Earthward moving anti-polarization front (adapted from Lu et al. 2015). **c**) Merging of two plasmoids (blobs) in the solar corona (STEREO A observations). Distances are given in solar radii. Sun is in the left. Smaller blob shown by the white arrow overtakes the larger blob ejected earlier. Modified from Song et al. (2012). **d**) Observation of the plasmoid and shock created by a laser jet in the 5-Torr-Nitrogen-filled chamber in the laboratory experiment (adapted from Kuramitsu et al. 2018). The laser jet came from the left 35 ns before the picture was taken, and the gas was ionized to initiate magnetic reconnection after the shot

plasmoids in the magnetotail representing Earthward propagating depolarization fronts may dynamically evolve and change their form, but their lifetime allows them to pass through tens of Earth radii. So-called "anti-dipolarization fronts", i.e. tailward-propagating plasmoids also appear as a result of simulations which are in a good agreement with observations (see a snapshot of the corresponding 3-D reconstruction in Fig. 23b).

Plasmoids occurring in the distant magnetotail are similar to those observed in the solar wind (Lepping et al. 1996). In space plasmas, plasmoids can only be visible in the solar corona, in which they are often called "*blobs*", as shown inFig. 23c (e.g., Song et al. 2012; Takasao et al. 2016; Di Matteo et al. 2019). A rare case of observation of a large rotating plasmoid seen in white light in the interplanetary medium was discussed by Khabarova et al. (2016). One can notice a striking similarity of processes occurring at the Sun with those

observed in the laboratory plasma (compare Fig. 23c with Fig. 23d representing a snapshot of the plasmoid formation owing to magnetic reconnection stimulated by a laser).

Debates whether plasmoids are real or imaginary structures in the heliosphere began with an important discussion paper by Lemaire and Roth (1981) in which they claimed that plasmoids in the solar wind and the magnetosphere differ from ideal MHD filaments, since observed plasmoids are finite in length, have a "skin" and represent surfaces at which the electron pitch-angle distribution pattern changes. The topic became very popular, and even a plasmoid model of the solar wind was developed (see Tamano 1991).

2.2.2 Magnetic Flux Tubes and Flux Ropes

Magnetic flux tubes or flux ropes have successfully been used in models describing the spatial and temporal evolution of many phenomena in space and laboratory plasmas. Flux tubes were initially introduced just as a convenient method to recalculate plasma and magnetic field parameters from one point to another. Therefore, borders of tubes consisting of magnetic field lines (as well as the rest of the flux rope body) can be chosen arbitrarily, in accordance with a certain task (see Maxwell 1861; Parker 1979; Sauty and Tsinganos 1994; Somov 2006; Archontis and Hood 2010; Ryutova 2018).

The essence of the method can be described as follows. One may choose a bundle of magnetic field lines with a surface called the "magnetic flux tube" and draw out the closed contour perpendicular to magnetic field lines in each point (see Fig. 24a). Since the magnetic field is divergent-free, the magnetic flux through the surface formed by the contour does not depend on the place where it is chosen. In other words, if A_0 is the area confined by a contour somewhere, B_0 is the mean magnetic field at the corresponding surface, A and B are, respectively, the cross-section area and the average magnetic field through the area in another part of the bundle, then $A_0 B_0 = AB$. Knowing how the cross-section of the bundle depends on coordinates, it is possible to find dependence of the magnetic field on coordinates and track it downstream/upstream. It is assumed that magnetic field lines are frozen into the solar wind plasma, which is described by the following equation, in which E is the electric field, v is the speed, and B is the magnetic field vector:

$$E + c^{-1}[v, B] = 0 \tag{2}$$

The differential rotation of the Sun is often neglected in models of the solar wind. Therefore, the transition from a non-inertial reference frame to the rotating system of reference allows removing the electric field from (2) (see, for example, Pizzo 1982). Then $v \| B$. Knowing the dependence of the function A on coordinates, one can recalculate the solar wind speed from one point of the bundle to another. Taking into account the continuity equation and the $v \| B$ rule, the momentum density ρ can also be recalculated from one part of the magnetic flux tube to another: $A_0 \rho_0 v_0 = A \rho v$. Therefore, the method allows recalculating key plasma and magnetic field parameters along magnetic filed lines from one point in space to another. The dependence of A on coordinates is usually set by means of the expansion factor (e.g., Wang and Sheeley 1990). For a better description of the solar wind, additional parameters can be employed, which allow, for example, considering the heat transfer in solar wind. Initial values of B_0, v_0, and ρ_0 are usually set near the Sun to be in agreement with in situ observations farther in the solar wind. The method is simple and well-combined with PFSS models (see, e.g., https://ccmc.gsfc.nasa.gov/models/modelinfo.php?model=PFSS; Wang and Sheeley 1990, 1992; Arge and Pizzo 2000). The flux tube concept is often used in modeling astrophysical objects and the magnetospheres of planets (e.g., Bhardwaj et al. 2001; Beskin 1997; see also

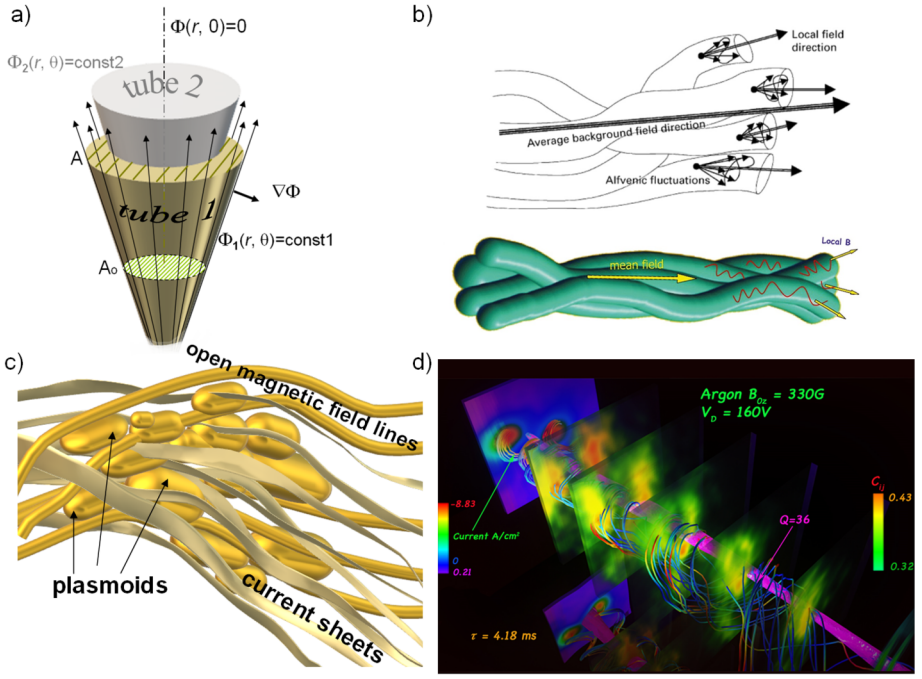

Fig. 24 Views on flux tubes/flux ropes in different branches of plasma physics. **a**) Illustration of the method of flux tubes. Two surfaces of the constant flow Φ are shown as golden and grey cones (modified from Beskin 1997). A_0 and A are the cross-sections of the flux tube. Since the velocity vector V is aligned with the Φ surfaces, the total flow of the plasma is conserved within the tubes. This approach works well in the corona, and, in the solar wind, the poloidal components of V and B remain aligned, which allows recalculating the key parameters along the tube to far distances (Kislov et al. 2015, 2019; Khabarova et al. 2018b). Flux tubes boundaries are chosen according to the task and common sense and not considered as real physical objects. **b**) Views on flux tubes in terms of interpretation of turbulence in the solar wind (upper panel is adapted from Bruno et al. 2001 and lower panel – from Bruno 2019). **c**) Sketch illustrating co-existing plasmoids and 3-D TCSs or quasi-separatrix layers in the undisturbed solar wind with IMF lines extended through the structures. **d**) Plasma currents of two flux ropes interacting in laboratory plasma (adapted from Gekelman et al. 2014). Two flux ropes with their sources on the left evolve with time and distance, collide and reconnect mostly along a 3-D quasi-separatrix layer formed (magenta) showing the so-called "chaos in flux ropes". Plasma currents are shown by colored lines reflecting the magnitude of the current density (see color scale on the left). C_{js} is the Jensen–Shannon complexity of B_y

https://wwwmpa.mpa-garching.mpg.de/~henk/mhd12.pdf). The same approach is also often applied to the processes occurring at the Sun (e.g., Yeates et al. 2015). Therefore, employing the idea about magnetic flux tubes is a way of describing changes in various parameters along magnetic field lines. A flux tube is not an isolated plasma structure and, in this sense, is no more real than the axis of rotation of the Sun or the ecliptic plane, being merely an imaginary surface.

The solar wind can be described as a fractal medium, elements of which can also be interpreted as flux tubes since multifractality is closely related to intermittency (Milovanov and Zelenyi 1999; Zelenyi and Milovanov 1992, 2004; Bruno 2019). In situ observations show that the quiet solar wind is filled with discontinuities and other coherent structures of various scales – from electron scales to hundreds gyroradii. Since it is impossible to restore a 3-D view of each structure crossed by a spacecraft from one-point observations, all

the discontinuities can potentially be treated as borders of some thin but elongated objects. Following the success of a theoretical method of flux tubes, an idea has appeared that (i) the entire solar wind consists of small-scale flux tubes or flux ropes with a width of 0.1–1 solar radius at 1 AU expanding directly from the Sun and connected to their coronal sources at any heliocentric distance, (ii) borders of magnetic flux tubes represent real structures, i.e. current sheets, and (iii) turbulent processes in the heliosphere can be explained by bending and mixing of the practically infinite small-scale magnetic tubes/ropes (e.g. Schatten 1971; Mariani et al. 1973; Borovsky 2008; Arnold et al. 2013; Burkholder et al. 2019).

This approach called the "spaghetti solar wind" paradigm is illustrated in Fig. 24b. Despite simplification of the reality, it is sometimes convenient to employ the paradigm, for example, for interpreting numerical simulations, since it practically allows converting 3-D task into 2-D (see Part II), although a question about inevitable losses of the quality of obtained information under such an approach remains open (e.g., see the discussion in Moldwin and Hughes 1991; Gekelman et al. 2018; Zhu et al. 2019 and Sect. 2.1.4).

Since it is impossible to see the solar wind by eye, and the SMEI/HI or STEL technologies have too low resolution to study the behavior of small-scale structures like flux tubes, formally, the picture of the solar wind observed in situ may correspond to both the "spaghetti" solar wind (Fig. 24b) and the solar wind representing open magnetic field lines mixed with elongated but finite dynamical current sheets, discontinuities and plasmoids embedded in the open flux as shown in Fig. 24c. Indeed, both cases suggest some impact on turbulence, determining its spatial scales and other properties. There may be related deviations from the Parker spiral, and the impact of the IMF structure on propagation of energetic particles is generally the same in both cases.

Meanwhile, there are puzzling observations which are difficult to understand if one assumes the existence of "solid-border" flux tubes rigidly connected to the Sun, but those events can be interpreted with local closed 3-D structures, current sheets and/or filamentary structures (Khabarova et al. 2015, 2016, 2020; Riazantseva et al. 2017; Adhikari et al. 2019; Malandraki et al. 2019; also see Sect. 3). Since there are many works advocating the "spaghetti" paradigm (see above), we focus below on the views about the solar wind structure as reflected in Fig. 24c. Note that we do not consider here large-scale ICMEs, CIRs and similar cases in which the existence of real large quasi-stable flux tubes or flux ropes is confirmed by different methods, including remote observations. We discuss a possibility of the solar wind consisting of small-scale spaghetti-tubes with a cross-sectional diameter of $\sim 10^5$–10^7 km at 1 AU (Borovsky 2008). This corresponds to structures with a typical angular size from one to six degrees if projected to the Sun. Could the flux tubes of this sort survive during their expansion from the solar corona? Can we see them in the corona if their borders are real?

A question about the stability of small-scale flux ropes and their hypothetical ability to reach the Earth, expanding from the Sun in a form of entangled but surviving spaghetti, arises. Observations of artificially-created flux ropes/tubes in laboratory plasmas and corresponding 3-D modeling show that initially stable and spatially well-separated flux ropes experience interactions leading to their quick restructuring, twist, writhe, pinch, merging, bouncing, repeated magnetic reconnection at many points and formation of 3-D separators, so-called quasi-separatrix layers (Sun et al. 2010; Gekelman et al. 2014, 2018). Some effects related to the natural extension and multiple interactions of flux ropes in the solar wind are not achievable in laboratory. Meanwhile, one can extend the knowledge of key features of the flux rope interaction studied in laboratory plasmas to space plasma. For example, laboratory observations suggest that magnetic helicity is dissipated within the quasi-separatrix layer region (DeHaas and Gekelman 2017).

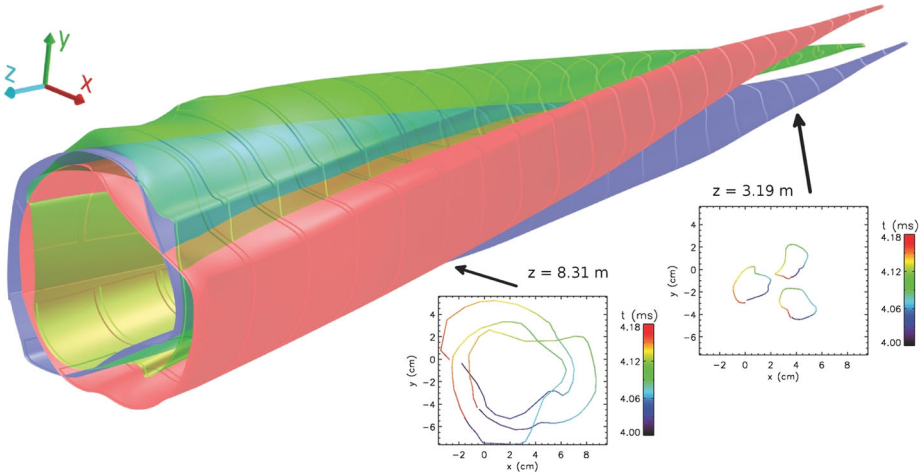

Fig. 25 Evolution and merging of laboratory flux ropes in the three flux rope case (adapted from Van Compernolle and Gekelman 2012). Surfaces swept out by the field lines at the center of each flux rope are shown by different colors. Flux ropes merge and rotate about the guide field. Cuts of the surface at certain distances from the source shown by arrows illustrate the evolution of flux ropes in 2D known as merging of magnetic islands

Figure 24d illustrates the development of the process called "chaos in magnetic flux ropes" among laboratory plasma physicists. This is the case of evolution of two flux ropes. The quasi-separatrix layer is shown in magenta in Fig. 24d. Note that this phenomenon occurs in natural plasmas and can be studied in 3-D geometry only. In the three flux rope case, more quasi-separatrix layers appear, and the flux ropes can finally merge to form a big one (Gekelman et al. 2012). A flux rope can be vizualized by both the magnetic and current density field lines. Meanwhile, note that the current field lines are strongly twisted in the poloidal direction over magnetic field lines (see Fig. 24d and Fig. 7 of Van Compernolle and Gekelman 2012). The electric currents rotate in the direction of the electron gyration, and the current channels are twisting about themselves. The surfaces swept out by the magnetic field lines at the center of each flux rope are shown in Fig. 25 for three flux ropes. Two flux ropes are found to mesh into each other, forming complex structures (see Fig. 5 of Gekelman et al. 2012), while three flux ropes may completely merge with time/distance from the source (Fig. 25). Vertical cuts show the corresponding evolution of 2D magnetic islands. The latter is an analogue of the picture observed in the solar wind since a spacecraft just crosses plasma structures along some trajectory. Therefore, the scenario of interaction of flux ropes is not only plasma property-dependent but also flux-rope number dependent. In the case of an uncountable number of flux ropes with different widths, twist properties and different orientation with respect to each other, various and more complex scenarios of flux rope merging and reconnection may develop as shown by Linton and Antiochos (2005) and Linton (2006) for realistic solar conditions (see https://online.kitp.ucsb.edu/online/solar02/linton/pdf/Linton.pdf).

There is no technique to observe flux ropes in space as 3-D objects. Only numerical simulations can help. Higginson and Lynch (2018) studied consequences of interchange magnetic reconnection that occurs in the slow pristine solar wind at low heliolatitudes near the HCS and at high and medium heliolatitudes in the so-called Separatrix-Web (S-Web) topology regions (Antiochos et al. 2011). The particular case discussed by Higginson and

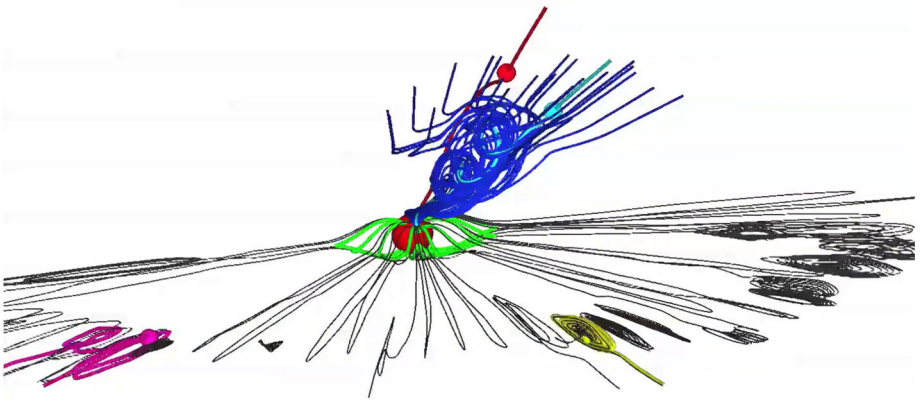

Fig. 26 3-D modeling of formation of plasmoids/streamer blobs at the HCS at low heliolatitudes and torsional Alfvén waves at high heliolatitudes. Realistic conditions at the Sun are chosen for simulations. Red blue and magenta dots are probe spacecraft at 21 solar radii. Both rotating wave in the polar solar wind and in-ecliptic blobs are created by interchange magnetic reconnection but its consequences are topologically different at high and low heliolatitudes. Adapted from Higginson and Lynch (2018). Adaptively Refined MHD Solver code developed by DeVore and Antiochos (2008) is used

Lynch (2018) was associated with an elongated coronal-hole corridor extending from the pole down to the solar equator. The Adaptively Refined MHD Solver (ARMS) code developed by DeVore and Antiochos (2008) was employed to perform 3-D simulations. The essence of the results is shown in Fig. 26 (see the corresponding animation at https://iopscience.iop.org/0004-637X/859/1/6/suppdata/apjaabc08f2_video.mp4). The figure and the corresponding movie of Higginson and Lynch (2018) illustrate an interesting fact that interchange magnetic reconnection has dramatically different consequences at low and high heliolatitudes.

At low latitudes, blobs/plasmoids actively reconnecting with the ambient solar wind propagate outward along the HCS (black), while torsional (rotating) Alfvén waves are formed in the polar region (blue). Note that only 3-D simulations could predict the occurrence of such a region seen at high heliolatitude in Fig. 26. The similarity of CCSs (tornado-like structures boarded by conic-like current sheets observed by Ulysses within the polar CH at several AU) and the rotating wave occurring due to interchange magnetic reconnection in the same region may be not random. One can compare the structure of magnetic field lines in the high-latitude torsional wave shown in Fig. 26 with Fig. 16c–d. Also the HCS blobs seen in the ecliptic plane in Fig. 26 can be compared with those shown in Fig. 21. Therefore, one may suggest that Higginson and Lynch (2018) successfully linked processes and structures occurring in the solar corona/pristine solar wind with those observed in situ far downstream.

The CH is a well-known source of the high-speed solar wind, but Higginson and Lynch (2018) has predicted the occurrence of the source of the relatively slow solar wind flow within the high-speed solar wind from a CH. One of the main features of tornado-like polar CCSs shown in Fig. 16b is a sharp decrease in the solar wind speed as observed in situ (Khabarova et al. 2017a). The occurrence of the low-speed "spots" inside high-speed solar wind originating from a CH is confirmed by different independent methods of distant observations (Bemporad 2017; Tokumaru et al. 2017). Interestingly, this finding had been treated as controversial, and the nature of this effect was unclear until its association with the conic-like polar current sheet was established (Khabarova et al. 2017a). Quite probably, these findings are linked. Adding the "Burger-Fisk solar wind" effect (Burger et al. 2008)

to the predictions of Higginson and Lynch (2018) and modeling the formation of the corresponding current sheet at the edge of the region separating twisted magnetic field lines from the ambient solar wind seen in Fig. 26 may yield the complex picture observed by Ulysses.

Well-formed plasma blobs/plasmoids are found by Higginson and Lynch (2018) in their numerical experiment to be still magnetically connected to the Sun at 20–30 solar radii. However, in real plasma, such plasma structures may detach farther downstream owing to various dynamical processes. One can apply the results discussed above to the solar wind, suggesting that flux ropes may interact, reconnect, tear up and fall into chains of numerous elongated plasmoids farther from their source in the corona since these are kink-unstable and also experience pinching (see Linton et al. 2001; Lapenta and Restante 2008 and Fig. 7 of Lin et al. 2008). This scenario questions the ability of spaghetti-like flux ropes to elongate very far from the coronal source simply representing an extension of the so-called magnetic carpet seen on the Sun (e.g., Kitiashvili et al. 2015), when flux ropes are assumed to remain untouched or entangling without interaction and formation other plasma structures in the solar wind.

The latter is supported by observational studies of flux rope evolution in the corona carried out by DeForest et al. (2016, 2018). Novel techniques employed by DeForest et al. (2016, 2018) allow visualizing structures from the STEREO inner Heliospheric Imager white-light observations in the best way and show how the solar wind flows up to tens solar radii in fine details. It has been found that radial striae that were earlier supposed to survive far from the corona in fact fade very quickly, while there is an obvious process of local formation of dense structures called "flocculation". This fact practically means restructuring the solar wind plasma close to the coronal source and suggests that turbulence and magnetic reconnection have a significant impact on the pristine solar wind even below the Alfvén radius. The latter has recently been confirmed by observations from the Parker Solar Probe mission (e.g. Chhiber et al. 2020; Zhao et al. 2020). In particular, Chen et al. (2020b) estimated the turbulence-associated energy flux to be $\sim 10\%$ of the bulk solar wind kinetic energy at 0.17 au, and the value quickly increases to $\sim 40\%$ at the Alfvén radius.

Summarizing, the laboratory and numerical experiments as well as in-situ observations suggest the course of events that leads to co-existence of open magnetic field lines, elongated flux ropes, plasmoids, and magnetic separators (small-scale current sheets) in the solar wind as shown in Fig. 24c.

2.2.3 Magnetic Islands

The term "magnetic flux ropes" should be used with caution. Magnetic islands are treated as a 2-D representation of both plasmoids/blobs and flux ropes/magnetic tubes. Indeed, one may find that perpendicular cuts of plasmoids/blobs as well as flux ropes/tubes shown in Figs. 24 and 15 give very similar pictures of closed magnetic field lines. Moldwin and Hughes (1991) examined magnetic field configurations observed in situ and interpreted those as either plasmoids or flux ropes. They concluded that it is impossible to distinguish between the two types of structures using single spacecraft observations. From this point forward, some misuse of the "magnetic flux rope" and "plasmoid" terms begins. For example, since the "spaghetti solar wind" paradigm is very popular, researchers have some preset picture of processes in mind before they carry out a study. As a result, single-spacecraft observations of the rotating magnetic field vector may be interpreted as "magnetic flux ropes" without taking into account the fact that the structures observed are merely assumed to be flux ropes, but may be plasmoids instead. Even multi-satellite measurements may give a wrong impression of a flux rope observation instead of a plasmoid, if the latter is elongated and its length exceeds the spatial resolution of the set of satellites.

So far, many researchers prefer to speak of "magnetic islands" in 2-D configurations or specify that 2-D cuts of all elongated 3-D structures are treated as "flux ropes" (see Zank et al. 2014, 2015; le Roux et al. 2015, 2016, 2018; Le Roux et al. 2019, 2020 and Part II of this review). The simplest method for identifying magnetic islands from single-spacecraft measurements of plasma and IMF parameters is based on detection of intense anti-correlated variations in the IMF and the plasma density, combined with specific changes in both the IMF components and the IMF angles, characterizing rotation of the IMF vector. The latter can be found via a hodogram method often used in the magnetospheric physics but rarely applied to the solar wind (see Khabarova et al. 2015; Khabarova and Zank 2017; Malandraki et al. 2019). The method is based on the analysis of patterns of the IMF vector projections on the three perpendicular coordinate planes.

An example is given in Fig. 27a and 27b (adapted from Khabarova et al. 2015). It was a case of the prolonged complex HPS crossing with poor correlation between the PAD features and the IMF features similar to Fig. 4b. The event can be found in the SBC list compiled by L. Svalgaard (http://wso.stanford.edu/SB/SB.Svalgaard.html). Multi-spacecraft observations of merging SMIs surrounding the HCS were analyzed with ACE and WIND, which were 150 Earth radii apart. The largest islands are indicated by color stripes in Fig. 27a. A clear rotation of the IMF vector in the region filled with magnetic islands is seen in IMF hodograms (Fig. 27b). One can find that a crossing of the HCS, not complicated by approaching high-speed streams, is associated with energetic particle flux enhancements (see Fig. 27b), which is quite typical for such events. The study showed the associated particle acceleration (see the three lower panels in Fig. 27a).

Another method to identify magnetic islands is a Grad-Shafranov reconstruction of the spatial profile of the local magnetic field. The method has been employed for investigations of properties of magnetic islands in the terrestrial magnetosphere for more than two decades (e.g. Sonnerup and Guo 1996; Hau and Sonnerup 1999; Hu and Sonnerup 2003).

Studies of the last decade show a boom in applications of this technique to the solar wind (Trenchi et al. 2013; Hasegawa et al. 2014; Hu et al. 2014; Hu 2017; Chen et al. 2018; Zhao et al. 2018; Zheng and Hu 2018; Malandraki et al. 2019; Pecora et al. 2019). An example is shown in Fig. 27c. Magnetic islands reconstructed from Ulysses observations at ~ 5.3 AU, and their sizes can be estimated as being about 10^{-3}–10^{-2} AU. There is a database of flux ropes (magnetic islands) identified via the Grad-Shafranov method from the ACE, Wind and Ulysses data created by Jinlei Zheng, Qiang Hu and Yu Chen (http://fluxrope.info).

Then, there is a magnetic field rotation analysis (MRA) method based on four-point measurements of the magnetic field (e.g., Shen et al. 2007) and a newly-created method of reconstruction of the 3-D distribution of quasi-separatrix layers (the so-called QSL method) which is potentially useful for identification and reconstruction of plasmoids from in situ observational data (see Zhu et al. 2019).

A typical size of magnetic islands observed at different distances from the Sun obviously varies because the solar wind expands, the IMF strength decreases, and characteristic gyroradii become larger with radial distance. Figure 28 focuses on spatial characteristics of magnetic islands associated with the HCS only. Observations show that sharp changes in the solar wind plasma presumably corresponding to the edges of magnetic islands are observed for days around the SBC day (Khabarova and Zastenker 2011), and the detailed analysis by Cartwright and Moldwin (2010) allows one to conclude that magnetic islands are observed within the interval of up to ± 4 days around the HCS, with a prominent peak on the HCS crossing, i.e. the SBC day (see Fig. 28a). The mean size of the magnetic islands vs heliocentric distance reported by Cartwright and Moldwin (2010) is shown in Fig. 28b by circles, and values predicted by Khabarova et al. (2015) for various distances are indicated by diamonds. The derived semi-empirical formula is shown directly in the panel. The averaged

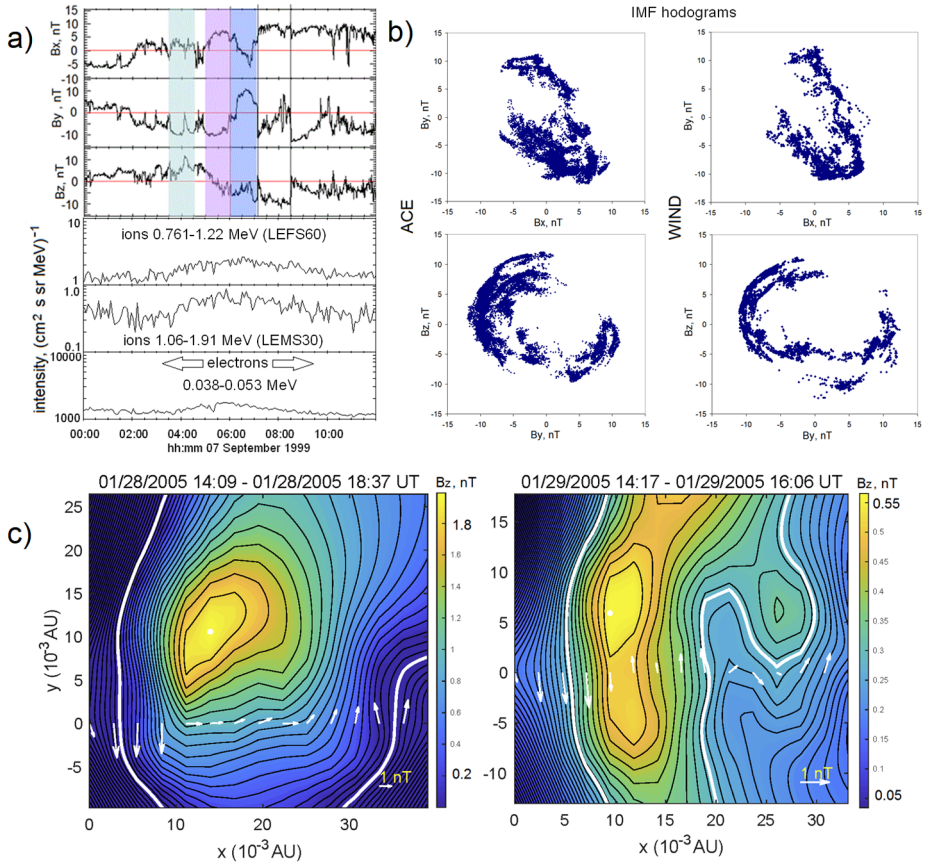

Fig. 27 Examples of identification of magnetic islands in the solar wind. **a**) Prolonged HPS crossing observed by ACE and WIND (modified from Khabarova et al. 2015). The IMF components show significant variations around zero (ACE observations). The largest islands are indicated by color stripes. The crossing is associated with enhancements in the energetic particle flux up to 2 MeV (ions) and 0.1 MeV (electrons) as shown in the lower three panels. **b**) Hodograms showing rotation of the IMF vector observed by the ACE and WIND spacecraft during the crossing of the islands indicated in **a**). The spacecraft are 150 Earth radii apart. **c**) Sample of the Grad-Shafranov reconstruction of magnetic islands. Cross-section maps of the local magnetic field rotating in small-scale magnetic islands of different sizes. The intensity is shown by color. Adapted from Malandraki et al. (2019)

IMF strength at the corresponding distances is taken from multi-spacecraft estimations by Khabarova and Obridko (2012). Note that Fig. 28b shows only averaged values; and deviations from the mean at each heliocentric distance can be several times larger (see Cartwright and Moldwin 2010 for details). For example, magnetic island crossings at 1 AU last from minutes to hours, i.e. their sizes fall in the range of 10^{-3}–10^{-2} AU.

The understanding of how their typical size varies with distance is important for theoretical predictions of the characteristics of turbulence, which in turn determines the scattering coefficients and thus the propagation of cosmic rays and solar energetic particles in the heliosphere (Engelbrecht 2019).

Ignoring details, vast areas filled with magnetic islands can be created by turbulence in the solar wind (see explanations about the link between turbulence and magnetic islands in

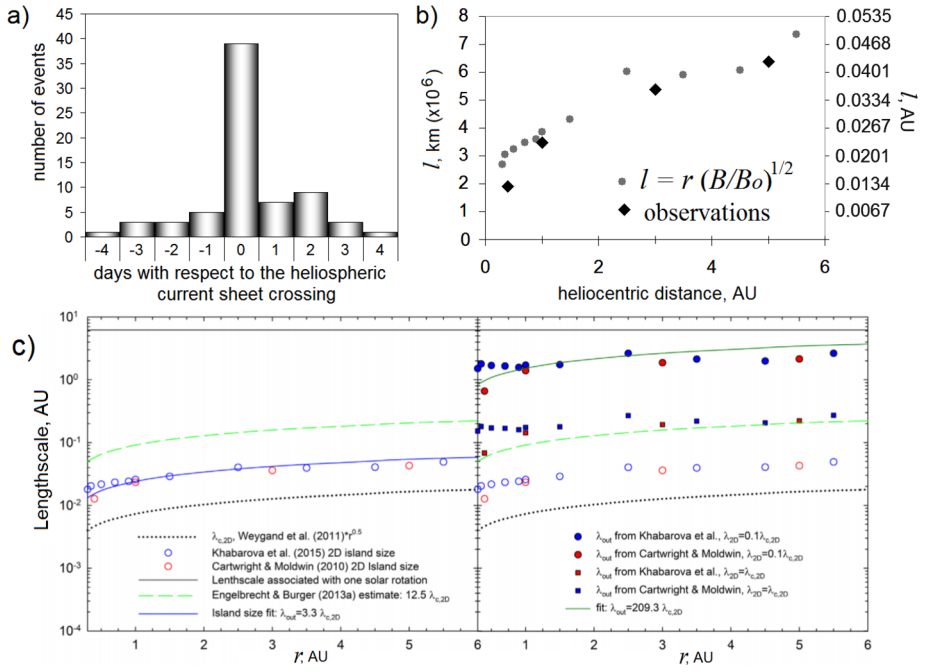

Fig. 28 Radial dependence of spatial characteristics of small-scale magnetic islands observed within ±4 day interval encompassing the HCS, and the related lengthscale determining perpendicular diffusion coefficients of charged particles in the heliosphere. **a**) Observational rate of magnetic islands near the HCS (the HCS crossing day is zero day). Modified from Cartwright and Moldwin (2010). **b**) Typical width of magnetic islands at different heliocentric distances as derived from observations shown by diamonds (Cartwright and Moldwin 2010) and predictions indicated by circles (Khabarova et al. 2015). In the corresponding empirical formula, l is the width of magnetic islands, r is the heliocentric distance, B is the IMF strength at the corresponding distance, and $B_0 = 10$ μT. **c**) magnetic-island-size-determined lengthscale at which the energy containing range breaks and the inertial range commences. Left panel: outer scales as calculated in different studies prior Engelbrecht (2019). Right panel: Estimations by Engelbrecht (2019) showing a wider range of possibilities, which correspond to various situations involving magnetic islands in the heliosphere

Greco et al. 2016 and Part II). Therefore, Fig. 28b allows for calculating the lengthscale λ_{out} corresponding to the wavenumber at which the energy-containing range of the 2D turbulence power spectrum commences. The latter determines the perpendicular diffusion coefficient, which is the key parameter responsible for the propagation of galactic cosmic rays perpendicular to the magnetic field. The cross-line propagation is thought to be the dominant transport mechanism beyond the Earth since the IMF lines are twisted so much there that they become practically perpendicular to the radial direction to the Sun. Figure 28c illustrates how estimations of λ_{out} can be improved by employing the magnetic island size (see details in Engelbrecht 2019 and Part II of this review).

Summarizing, the term magnetic islands is used when observations or modeling do not allow considering studied structures as 3-D objects. Talking of 2-D magnetic islands, one cannot say whether they represent plasmoids/blobs or flux ropes/magnetic tubes. Additional studies are required to understand their nature. In the solar wind, tracking magnetic islands with several spacecraft is a method that allows distinguishing between closed IMF structures and flux ropes. Methods of identification of flux ropes can be used as methods identifying magnetic islands. Although plasmoids and flux ropes are phenomenologically different ob-

jects, theoretical studies supported by observations show that physical effects associated with the structures are the same. An important consequence of the existence of dynamical magnetic islands in the heliosphere is local particle acceleration.

3 Particle Acceleration Associated with Dynamical Current Sheets, Flux Ropes and Plasmoids in the Solar Wind

3.1 Evolution of Views on Particle Acceleration in the Solar Wind. The Role of Magnetic Cavities in Local Particle Acceleration

The fact that magnetic reconnection can accelerate charged particles is undoubted. This effect has been known for decades for current sheets of various types, including those separating magnetic islands, and for magnetic islands themselves. It has been studied theoretically in many aspects and details, from estimations of the reachable energies to particle tracing via numerical simulations (e.g., Matthaeus et al. 1984; Büchner and Kuska 1998; Zharkova and Gordovskyy 2004, 2005; Drake et al. 2006, 2010; Siversky and Zharkova 2009; Fleishman et al. 2011; Zelenyi et al. 2011; Bian and Kontar 2013; Edmondson and Lynch 2017; Muñoz and Büchner 2018; Du et al. 2018; Xia and Zharkova 2018; Comisso and Sironi 2019; Zhou et al. 2019).

Meanwhile, observations of local particle acceleration in space were limited to studies of planetary (mainly terrestrial) magnetotails and the solar corona (see, for example, Somov and Kosugi 1997; Zelenyi et al. 2011; Vasko et al. 2012; Zhou et al. 2015 and references therein). In view of this, the HCS and similarly strong current sheets in the heliosphere might be the main object of interest for specialists in heliospheric physics. However, until 2015, only one paper claimed the association of enhancements in energetic particles up to several MeV with the HCS crossings observed in the outer heliosphere (Richardson et al. 2006), and there were no such reports regarding the HCS and energetic particles in the inner heliosphere. The first clear evidence for pronounced particle acceleration up to 1–2 MeV/nuc associated with isolated HCS/HPS crossings at 1 AU was presented in 2015 in works by Khabarova et al. (2015) and Zharkova and Khabarova (2015), and similar crossings were reported later by Khabarova et al. (2016, 2017b, 2018a) and Adhikari et al. (2019).

Prior attempts to find signatures of particle acceleration near current sheets in the solar wind, including the HCS, were unsuccessful partially because the effectiveness of magnetic reconnection was supposed to be insufficient to accelerate particles to suprathermal energies. Current sheets in the solar wind were treated as planar thin 2-D objects. Magnetic reconnection was thought to be Petsheck-type suggesting a single act of reconnection that finally tears a whole current sheet up completely as shown in Fig. 9. The key observational work about this problem claimed the "*Absence of energetic particle effects associated with magnetic reconnection exhausts in the solar wind*" (Gosling et al. 2005a). It was thought at that time that all reconnecting current sheets should produce narrow reconnection exhausts, and, therefore, finding signatures of magnetic reconnection in the solar wind meant finding Petschek reconnection only. The logic was, subsequently, as follows: if one observes clear signatures of outflows with the increased temperature and speed in the solar wind, but there is no sharp energetic particle enhancement in the nearest vicinity of the exhaust, then the reconnecting current sheet does not accelerate particles.

Figure 29 illustrates how different pre-set of ideas may lead to completely different conclusions. Khabarova and Zank (2017) have shown a significant energetic particle flux enhancement up to 5 MeV/nuc observed during the very event studied by Gosling et al. (2005a)

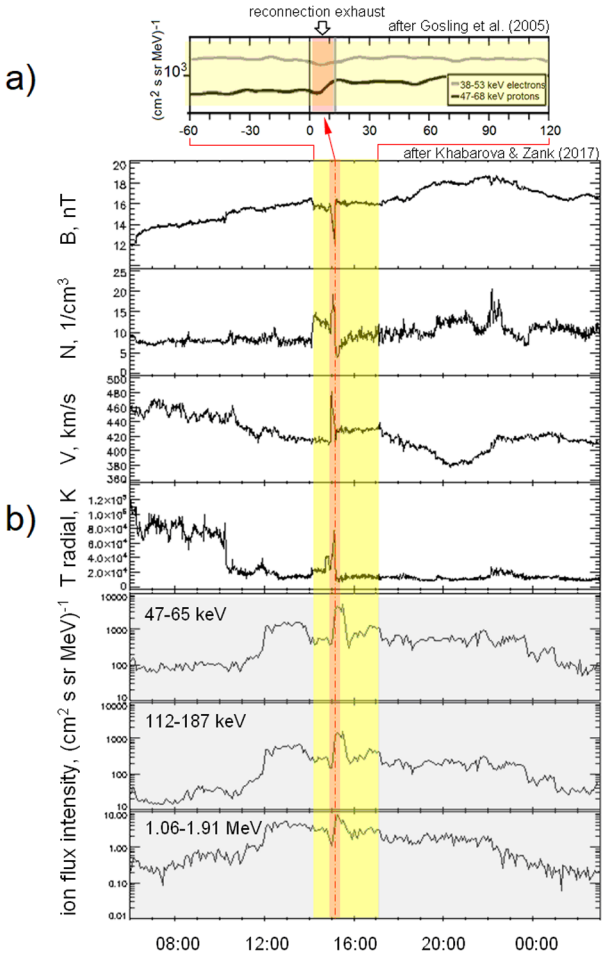

Fig. 29 The same event analyzed under different approaches that lead to different conclusions about the ability of magnetic reconnection to accelerate particles in the solar wind. **a**) Suprathermal ion flux intensity in the 47–68 keV energy channel according to Gosling et al. (2005a). **b**) Extract from the study of the same event by Khabarova and Zank (2017), showing the period from 06:00, 3 October 2000 to 04:00, 4 October 2000. From top to bottom: the solar wind density N, speed V, and temperature T (uncolored panels), and the light-blue colored panels indicate the energetic ion flux from different randomly chosen energy channels from the same ACE EPAM telescope as considered by Gosling et al. (2005a). The pink area indicates the reconnection exhaust seen in plasma parameters, the red vertical line shows the position of the reconnecting current sheet, and the yellow stripe shows the period under consideration in the study by Gosling et al. (2005a)

and explained that the conclusion about the absence of particle acceleration was based on the incorrect expectation of observing a narrow exhaust of accelerated particles in the nearest vicinity of a reconnecting current sheet (see Fig. 29). Figure 29a is an extract from the key figure of Gosling et al. (2005a) characterizing a course of the suprathermal ion flux intensity in the 47–68 keV energy channel, on the base of which the conclusion about the absence of particle acceleration was made. The pink area indicates the period during which the reconnection exhaust is observed as identified by Gosling et al. (2005a) via the enhanced density N, speed V, and temperature T shown in Fig. 29b. Gosling et al. (2005a) considered a $-1/+2$ day region encompassing the reconnecting current sheet. The resolution is unknown but lower that the 5-minute resolution considered by Khabarova and Zank (2017) (compare the pink area in Fig. 29a and the same in bottom light-blue panels of Fig. 29b).

Khabarova and Zank (2017) analyzed a several-day period encompassing the event and claimed that the region filled with accelerated energetic particles happened to be ten times wider, similar to observations in the solar atmosphere (Fleishman et al. 2020). An analysis of the ion flux intensity variations (Fig. 29b) showed that energies reached by particles were several times higher than expected by Gosling et al. (2005a) under a supposition of magnetic

reconnection occurring in a simple Petsheck way at a single thin current sheet. According to the occurrence of a small peak in the background of a larger peak seen in the energetic ion flux profiles in the bottom panels of Fig. 29b, there were signatures of both local particle energization associated with the reconnection exhaust identified by Gosling et al. (2005a) and particle acceleration determined by collective/stochastic effects in surrounding magnetic islands and current sheets discussed by Zank et al. (2014, 2015).

Therefore, the study by Gosling et al. (2005a) was restricted by an analysis of the particle behavior in the lowest energy channels of several tens of keV seen under an insufficient resolution. In such circumstances, the time period, the data average, and energy ranges chosen by Gosling et al. (2005a) did not allow for recognizing the effect. Their methodology revealed a plateau (Fig. 29a), but did not allow finding out that it was a plateau on top of the strong enhancement seen with a higher resolution during a longer period (see Fig. 29b). The particular event was associated with relatively large magnetic islands formed inside a fragmented ICME. The energetic particle flux peak occurred at the strongest current sheet separating magnetic islands from the ICME sheath. Khabarova and Zank (2017) demonstrated that energetic particles were accelerated locally, providing evidence that the energetic particle flux enhancements were detected by ACE and WIND with a time shift corresponding to the propagation of the whole structure from one spacecraft to the other, and showed the occurrence of magnetic islands associated with the event.

Khabarova and Zank (2017) also expanded the study and performed a statistical analysis of the energetic ion flux intensity level for the several-day interval around reconnecting current sheets of various origins, analyzing more that 100 reconnection exhausts identified by J. Gosling. It was found that, purely statistically, peaks of energetic ion flux enhancements up to 5 MeV are observed near reconnecting current sheets. The latter is in agreement with a statistically-supported increasing level of the energetic ion flux found around all types of strong coherent structures (without any differentiation for shocks, current sheets and other discontinuities) reported by Tessein et al. (2013, 2015).

Examples of energetic particle flux enhancements associated neither with SEPs, nor with CIR/SIR energetic particles, but with the HCS crossing as observed by ACE and WIND spacecraft near the Earth are shown above in Figs. 7b and 27a. Here we show Fig. 30 that allows for comparisons between energetic ion enhancements observed by two spatially separated identical spacecraft STEREO A and STEREO B during the HCS/HPS crossing in November 2007. STEREO A observations were discussed first by Zharkova and Khabarova (2015), and the complete picture from STEREO A, STEREO B and ACE was presented in Khabarova et al. (2018a). Note that the same event, detected by ACE, is shown in Fig. 7b. The HPS crossings in Fig. 30 are characterized by sharp changes in the azimuthal IMF angle, the high plasma beta, and sharp drops in the IMF strength corresponding to crossings of strong current sheets within the region. Owing to the relative position of the spacecraft, which can be found at https://stereo-ssc.nascom.nasa.gov/cgi-bin/make_where_gif and the rotation of the solar wind in the anti-clockwise direction (when viewed from the solar North pole), STEREO B observes the crossing first, then the HPS reaches the 1st Lagrangian point in which ACE orbits, and, finally, STEREO A.

The two panels in Fig. 30 show the importance of an analysis of local disturbances near the HPS. STEREO B detects even more enhancements associated with ripples of the HCS than STEREO A and the ACE spacecraft. The crossing of the HCS ripples is seen as the fast changes of the azimuthal angle in the bottom panel.

The occurrence of a time shift in observations of energetic ion enhancements by differently-located spacecraft is a “calling card” of such events, called atypical energetic particle events (AEPEs) to distinguish them from solar energetic particle (SEP) events,

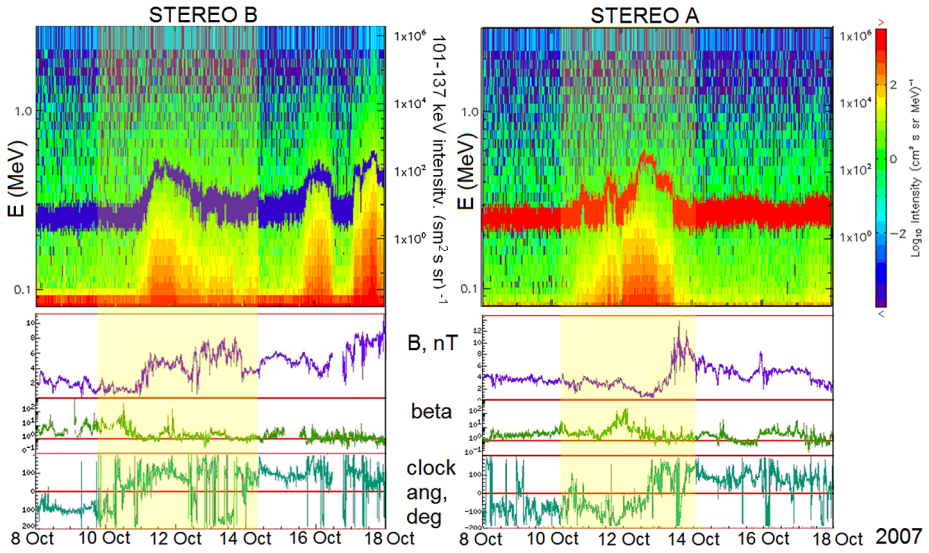

Fig. 30 Examples of observations of energetic particle flux enhancements associated with the HCS/HPS crossing as observed by two spacecraft separated by 36° (adapted from Khabarova et al. (2018a)). Left panel: STEREO B. Right panel: STEREO A. Same event as shown in Fig. 4b (ACE observations). From top to bottom: energetic ion flux spectrogram (omni-directional) combined with variations in the 101–137 keV energy channel; the IMF strength, the plasma beta and the IMF azimuthal angle. Magnetic-island–dominant region is indicated by the yellow stripe

CIR/SIR-associated energetic ion flux enhancements, and effects of diffusive shock acceleration (DSA) (see detailed explanations in Khabarova et al. 2016; Khabarova and Zank 2017; Adhikari et al. 2019; Malandraki et al. 2019; Pavlos et al. 2019).

Only DSA events and AEPEs can be considered as local phenomena occurring at the point of observations or nearby. In other cases, energetic particles come to 1 AU either from the Sun (SEP events) or from CIR/SIR shocks formed beyond the Earth's orbit, typically at 2–3 AU (Malandraki and Crosby 2018).

AEPEs are presumably produced by collective effects, namely by (i) stochastic magnetic reconnection at the HCS and current sheets separating magnetic islands, (ii) Fermi acceleration due to merging and contraction of SMIs, and (iii) resonance-like effects in dynamical magnetic islands (see the theoretical background in Zank et al. 2014, 2015; le Roux et al. 2015, 2016, 2018, 2019; Mingalev et al. 2019). As a result, AEPEs demonstrate weak anisotropy (Khabarova et al. 2015; Mingalev et al. 2019), much weaker than in the SEP or CIR/SIR cases since the source is around the spacecraft position and particles come to the detector practically "from everywhere".

Observations of AEPEs are not restricted to the HCS/HPS crossings. Any crossing of a strong reconnecting current sheet may be associated with energetic particle flux enhancements if the current sheet is disturbed and produces magnetic islands. The presence of magnetic islands (blobs/plasmoids) is crucial for increasing the effectiveness of magnetic reconnection and particle acceleration (Fleishman and Toptygin 2013). As mentioned above, magnetic islands also can be formed within the main body of an ICME, in the ICME sheath and SIRs/CIRs. An ICME can become fragmented on its way to the point of observations due to its interaction with a CH flow, another ICME or simply because of twisting and magnetic reconnection at borders of a large flux rope, which occurs with time and produces several

smaller-scale magnetic islands separated by current sheets instead of the one large flux rope in the main ICME body (Khabarova et al. 2016, 2017b, 2018a; Khabarova and Zank 2017; Adhikari et al. 2019; Malandraki et al. 2019; Oka et al. 2021). ICME-born magnetic islands are the largest among those formed directly in the solar wind, and, consequently, associated acceleration of charged energetic particles is strongest there (Khabarova and Zank 2017; Adhikari et al. 2019; Malandraki et al. 2019; Oka et al. 2021).

Furthermore, since ICMEs are preceded by ICME-driven shocks, energetic particles energized via DSA can be trapped by magnetic islands downstream of the shock, including the ICME sheath turbulent cavity (Oka et al. 2021) and the main ICME body (Khabarova and Zank 2017; Adhikari et al. 2019). As a result, seed particles can be re-accelerated to 5 MeV or even higher energies instead of 1–2 MeV typically observed in the pure case of a wide open region of magnetic islands. An explanation of this effect was given in Zank et al. (2015) through the example of the heliospheric termination shock crossing. Voyager 2 observations showed AEPEs located far downstream of the termination shock, where the DSA effect should diminish. Zank et al. (2015) showed that a combination of DSA and a mechanism of particle acceleration in dynamical magnetic islands proposed by Zank et al. (2014) successfully explains most of the properties of the energetic particle enhancement.

The same combined mechanism is applicable to interplanetary shocks of any origin, downstream current sheets and magnetic islands (Khabarova et al. 2016, 2017b; Khabarova and Zank 2017; Malandraki et al. 2019). A possibility of combined acceleration in regions filled with magnetic islands is very important, since it allows for particles obtaining higher energies than from acceleration of thermal energy plasma in reconnecting current sheets and magnetic islands.

Purely theoretically, there is no difference in what way the injection of pre-accelerated particles to the region of subsequent acceleration occurs. For mechanisms of particle acceleration at current sheets and magnetic islands in the solar wind, there is no "seed population problem" which is an issue for interplanetary shocks (e.g., Verkhoglyadova et al. 2015). Pre-accelerated (seed) particles may be produced by DSA, magnetic reconnection at nearby current sheets or can even be SEPs. Generally, one may assume that, besides the properties of the solar wind surrounding the region, the highest reachable energy of re-accelerated particles depends on (i) the initial energy of charged particles (pre-accelerated or not), (ii) the size of magnetic islands, (iii) their corresponding gyroradii, (iv) the number of magnetic islands, and (v) the size of the magnetic cavity in which magnetic islands are confined. The analytical dependence based on (i–iii) is obtained for the case of acceleration due to resonance pumping (Mingalev et al. 2019) and the importance of (ii) and (iii) is known since theoretical studies by Zank et al. (2014), and further work on deriving a semi-empirical formula for the general case of magnetic reconnection and Fermi acceleration in magnetic islands is currently ongoing.

Therefore, the studies of the last decade have brought understanding that reconnecting current sheets produce magnetic islands, and the latter can trap and additionally accelerate energetic particles. Meanwhile, this is not the end of the chain of effective particle energization in space. There is one more aspect involving current sheets that should be taken into account. Comparisons of STEL reconstructions of the solar wind speed (see Fig. 4a and Sect. 3.1) and the IMF with in situ observations reveal that AEPEs are mostly associated with crossings of large-scale magnetic cavities formed by strong current sheets of various origins. The latter may represent leading edges of ICMEs or SIRs/CIRs. One of the walls forming a cavity is usually the HCS (see Fig. 31).

Taking in to account that such cavities evolve, and some parts of the cavity always experience compression despite the expansion of the solar wind as a whole, magnetic cavities

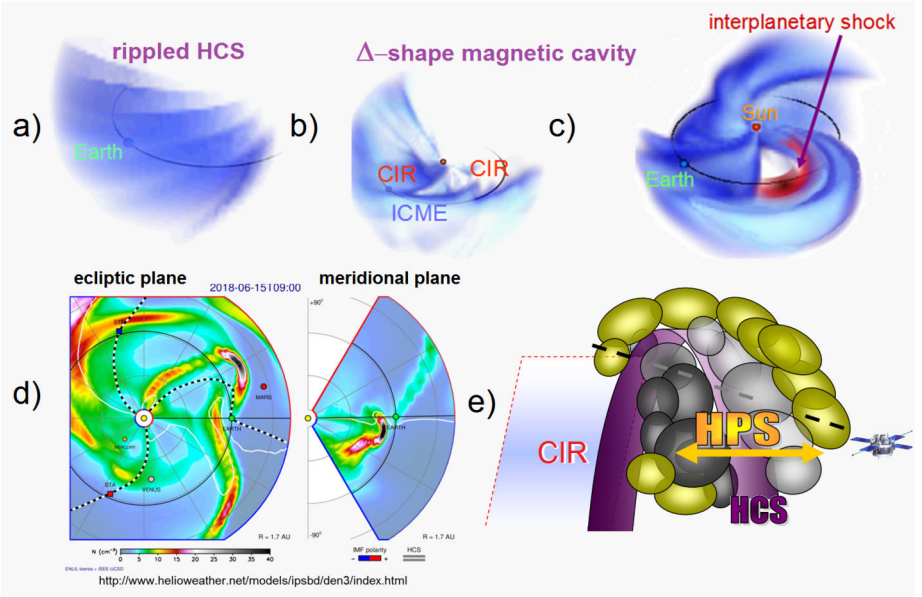

Fig. 31 Formation of magnetic cavities in the interplanetary space and the interaction of streams with the HCS. **a**) Cavities inside the HCS ripples. **b**) Cavities formed by co-existing streams/flows. **c**) HCS distorted by an approaching ICME. **d**) ENLIL reconstructions of the HCS (white line) distortion by propagating streams (green and yellow areas). Left – the ecliptic plane. Right – the meridional plane. In the meridional plane it is seen that the HCS is crossed twice – before and after the stream passage. Magnetic cavities are formed between the stream and the HCS. **e**) Sketch illustrating a complex distortion of the HCS/HPS-magnetic island system by an approaching CIR. Magnetic islands within the HPS are grey and outside are yellow, but since the HCS/HPS is strongly bended by the CIR, some of "outside" magnetic islands are located inside the ripple (modified from Adhikari et al. 2019)

may play a role of natural tokamaks/spheromaks/stellarators (depending on their origins and configurations), allowing all possible types of particle acceleration to occur and even be intensified within closed magnetic walls (see Khabarova et al. 2015). An analogy between magnetic cavities and the magnetic fusion devices appears since magnetic cavities ensure the magnetic confinement of a region where acceleration takes place, and magnetic islands play a significant role in the local energy release. One can notice that a detached ICME magnetic cloud resembles a modern stellarator with an island-chain-type divertor, a fragmented ICME may be associated with a chain of torus-shape tokamaks or a spheromaks, while magnetic cavities formed by several streams/flows from one side and the HCS from the other side resemble simple magnetic mirror traps filled with magnetic islands (see Waelbroeck 2009; Feng et al. 2011; Helander et al. 2012 and references therein).

Figure 31 illustrates the main types of magnetic cavities formed in the interplanetary space. Figure 31a shows the HCS/HPS system that possesses a lot of small-scale ripples with a width of ~ 0.01 AU. Magnetic islands in such a system may be produced locally by magnetic reconnection at current sheets within the HPS as well as drift from the upstream sources (Maiewski et al. 2020). Since a ripple represents a semi-closed magnetic structure, magnetic islands become confined inside the ripple, and the plasma/magnetic field configuration allows effective particle acceleration if the HCS experiences distorsion, compression or oscillations (Mingalev et al. 2019).

Figure 31b considers a complex case of a multi-stream interaction, which often occurs in the solar wind in solar maximum, when active regions coexist with low-latitude CHs at the Sun. Figure 31c illustrates the HCS distortion by an approaching ICME with the ICME-driven shock ahead. If an ICME is disconnected from the Sun, which inevitably occurs at some heliocentric distance, it represents a magnetic cavity too, since the main part of an ICME is shielded from the surrounding solar wind by strong current sheets at the ICME sheath edge. Generally, an expanding ICME/magnetic cavity cannot accelerate particles inside it. However, processes of magnetic reconnection and particle reacceleration at current sheets and in dynamical magnetic islands representing a fragmented flux rope provide such an opportunity (Oka et al. 2021), especially taking into account that ICMEs propagate through the turbulent solar wind (Manchester and Van Der Holst 2017) and very often are affected by long-lived CIRs (Malandraki et al. 2019).

Figure 31d shows a quite typical situation of co-existence and interaction of different streams and flows in the solar wind, as ENLIL reconstructions reveal (see http://www.helioweather.net/ for details, and explanations of the key points about the 3-D modeling can be found in Odstrcil 2003). The HCS is shown by the white line. From ENLIL and STEL reconstructions it is known that the HCS is very "elastic". In a course of the stream/flow – HCS interaction, the HCS may be bent by a stream/flow or may cover a large part of the stream, returning back to the undisturbed state in several hours after its passage. In 3-D, an ICME/CIR interacting with the HCS resembles a pet crawling under the carpet. Taking this into account, one may expect to cross the HCS both before and after the passage of high-speed streams/flows when observing the solar wind with a single spacecraft (see the meridional cut in the right panel of Fig. 31d). Correspondingly, a magnetic cavity filled with magnetic islands is formed between the HCS and the strongest current sheet at the leading edge of the stream (see Khabarova et al. 2016, 2017b).

Sometimes, a part of the HCS can coincide with the stream/flow leading edge as shown in the sketch modified from Adhikari et al. (2019) (see Fig. 31e). Generally, this type of magnetic cavity corresponds to the HCS ripple formed in the perpendicular direction to the ecliptic plane in front of an approaching stream/flow (see a hump formed by the HCS in the southern heliosphere below the Earth position in the right panel of Fig. 31d). The HCS is surrounded by magnetic islands and current sheets filling the HPS (the magnetic islands inside the HPS are shown by grey), and some magnetic islands are located outside the HPS (shown by yellow). When the HCS/HPS system is strongly bent, the ripple contains both types of islands (see Fig. 31e). Multiple crossings of current sheets separating local changes of the magnetic field polarity and even several crossings of the larger-scale IMF "sectors" are possible in this case. Note, that such a situation can occur during the interaction of any high-speed stream (both an ICME and a SIR/CIR) with the HCS, but of course there is a corresponding difference in topologies of formed magnetic cavities and the HCS/HPS bending.

Adhikari et al. (2019) employed the sketch shown in Fig. 31e to interpret the event of several HCS crossings before the CIR approach as well as related energetic particle flux enhancements on 24–25 December 1998. This event was studied by Gosling et al. (2006) for the 24-hour period starting from 00:00 UT, 25 December 1998 (Fig. 6a of this review), and Adhikari et al. (2019) considered a full course of the events that took two days (24–25 December 1998). Gosling et al. (2006) discussed only one HCS crossing, coinciding with the leading edge of the CIR, and limited their study to the situation inside the HCS ripple. The whole event was far more complex and included the HCS crossing at the outer side of the ripple that occurred several hours before (see Fig. 4 of Adhikari et al. 2019). Imagine that the CIR moves toward the spacecraft (or the Earth), bending the HCS in front of it as

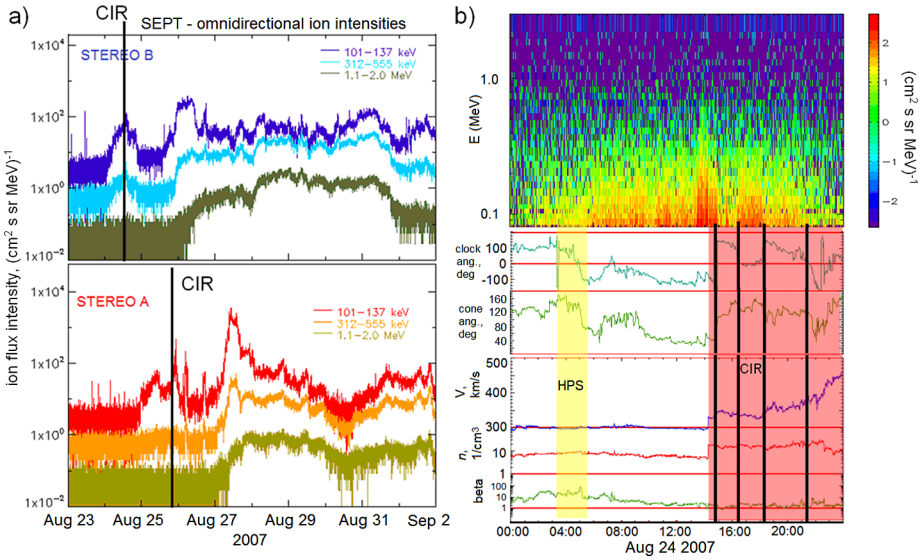

Fig. 32 Example of energetic particle flux enhancements caused by particle acceleration in the magnetic cavity formed by the HCS and the approaching CIR. **a**) Energetic ion flux intensity in three energy channels observed by STEREO B (upper panel) and STEREO A (bottom panel). Prominent energetic ion flux enhancement is observed bu both spacecraft with corresponding time delay before typical energetic ion enhancements associated with SIRs/CIRs. **b**) Detailed information on the magnetic cavity crossing as observed by STEREO B. From top to bottom: energetic ion flux intensity spectrogram showing ions accelerated up to 1 MeV/nuc, IMF direction angles, the solar wind speed and density, and the plasma beta. The HPS is shown by the yellow stripe, and the CIR is shown by the pink stripe. Main current sheets within the CIR are indicated by vertical black lines (modified from Khabarova et al. 2016)

shown in Fig. 31d and 31e, then the HCS can be crossed twice (see the spacecraft path in Fig. 31e). Since the HCS/HPS fold or ripple moves forward, the IMF polarity may change near the CIR leading front several times just in several hours, depending on the way in which the spacecraft crosses the whole structure, which is atypical for the pure undisturbed HCS crossing case.

An example of observations of energetic particle flux acceleration occurring in magnetic cavities is shown in Fig. 32. This is the case of the magnetic cavity formed by the HCS and an approaching CH flow with a strong CIR/SIR at the leading edge. Energetic ion enhancements in hundred keV–1 MeV energy channels are detected by the twin STEREO spacecraft after the HCS crossing, but before the enhancement typical for SIR crossings. STEREO B observed it first, and then STEREO A detected accelerated particles with the corresponding delay (see Fig. 32a). The crossing is shown in detail in Fig. 32b.

Notably, the peak of the energetic ion flux enhancement is observed between the HPS and the CIR leading current sheet, and there are obvious local enhancements between the main current sheets observed within the CIR.

Using a theory by Zank et al. (2014), Adhikari et al. (2019) reconstructed key properties of magnetic island-associated enhancements, which can be considered to be a confirmation of the correct interpretation of the event. Adhikari et al. (2019) explained the event in the frame of the new paradigm, considering dynamical processes in magnetic islands confined in magnetic cavities as sources of energetic particles accelerated locally in the solar wind.

This approach was confirmed by the fact that the energetic ion flux was significantly enhanced in the region filled with magnetic islands, too far from the CIR to be explained by the impact of the CIR, and then the classic CIR-associated energetic ion flux enhancement was observed too. Gosling et al. (2006) reported the occurrence of closed IMF field lines near the HCS, but this was interpreted in the way shown in Fig. 9a.

In most cases, it is not easy to distinguish between local particle acceleration/re-acceleration of seed particles and that determined by distant sources, observing accelerated particles in situ. The key features of local ion acceleration in the solar wind are the following: a) pronounced energetic ion flux enhancements seen in the 100–600 keV energy channels, b) the almost-independent behavior of time-intensity profiles observed in lower-energy channels from those seen in higher-energy channels, c) such enhancements are observed by two spacecraft with a time delay corresponding to the core solar wind propagation, and d) ion time-arrival spectrograms (so-called 1/ion speed dispersion plots) for heavy ions often show a vertical pattern indicating local particle acceleration (Khabarova and Zank 2017).

In most cases, different mechanisms of particle acceleration act simultaneously (see Sect. 3.2), but sometimes pure cases are observed. Figure 33 is an example of consequent operation of two local mechanisms of particle energization, namely, DSA and that associated with current sheets and magnetic islands. The ICME-driven interplanetary shock, shown by the blue vertical line in Fig. 33a, accelerated ions up to 1 MeV while particle acceleration occurring within the fragmented ICME was more effective and accelerated particles to ~ 5 MeV. The strongest reconnecting current sheet at the internal boundary of the ICME sheath is shown by the red line. Since both events are spatially separated (which means that they are temporally separated for an observer), one can also see the region in which they overlap. Figure 33b shows the fine structure of the ICME with identified current sheets. The occurrence of bi-directional strahls characterizing the movement of accelerated electrons along closed magnetic field lines is obvious from the PAD (see the upper color panel). It is important to note that the presence of bi-directional strahls just means that there is electron acceleration at current sheets associated with closed or semi-closed magnetic structures such as plasmoids. Connection to the Sun is not necessary (see Sect. 3.3 for explanations).

Summarizing, it is worth underlining the co-existence of many mechanisms of particle acceleration in the solar wind, producing the observed picture of energetic particle enhancements. The most important roles in the acceleration of charged particles by the electric field are played by (i) the Fermi mechanism (caused by merging/coalescence and/or contraction/squashing of magnetic islands), and (ii) magnetic reconnection (Zank et al. 2014, 2015; le Roux et al. 2015, 2016, 2018, 2019; Xia and Zharkova 2018, 2020; Mingalev et al. 2019; Zhou et al. 2019; Khabarova et al. 2020; Oka et al. 2021). All the studies reported here also acknowledge the importance of the guide magnetic field in increasing the effectiveness of particle acceleration. Numerical simulations show that an approach to the real ion/electron mass ratio and larger scales typical for the solar wind gives more opportunities for particle acceleration, especially in the 3-D case (e.g., Muñoz and Büchner 2018; Xia and Zharkova 2018, 2020; Werner et al. 2018; Zhu et al. 2019).

Historically, all energetic particles observed at 1 AU were thought to be produced somewhere far from the point of observations. Ignoring the existence of local particle acceleration led to difficulties in interpretation of observations. Meanwhile, many complex events can be understood by knowing that dynamical processes in the HCS/HPS system, current sheets of other origins and magnetic islands can lead to initial acceleration of the solar wind charged ions to 100 keV–1 MeV energies and re-acceleration of energetic particles to at least 5 MeV directly in the solar wind. The effectiveness of these processes increases if the region filled with magnetic islands is bounded by magnetic cavities, serving as magnetic confinement and allowing energization to realize in a finite region (e.g., Ergun et al. 2020).

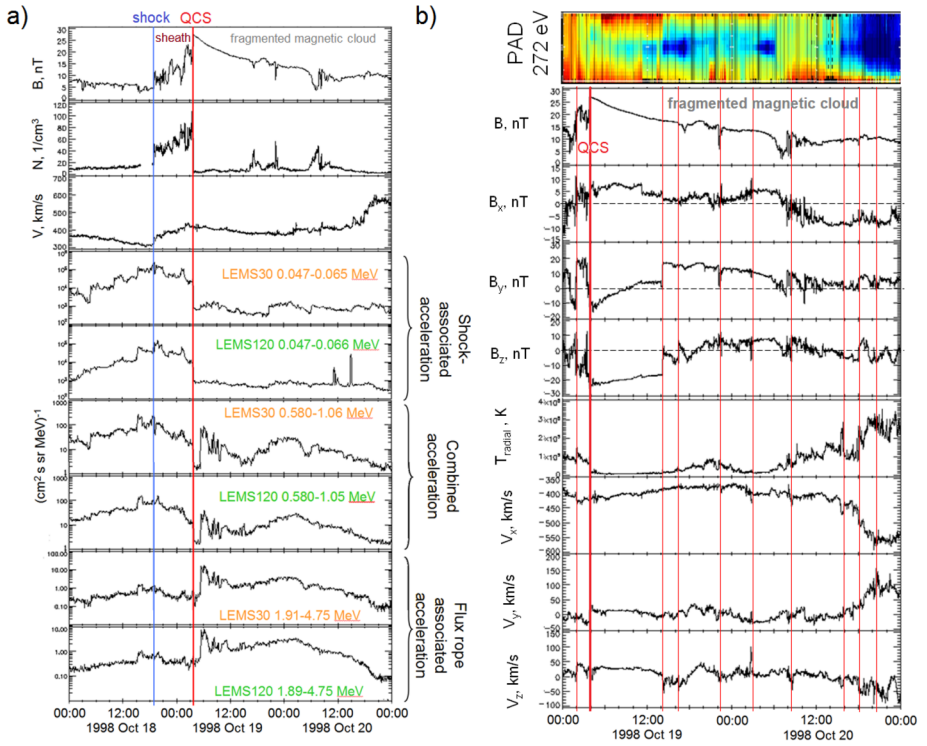

Fig. 33 Energetic ion flux enhancements caused by different mechanisms associated with the arrival of an ICME. **a**) From top to bottom: IMF strength, plasma parameters (density and speed) from ACE (the 1 AU spacecraft), ion flux from ACE LEMS30 and LEMS120 (see corresponding energy channels indicated). The first (left) ion flux enhancement is clearly associated with the interplanetary shock (blue line) and bounded by the end of the ICME sheath region represented by a QCS (red line) as seen in lower energy channels. The role of DSA decreases with increasing energy, but, beginning with ~ 0.6 MeV, local particle acceleration is seen in the fragmented magnetic cloud region filled with flux ropes/plasmoids/magnetic islands and strong current sheets. Adapted from Khabarova and Zank (2017). **b**) Detailed features of the fragmented magnetic cloud region, associated with current sheets and magnetic islands. From top to bottom: pitch-angle distribution spectrogram of 272 eV suprathermal electrons, the IMF strength and components, radial temperature, and speed components. The strongest current sheets with signatures of magnetic reconnection are indicated by red vertical lines. Adapted from Adhikari et al. (2019)

Therefore, the results of studies discussed in this section allow one to answer *question 2* (Q2) of Sect. 2.1: Energetic particle flux enhancements are often observed near the HCS/HPS because this is the region where local particle acceleration occurs simultaneously. The intensity of the particular event depends on the topology of the region, parameters of the surrounding solar wind plasma and IMF, parameters of magnetic islands and current sheets in the region, the occurrence of magnetic cavities ensuring confinement of the region of particle acceleration, and the pre-history of the event in terms of the existence of pre-accelerated energetic particles.

3.2 Combined Particle Acceleration in the Solar Wind

At 1 AU, observations often show signatures of two or more mechanisms of particle acceleration acting simultaneously. The same was found for the outer heliosphere. Does it work

in the middle, between the Earth and the far edges of the heliosphere? The example below allows us to answer this question positively.

Malandraki et al. (2007) presented and discussed energetic particle observations in the 3.8–19 MeV energy range, as measured by the COSPIN/LET instrument onboard Ulysses following the intense solar activity in 2005 January. They found that Ulysses observed ICME transient material on days 29–39, 2005 due to Ulysses being in a favorable position to detect, during this period, a system of solar wind transient flows that resulted from the interaction and coalescence of a series of unusually fast halo CMEs ejected from the Sun during 2005 January 15–20, in association with AR 10720, culminating with the one of the fastest halo CMEs that was ejected on January 20. During this period, in the declining phase of the solar cycle 23, CIR/SIRs were predominantly observed in the heliosphere leading to the formation of a compound stream at ~ 5 AU observed by Ulysses. Multiple shocks are often seen in association with the passage of such ICME/SIR combinations at such heliocentric distances (e.g. Malandraki et al. 2008). In January 2005, three forward shocks and a later reverse shock were observed in association with the ICME/SIR interaction. As was shown by Malandraki et al. (2007), energetic particles injected from the Sun during the 2005 January intense solar activity were not observed at COSPIN/LET energies by Ulysses until a stream interface (SI) associated with a preceding CIR that acted as a barrier to the particles reached the spacecraft. It was concluded that, at least at the energies measured by LET, the energetic particle profiles observed by Ulysses at 5 AU during this interval do not show evidence for direct propagation from the Sun to the observer but appear to be controlled by large-scale solar wind structures crossing the spacecraft.

Malandraki et al. (2019) revisited the January 2005 event from a lower-energy ion perspective, carrying out a detailed analysis of the hourly ion flux from the LEMS120 telescope of the HI-SCALE instrument onboard Ulysses (Lanzerotti et al. 1992) as well as the high-resolution IMF/plasma data, presented in Fig. 34a from 2005, 22–31 January. The different shading throughout the data denotes the different regions preceding and following the ICME merged structure, as identified by Malandraki et al. (2019) based on the behavior of the solar wind and magnetic field parameters. Region 1 (R1) is the interval between the Stream Interface (SI) and the Reverse Shock (RS), Region 2 (R2) is a quiet interval between the CIR and the ICME compound structure, from the RS to the first of the three Forward Shocks (FSs), Region 3 (R3) corresponds to the merged ICME sheath whereas Region 4 (R4) denotes the period when Ulysses is immersed in the ICME main body (see numbers above the upper panel in Fig. 34a). The analysis revealed the existence of two main peaks of the energetic ion flux in energies up to 1 MeV observed during the period of interest: the smaller double peak associated with the CIR R1, and the higher double peak observed within R3.

Lower-energy ions behave almost independently of higher-energy particles, as seen from the comparison of the black and green curves. An abrupt enhancement of the lower energy (0.061–0.601 MeV) ion intensities is observed at the passage of the SI over the spacecraft. At the passage of the RS, a more gradual decrease is observed in the lower-energy ion flux profiles, with the intensity levels getting back to nearly pre-event levels and exhibiting a plateau thereafter within R2. Energetic ions of higher-energy intensities (from 0.601–4.752 MeV), as observed in R1 and R2, have typical SEP characteristic profiles in a similar way to that shown in Malandraki et al. (2007). Lower-energy ion flux enhancements observed in R1 are definitely not related to the SEP propagation. They are CIR-associated with a possible impact of DSA at the RS, but at the same time, they are quite possibly determined by the existence of magnetic islands inside R1, since typical DSA-associated profiles always peak at the shock position.

Furthermore, Malandraki et al. (2019) concluded that the extra peaks far downstream of the FS i.e. peak II is not related to DSA only but there is another origin for these energetic

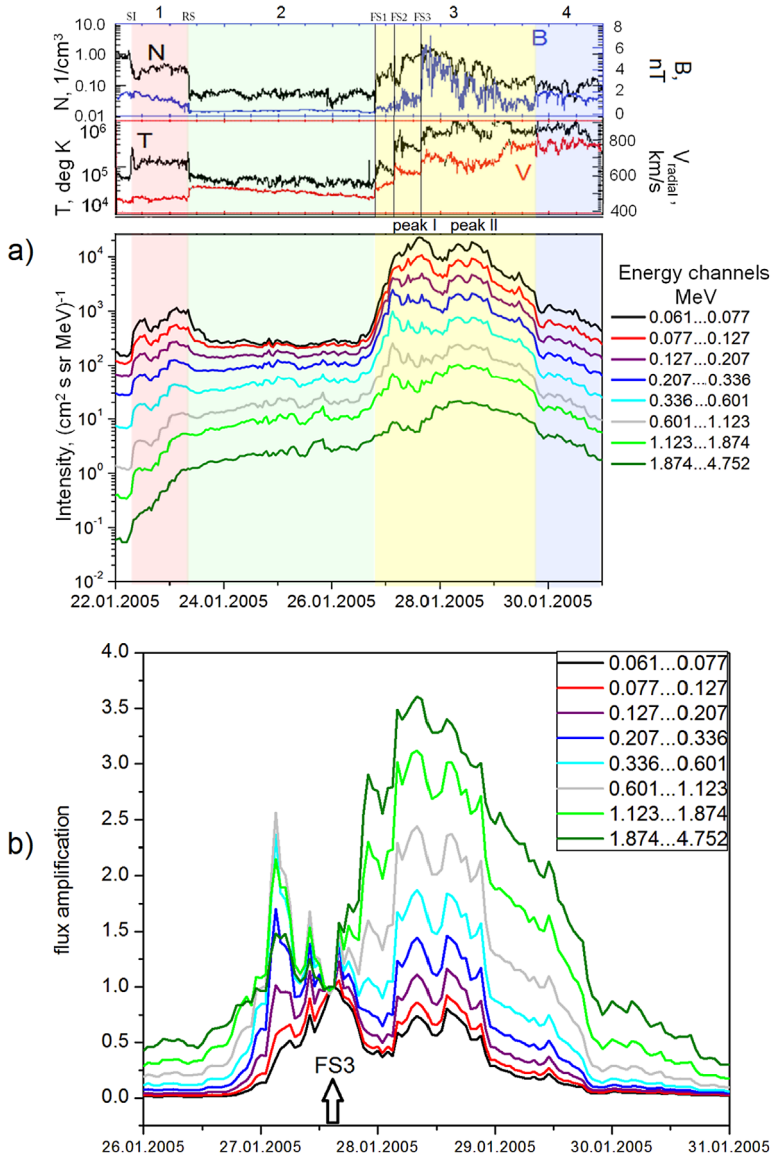

Fig. 34 Example of co-action of different mechanisms of particle acceleration in the solar wind. **a**) Variations in the solar wind plasma and IMF parameters and impact of local plasma/IMF configurations on the energetic ion flux profiles. Identified Regions 1–4, based on the behavior of the solar wind and magnetic field parameters are denoted by the different shading. From top to bottom: the solar wind density (black) and the IMF strength (blue), the solar wind temperature (black) and the solar wind speed (red) and the HI-SCALE/LEMS120 detector measurements of energetic ion flux in corresponding energy channels. Forward shocks of the merged ICMEs are shown by vertical lines FS1–FS3. **b**) Amplification factor calculated with respect to the position of FS3

particle enhancements. Figure 34b presents the flux amplification calculated for the eight energy channels of the HI-SCALE/LEMS120 telescope. The zero-point that is shown by the arrow corresponds to the last shock (FS3) position. In the case of pure DSA, the flux amplification factor should be unity downstream of the shock (see explanations in Zank et al. 2015). The existence of a prominent peak far behind the shock is a signature of some unaccounted-for processes that accelerate particles occurring within the ICME sheath. Furthermore, the order of the curves with higher energies on the top is a signature of the particle acceleration mechanism proposed by Zank et al. (2014) that suggests energization of ions by dynamical magnetic islands.

Inspection by Malandraki et al. (2019) showed a clear evidence for the existence of small-scale magnetic islands (SMIs) in R1 and R3. In both regions there is a clear anti-correlation observed between the density and the IMF strength, with the anti-correlated pulses being especially well-pronounced in R3, which is one of the signatures for the occurrence of SMIs. Furthermore, an analysis of IMF hodograms for each interval (not shown) suggests that the corresponding AEPEs cannot be explained by wave activity or large-scale turbulence. It is also proved that the variations of the IMF observed in R1 and R3 are not associated with Alfvénic fluctuations.

The other signature of the presence of SMIs is observations of the CSs separating them. The statistics of PVI events and CSs within the four intervals show that the number of high PVI events is approximately the same for the intervals 1, 3 and 4 (see Malandraki et al. 2019). At the same time, the number of CSs per hour is much higher within intervals 1 and 3, possibly indicating the intensified formation of SMIs separated by thin CSs detected using Gang Li's method (Li 2008).

The relative PVI rate over the CS rate is smallest in interval 3 and largest in the interval 4, which means that the role of CSs, compared to other coherent structures, increases in the turbulent ICME sheath and is insignificant in the main body of the particular ICME structure. The Grad-Shafranov reconstruction of the spatial profile of the local magnetic field was carried out, and also showed evidence for the existence of SMIs in Regions 1 and 3 (see Fig. 27c). Considering all these results together, Malandraki et al. (2019) concluded that the local particle acceleration in R1 and R3 is governed not only by shocks but also by dynamical SMIs and stochastically reconnecting CSs.

Magnetic islands and current sheets are objects at which solar energetic particles or shock-accelerated particles scatter in the solar wind. These also represent sources of particle energization/re-acceleration and consequently contribute to variations of time-intensity profiles of the energetic ion flux even in the case when seed particles originate from the corona or are associated with DSA at interplanetary shocks.

3.3 Two Populations of Suprathermal Electrons in the Solar Wind. Signatures of Local Acceleration of Core Electrons to Suprathermal Energies

The behavior of suprathermal electrons with energies above 70 eV at 1 AU has been considered to be the best method to identify the IMF direction changes also called IMF sector boundaries (see Sect. 2). Figure 35, adapted from Štverák et al. (2009), illustrates the place of suprathermal electrons in the electron velocity distribution function. Halo electrons are isotropic or weakly anisotropic, and strahl electrons are narrow beams, always field-aligned, which correspondingly form the famous 0–180° stripes in PAD spectrograms (see Figs. 6 and 7). Both halo and strahl electrons observed in the solar wind are usually believed to originate from hot coronal sources (e.g., Crooker et al. 2004; Štverák et al. 2009; Graham et al. 2017; Chen et al. 2020a). The most important process that may impact electrons far from the

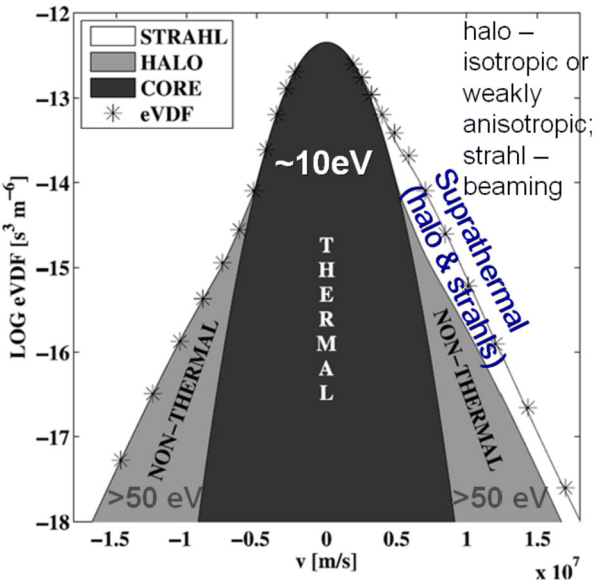

Fig. 35 Velocity distribution function of electrons observed at 1 AU (modified from Štverák et al. 2009). Core (thermal) fully isotropic electrons are shown by black. Halo electrons may be weakly anisotropic and following IMF lines. Strahl electrons are magnetic field aligned beams ($E > 70$–100 eV at 1 AU), moving predominantly away from the Sun. "Superhalo" are suprathermal electrons with energies > 2 keV

corona is supposed to be scattering (e.g., Fitzenreiter and Ogilvie 1992; Berčič et al. 2019). In particular, it is thought that halo electrons appear due to the scattering of beamed strahls, but the relationship between halo and strahl populations is debated (see Graham et al. 2017 and references therein).

If all suprathermal electrons come from the corona, the HCS crossings should be seen as simultaneous changes in the strahl electron PADs and the IMF direction identified via the IMF angles (e.g., Crooker et al. 2004). The corresponding PAD pattern should be very similar in all energy channels and represent a simple disappearance of one strahl-associated stripe and appearance of the other at the opposite (top/bottom) side of the PAD spectrogram, as shown in Fig. 6a. However, there are mismatches between observations of changes in the IMF vector angles and the suprathermal electron behavior obtained from PAD spectrograms (see Sect. 2). These may be a time lag between IMF and PAD changes characterized by periods of prolonged unstable direction of motion of suprathermal electrons (e.g. Fig. 6b), electron heat flux dopouts (e.g., Fig. 7, McComas et al. 1989, 1992), counterstreaming propagation of strahl electrons (e.g., Fig. 33b, McComas et al. 1994), and/or the non-uniform behavior of electrons of different energies.

It has been known for decades that heat flux dropouts occur within the HPS and in the nearest vicinity of current sheets. Before 2010th, only two mechanisms were thought to be responsible for the effect, namely, magnetic field line disconnection from the Sun as shown in Fig. 9a and/or intensive Coulomb scattering (e.g., McComas et al. 1989; Fitzenreiter and Ogilvie 1992; Crooker et al. 2003; Pagel et al. 2005). Modern studies suggest that there are more mechanisms, including local velocity shears, waves and turbulence (see Macneil et al. 2020 and references therein).

Bi-directional (or counterstreaming) strahls are often associated with ICMEs. An important question about the nature of this effect was raised by McComas et al. (1992, 1994). They gave an explanation that had become the most popular in the community of space scientists and is used nowadays. It is suggested that ICMEs remain connected to the Sun even far from it, so suprathermal electrons propagate along the expanding closed IMF structure back and forth to the ends of the ICME roots in the corona. McComas et al. (1992, 1994)

also note that there are cases when the occurrence of counterstreaming strahls in front of ICMEs indicates the U-shape of magnetic field lines opened to the outer heliosphere. However, the problem is that one can always find observations of bi-directional strahls (i) that are definitely not associated with ICMEs, and (ii) are associated with ICMEs undoubtedly disconnected from the Sun (Khabarova et al. 2015, 2016; Adhikari et al. 2019; Malandraki et al. 2019).

An idea of the loop entangling is sometimes employed to explanations of crossings of fragmented ICMEs in which counterstreaming strahls are observed (Baker et al. 2009). The same explanation is often given for the case of complicated HCS crossings (see Fig. 9b and related discussion).

Knowing that the HCS/HPS system is filled with and surrounded by dynamical magnetic islands and current sheets, one can interpret such a behavior of suprathermal electrons without making suppositions of entangled magnetic field lines, loops going far back to the Sun or lost-and-found connections to the coronal source of accelerated electrons. Electrons, similar to ions, can be accelerated to suprathermal energies via dynamical processes occurring both at current sheets and/or magnetic islands directly in the solar wind similar to their acceleration in the solar corona (e.g. Zharkova and Khabarova 2012, 2015; Khabarova et al. 2015; Dahlin et al. 2017; Khabarova and Zank 2017; Du et al. 2018; Xia and Zharkova 2018, 2020; Zharkova and Xia 2021). The latter explains the unusual PAD features associated with the HCS and other current sheets and gives an explanation to widely debated phenomena such as heat flux dropouts and bi-directional strahls, suggesting that those are determined by effects of local electron acceleration rather than scattering.

Indeed, recent numerical experiments and observations have shown that a spatial distribution of electrons accelerated by magnetic reconnection is far more complex that one can imagine from the Petschek reconnection topology shown in Fig. 9a. Narrow reconnection exhausts are an exception rather than a rule in real plasma conditions, especially talking of electrons weighing less than ions and being more maneuverable (Li and Lin 2012; Zharkova and Khabarova 2012, 2015; Egedal et al. 2015; Khabarova and Zank 2017; Du et al. 2018). If one considers a quite typical situation of a reconnecting current sheet with reconnection-borne magnetic islands, it is easy to find that electrons form wide clouds around the reconnecting sites.

Figure 36a and 36b present simulations of the behavior of electrons accelerated at the reconnecting current sheet with dynamically evolving magnetic islands. The three panels (from top to bottom) of Fig. 36a are examples of results of numerical modeling of the speed component parallel to the magnetic field, the logarithm of IMF strength and the electron density in the reconnecting region across the current sheet, respectively, as provided by Egedal et al. (2015). The intensity of the parameters is given with the color maps. Generally, maxima of all parameters follow the dynamical configuration of magnetic islands, but the speed panel shows the acceleration of electrons to the opposite sites of the two nearest reconnecting magnetic islands. The corresponding electron distribution function in the points numbered P3, P4 and P5 is shown in Fig. 36b. Egedal et al. (2015) stress that there are areas of mixing of electrons with different pitch angles and that those areas coincide with the localization of magnetic islands. Also, there is a region near the X-point (where a single current sheet separating magnetic islands is detected in observations) in which the distribution is fully isotropic, since the magnetic field is weak in the center of the exhaust (see the P5 panel and compare with the location of P5 in Fig. 36a). This fact easily explains the vertical patterns seen in PADs at crossings of local current sheets.

Furthermore, all simulations of the motion of accelerated elections in similar configurations show the existence of the region in which electrons follow local magnetic field lines

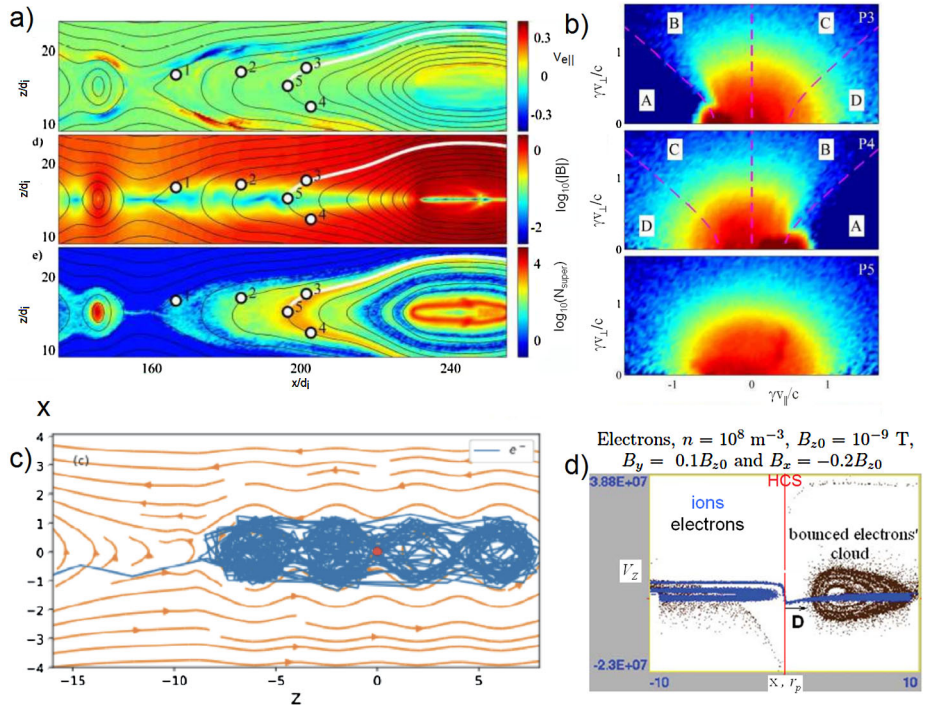

Fig. 36 Examples of the behavior of electrons accelerated locally by dynamical processes in current sheets and magnetic islands. **a**) From top to bottom: results of modeling of the speed component parallel to the magnetic field, the logarithm of IMF strength and the electron density in the reconnecting region across the current sheet, correspondingly. Adapted from Egedal et al. (2015). **b**) Electron distribution function corresponding to points P3, P4 and P5 in **a**). **c**) Acceleration trajectory of an electron (blue) in the chain of merging magnetic islands under a strong guide field. Magnetic field lines are shown by red. Adapted from Xia and Zharkova (2018). **d**) Snapshot of the plasma particles in the x-Vz phase plane for the low density from PIC simulations. The current sheet is shown by the red line. Modified from Zharkova and Khabarova (2012)

and cover magnetic islands like cocoons (Du et al. 2018; Xia and Zharkova 2018, 2020). It is obvious that when a spacecraft passes through such a configuration with closed magnetic field lines, bi-directional patterns in PADs are detected. However, these PAD features occur not because the accelerated electrons come from the Sun, but because these are accelerated locally and move around magnetic islands (Khabarova et al. 2016, 2018a).

An example of the trajectory of an accelerated electron (blue) in the chain of merging magnetic islands is shown in Fig. 36c, adapted from Xia and Zharkova (2018), who tested the behavior of electrons and ions in merging and contracting magnetic islands under different external conditions. It can be seen that the electron trajectory cocoons magnetic islands at the beginning of the acceleration process. Notably, the most energetic electrons move further away from magnetic islands (see Fig. 9 from Xia and Zharkova 2018).

Even if particles are energized in a single ideal current sheet, without the presence of any magnetic islands, accelerated electrons may be found mainly at some distance from the current sheet, where the particles form clouds of various shapes from a locket to a horse-shoe (Zharkova and Khabarova 2012). An example of the corresponding PIC simulations for the heliospheric plasma and IMF parameters is given in Fig. 36d. The red line is the midplane of the reconnecting current sheet, ions are shown by blue and electrons are black dots. The locket of accelerated electrons that cannot go too far from the current sheet is formed at

some distance from the current sheet under the chosen conditions (see the parameters above the panel, and details in Zharkova and Khabarova 2012). If there are many reconnecting sites along the current sheet and many magnetic islands, as suggested by other simulations discussed above, the cloud becomes larger and may be observed several hours after/before the crossing of the current sheet, since the effectiveness of reconnection increases (e.g. Li and Lin 2012). Importantly, simulations by Zharkova and Khabarova (2012) also suggest that both the dispersionless behavior of electrons and dropouts are possible in the nearest vicinity of reconnecting current sheets. Therefore, all key features of the suprathermal electron behavior in the vicinity of dynamical current sheets can be found from numerical simulations.

Figure 37 shows a strong example of the HCS/HPS crossing with a typical mismatch between the IMF and PAD signatures. This crossing may be regarded as classical if identified through the IMF features, according to the decrease in the IMF strength B and the plasma density N, the increase in the plasma beta, the relatively fast change in the azimuthal IMF angle (Bphi), and a classic drop in the alpha to proton ratio within the HPS. The HPS area can be identified clearly in this case, since there are signatures of strong current sheets at both its edges. However, this interpretation can be disputed if one considers the PADs (three upper stripes in Fig. 37a).

Firstly, suprathermal electrons of different energies behave differently, which cannot be if all of the electrons originate from the same source (see the three upper panels in Fig. 37a). Secondly, there is a wide region seen as a dropout in 272 eV, and 73.3 eV channels centered at the HPS identified from the IMF parameters, but 1.37 keV electrons display a smooth change in the direction in the region. Thirdly, the bi-directional pattern is seen in 272 eV and 73.3 eV PADs only, and the area of counterstreaming strahls is wider than the HPS.

At the same time, Fig. 37b shows a moderate enhancement in the keV-MeV energetic ion flux in the region, much wider than the HPS. Note that the irregular spikes seen in the lower-energy channels in Fig. 37b are not determined by acceleration at the HCS and surrounding magnetic islands. These are narrow beams of accelerated ions coming to the spacecraft from the magnetospheric side and representing examples of the Petschek-like magnetic reconnection exhausts. The particles are accelerated due to the interaction of the HCS with the terrestrial bow shock and can be registered for many hours while the HCS/HPS crosses the shock body, especially if there are feed particles pre-accelerated in the HCS/HPS system. The interesting effect of "upstream magnetospheric events" has been known for years and has always been considered to be an unwelcome data contamination (e.g. Gold et al. 1998), but the fact that at least a part of the events is associated with the passage of reconnecting strong current sheets from the solar wind side across the terrestrial magnetosphere was noticed and discussed for the first time in Khabarova and Zank (2017) although a significant impact of the HCS on the terrestrial bowshock has been noticed and admitted a long time ago (e.g., Schwartz et al. 1988).

Taking into account the presence of magnetic islands both inside and outside the HPS (see the rotation of the IMF vector in Fig. 37c), one can interpret the event shown in Fig. 37a, b in the frame of an updated paradigm in the following manner:

– If the spacecraft crosses the HCS/HPS system approximately perpendicular to the midplane (the vertical green dashed line in Fig. 37d), it first approaches the area filled with magnetic islands advected by the solar wind surrounding the HPS (the wide purple stripe in Fig. 37a). The largest magnetic islands (blobs of the coronal origin) are usually found here (see the corresponding statistics in Fig. 28a). The IMF direction becomes unstable, but the dominant direction is still obvious. Ions and suprathermal electrons of moderate

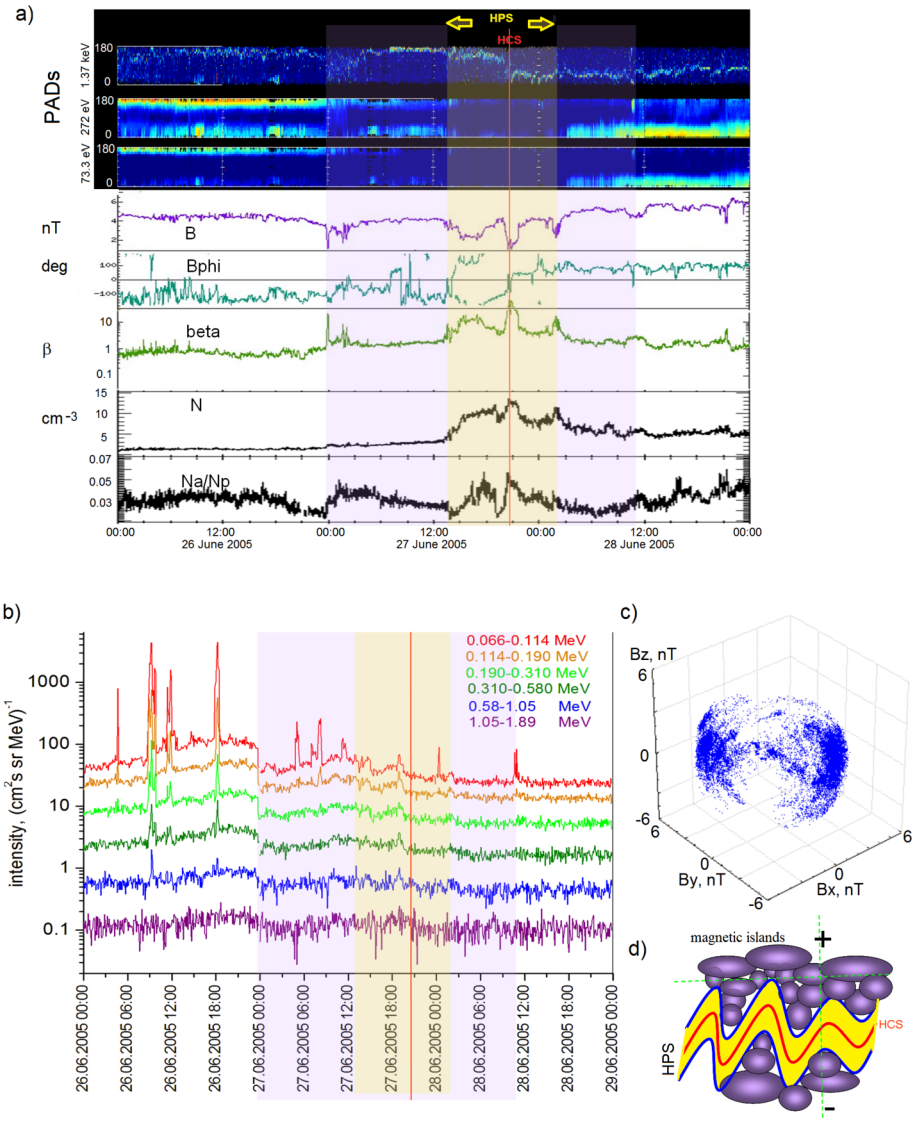

Fig. 37 ACE observations of a HCS/HPS crossing. **a**) From top to bottom: PADs in 1.37 keV, 272 eV, and 73.3 eV energy channels, the IMF strength, the azimuthal IMF angle, the plasma beta, the solar wind density, and the alpha to proton ratio. The wide dropout and bi-directional features in the PADs are due to the presence of magnetic islands. **b**) Energetic ion flux in several channels. The spikes in the lower energy channels in the elevated background (**b**) are upstream magnetospheric events seen in the smooth background of AEPEs. **c**) IMF hodogram for the HPS (yellow) region and the purple region filled with magnetic islands in the nearest vicinity to the HPS. **d**) Sketch that illustrates the cross-section of the rippled HCS. The HCS is shown by the red line, the HPS region is yellow and the nearest to the HPS area filled with magnetic islands is indicated by purple

energies become trapped and/or accelerated by magnetic islands locally, and the corresponding PADs show clear bi-directional signatures (see 272 eV and 73.3 eV PADs in Fig. 37a). At the same time, the most energetic electrons coming from the corona, being too fast to be trapped, and, on the other hand, possessing energies unreachable with the local acceleration mechanisms, still show no changes in the dominant field-aligned pattern (see the upper panel, corresponding to the 1.37 keV PAD).

– Then the spacecraft enters the HPS region (the yellow stripe in Fig. 37a) in which the number of smaller-scale magnetic islands and intensively reconnecting current sheets is so high, and the HCS-associated processes are so intensive, that the collective effects discussed above become dominant. Observations show that ions may be still trapped and accelerated in this area as effectively as in the vicinity of the HPS, but electrons being faster and smaller than ions behave differently. Depending on the IMF and plasma parameters, as well as on the width of the HPS and the manner of its crossing, it is possible to see either a wide gap between the accelerated elections and the HCS (a dropout) or simply dispersionless patterns in PADs (as shown in Fig. 7), except for the most high-energy elections. The latter may indicate a smooth or a sharp change in the strahl's direction as seen in the upper 1.37 keV PAD.
– The manner of leaving the HPS may look similar to entering the island-filled area, but the observed effects of particle acceleration mostly depend on the manner of the particular HCS crossing, and dominate from the internal side of the HCS ripple (see the sketch in Fig. 37d or Fig. 40b below).

As noticed above, simulations of processes of electron acceleration in the HCS/HPS configuration containing magnetic islands increasingly support observations of local electron acceleration associated with local IMF structures. The idea that the bi-directional PAD pattern near the HCS and similarly strong current sheets is caused by acceleration of electrons in magnetic islands with closed IMF lines not connected to the Sun was first suggested by Khabarova et al. (2015, 2016). The most recent studies confirm that suprathermal electrons are very sensitive to the instantaneous magnetic field direction and local plasma structures (Du et al. 2018; Khabarova et al. 2018a, 2020; Xia and Zharkova 2018, 2020).

Khabarova et al. (2020) made two virtual experiments based on 2.5D particle-in-cell (PIC) simulations that clearly showed that both dropouts and bi-directionality/counter-streaming features in PADs might be caused by ongoing local magnetic reconnection at strong current sheets and in the chain of plasmoids not connected to the Sun in any way.

Figure 38 illustrates this by showing PAD features electrons accelerated to suprathermal energies at a reconnecting current sheet (the first experiment). It is found that, during the acceleration process, both ions and electrons become divided into trapped and bounced categories (similar to those shown in Fig. 37d), i.e. they form two distinct populations with quite different energies separated by a threshold. So-called "transit" electrons have the higher energies that allow them to leave the reconnecting current sheet upon acceleration, and "bounced" electrons with the energies below the threshold become trapped and circulate in the vicinity of the current sheet. A report of this phenomenon, one of the most important discoveries about reconnecting current sheets in space plasmas, was first made by Zharkova and Gordovskyy (2005) (see also Siversky and Zharkova 2009; Xia and Zharkova 2018, 2020).

The behavior of electrons belonging to these two populations can be compared if one looks at the upper and lower panels of Fig. 38, respectively. Wide dropouts and bi-directionality are very typical for lower-energy particles, exactly as it is usually seen in observations. Note that details of PAD features depend not only on the energy gained by

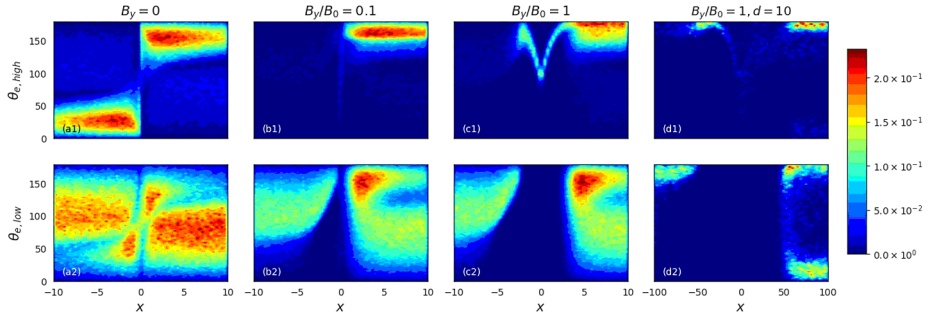

Fig. 38 PIC simulations of PADs for electrons accelerated at a reconnecting strong current sheet. There are two distinguished energy ranges depending on the energy gained by particles during acceleration. Upper panel is for higher energy electrons, and the bottom panel is for lower energy electrons. Three columns from left to right correspond to the increasing guide field B_y strength, and the right (fourth) column is the same as the third but for ten times thicker current sheet (the initial width of which equals one proton gyroradius). Adapted from Khabarova et al. (2020). Simulations show that dropouts (vertical features of the absence of color) and counterstreaming strahls (two co-existing stripes at 0° and 180°) may be caused by local electron acceleration at current sheets in the solar wind

particles, but also on the strength of the guide magnetic field B_y with respect to the maximal magnetic field B_0 and the width of the reconnecting current sheet. In Fig. 38, the guide magnetic field strength gradually increases from the first column to the third, and the fourth column is shown for the same guide magnetic field value but for a ten times wider current sheet.

The difference is dramatic. It is obvious that increasing the width of a reconnecting current sheet leads to the occurrence of a very wide dropout encompassing the current sheet. On the contrary, the location of the thin current sheet not supported by the guide field (the first left column) can be identified with the bright vertical line in higher energy channel PADs and as the center of the diagonal transition feature of the electron motion direction in lower energy channel PADs. An example can be seen in the upper and the lower panel of the first column of Fig. 38.

The second experiment shows that if the same current sheet contains dynamic (merging or contracting) magnetic islands, a crossing of this conglomerate is associated with both dropouts and bi-directional strahls, but the PAD patterns are even more complex than in the pure current sheet crossing case. The results of the experiment on merging magnetic islands are shown in Fig. 39.

A virtual spacecraft passes through the chain of dynamical magnetic islands based on the reconnecting current sheet with the width of two proton gyroradii. Counterstreaming strahls are observed all the way through the island crossing, and the PAD pattern becomes diagonal while the spacecraft crosses the X-shape region with the dominance of the reconnecting current sheet impact. In the low energy channel, the pattern is more dispersionless.

Therefore, Khabarova et al. (2020) have found that long-debated dropouts and bi-directionality seen in PAD patterns may be signatures of local particle acceleration far from the solar corona. It is not necessary to imagine huge loops of magnetic field lines entangling and moving back to the Sun to explain observations conforming to the requirement of a coronal source of suprathermal electrons. The idea of the formation of closed structures (Crooker et al. 2004; Gosling et al. 2006; Baker et al. 2009) was absolutely correct, except for the detail that all processes occur locally, not far from the point of observations, and that the closed loops are closed because they represent a chain or a sea of magnetic islands.

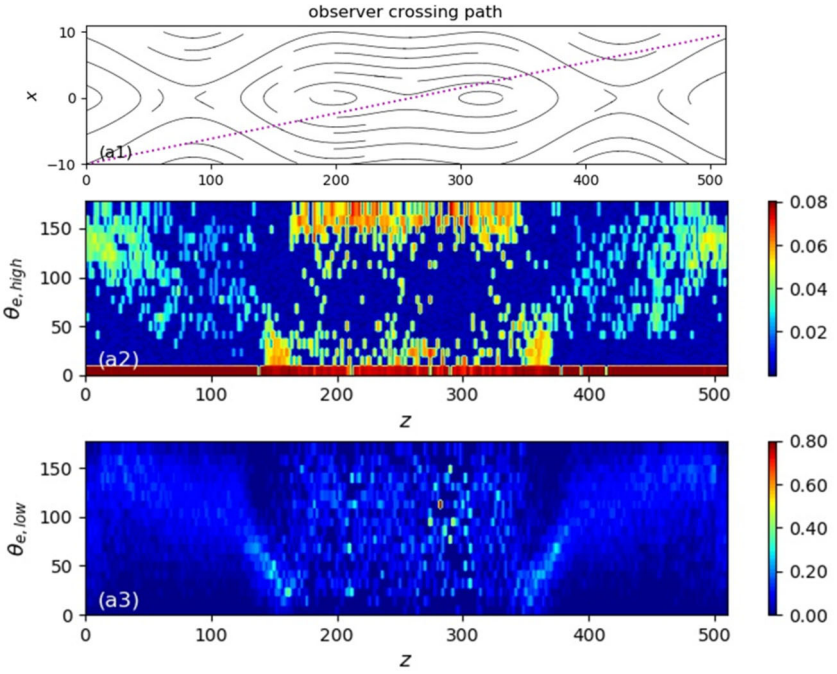

Fig. 39 PADs associated with merging (coalescent) magnetic islands embedded in the reconnecting current sheet. From top to bottom: magnetic field lines (black) through which a virtual spacecraft passes (purple line); PADs of higher and lower energy electrons analogous to Fig. 36. $B_y/B_0 = 0.1$, the current sheet is two times larger than that shown in three panels Fig. 36. For details see Khabarova et al. (2020)

Most recently, the occurrence of local ion and electron acceleration caused by magnetic reconnection has been confirmed by Tan (2020) who showed how easily difficult events, including those seen in properties of particle pitch angles, may be interpreted if one assumes the existence of local sources of accelerated ions and electrons in the solar wind. Indeed, such an approach easily solves many problems of the interpretation of observations of the HCS/HPS, ICME and SIR crossings, because it does not require a magnetic connection of the observational site to the Sun.

Furthermore, the presence of an unaccounted population of locally-born strahls allows one to explain the puzzling decrease of the strahl relative density with heliocentric distance. Knowing that the reconnection rate decreases with heliocentric distance, one may suggest that the input of strahls produced by reconnecting current sheets into the total volume of strahls decreases with distance too. The latter is true in a wider sense: in all cases of HCS crossings, the observed picture strongly depends on topological features of the HCS/HPS system, and, of course, on how the crossing occurs.

Since practically all types of the HCS/HPS crossings were presented above, it is reasonable to show the typical PAD patterns which may be associated with isolated HCS/HPS crossings. The term "isolated" means that the crossing occurred far from a high-speed stream of any origin. Figure 40 illustrates the general conditions under which four main types of PADs associated with the HCS crossings are observed. Figure 40a shows a planar minimally disturbed HCS (purple line) surrounded by some magnetic islands and current sheets forming the HPS (grey area), since magnetic reconnection and magnetic island production occur at the HCS even in the case of simple turbulence that is not considered a major disturbance.

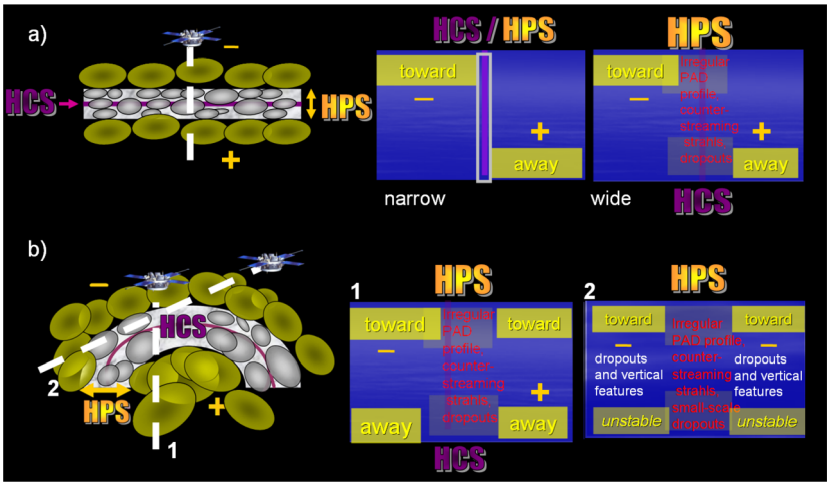

Fig. 40 Most frequently observed types of the HCS/HPS crossings, and corresponding PAD patterns. **a**) Case of the planar undisturbed HCS/HPS (left panel). The HPS filled with secondary current sheets and small-scale magnetic islands is schematically shown as a grey area, and the HCS along which the main current flows inside the HPS is shown as a narrow purple line. Magnetic islands capable of escaping the HPS have the yellow color. Depending on the width of the HPS and the rate of production of magnetic islands, an observer sees either a classic PAD (middle panel) or a region of irregular patterns in the PAD between two regular stripes of the strahl toward/away direction (right panel). **b**) Case of the rippled HCS. Crossing 1 in the middle (PAD) panel corresponds to the dashed line in the left (sketch) panel. It suggests the detection of bi-directional strahls from the both sides of the HPS and the area of mixing direction and/or dropouts in the middle, similar to the right panel in (**a**), but the HCS position is shifted from the center of the HPS. Crossing 2 (the right PAD panel) corresponds to the situation when the spacecraft just scrapes the HPS and magnetic islands outside (see line 2 in the left panel). As a result, the PAD is very complex

The whole system may be surrounded by detached magnetic islands as well as magnetic islands propagating from the corona. In the case of the practically perpendicular section of the system, its size is small enough to interpret the event as a classic HCS crossing (see the middle panel of Fig. 40a). However, if it is crossed under some angle or the entire system is wider because of an increased disturbance level, a wide area of the strange strahl behavior appears in the PAD. The latter may contain dropouts, bi-directional strahls and show dispersionless patterns (see Fig. 6, for example).

If a spacecraft crosses a HCS ripple (Fig. 40b), this corresponds to the condition when the entire HCS/HPS system is disturbed and the dynamical processes occur actively. Therefore, the same perpendicular crossing as shown in Fig. 40a (crossing 1 in Fig. 40b) suggests here far more complex features in PADs. In this case an observer most probably sees the bi-directional pattern in the PAD, the wide disorganized area in the middle and the bi-directional pattern again (an example, corresponding to the middle panel of Fig. 40b, is the event shown in Fig. 39).

The right panel in Fig. 40b illustrates the PAD type that is usually most difficult to understand. However, its nature is very simple. If a spacecraft just skims the HPS, going through the area filled with magnetic islands both near and/or inside the HPS (crossing 2), both the IMF direction and PADs show large variations in key parameters, sometimes even with bi-directional strahls, dropouts or vertical lines in PADs, and then a wide dropout or even the same but more variable features as before (the right panel in Fig. 40b). Despite all clear

signatures of an approaching HCS crossing, the observer finally finds the spacecraft in the same IMF direction after the passage of the outer region filled with magnetic islands.

Sometimes, the HCS may be just touched, then it is considered as the complete HCS crossing as, for instance, the crossing discussed in Khabarova et al. (2015) (the event shown in Fig. 27a). In the case shown in Fig. 40b as crossing 2, the HCS/HPS crossing lasts much longer than in the case of the oblique section of the HCS/HPS system shown in Fig. 40a. The number of typical PADs and crossing types is certainly much larger. For instance, one can imagine what a PAD may look like if a spacecraft crosses two or more ripples of the HCS. Also, there are cases of approaching CIRs/SIRs or an ICME, which are partially discussed above (see the discussion of Fig. 31d, e). The event shown in Fig. 6b is also the case of a SIR interaction with the HCS. One may practice in interpreting it, using the sketch in Fig. 31d and taking into account that (i) the final HCS crossing may or may not coincide with the stream interface, and the SIR may bring any direction of the IMF. It is not necessary to imagine huge loops of magnetic field lines entangling and moving back to the Sun to explain observations conforming to the requirement of a coronal source of suprathermal electrons. The idea of the formation of closed structures (Crooker et al. 2004; Gosling et al. 2006; Baker et al. 2009) was absolutely correct, except for the detail that all processes occur locally, not far from the point of observations, and that the closed loops are closed because they represent a chain or a sea of magnetic islands.

Summarizing, knowledge of the dynamical processes occurring near the HCS and QCSs is very important for the correct interpretation of observations. Finally, one may answer the key question 3 (Q3 in Sect. 2). The behavior of suprathermal electrons in the vicinity of the HCS is so complex and different from what is predicted because there are two populations of suprathermal electrons in the solar wind. One population is represented by "classic" suprathermal electrons of solar origin, but the other is produced by magnetic reconnection and Fermi acceleration in dynamical magnetic islands and current sheets locally in the solar wind. Other effects such as scattering, velocity shears and wave-associated dropouts may also contribute to the picture observed in PADs.

Note that there are both lower/upper thresholds to which particles can be accelerated by mechanisms working in current sheets and magnetic islands. This means that suprathermal electrons become sensitive to local IMF/plasma structures and show some specific patterns in PADs in a limited range of energies, above and below which the behavior of suprathermal electrons from coronal sources dominates again.

4 Summary and Discussion

We have shown that current sheets and plasmoids/blobs/flux ropes/magnetic islands of various scales and origins are closely related structures that occur in all space plasmas which are dynamical and unstable by nature. Consideration of the 3-D nature of these plasma objects is critically important for understanding magnetic reconnection, particle transport and acceleration in the heliosphere. Recent advances in space physics allow answering many questions that bothered generations of plasma physicists. The reader can find the most important conclusions derived from the discussed studies in the end of each subsection of Sects. 2–3. Below, we answer the main questions representing the biggest puzzles for observers.

1. Current sheets in the heliosphere are generally not planar, even at small scales. Simplified consideration of these objects as being 2-D should be approached with caution, since many effects simply do not exist in 2-D.

2. Reconnecting and/or waving current sheets quickly become unstable and transform into a subset of current sheets separated by magnetic structures known as plasmoids, flux ropes or blobs.
3. Plasmoids/blobs/flux ropes are 3-D structures that can be considered as magnetic islands in 2-D. Theoretical studies supported by observations suggest that results obtained for magnetic islands are applicable to all their 3-D counterparts. Meanwhile, further studies of 3-D effects in plasmoids/blobs/flux ropes in the heliosphere is necessary since laboratory experiments show features poorly investigated or even unknown in space plasma.
4. Understanding the fact that current sheets are 3-D and reconnect stochastically at numerous sites helps interpret observations.
5. Particle acceleration may occur both in the solar corona or at interplanetary shocks and locally at dynamical current sheets and magnetic islands in the solar wind. In the absence of seed particles accelerated in other ways (e.g., SEPs), core electrons may be accelerated to keV energies, and protons can be energized up to several MeV/nuc directly in the heliosphere. In combined cases, when seed particles are pre-accelerated to high energies, the impact of local ion acceleration may be observed in energy channels above 5 MeV.
6. Acceleration and re-acceleration of electrons directly in the solar wind to suprathermal energies may explain puzzling PAD features such as heat flux dropouts and counter-streaming (bi-directional) strahls as well as a decrease of the relative strahl density with heliocentric distance.
7. Magnetic confinement of current sheets and magnetic islands in magnetic cavities plays a dramatic role in the intensification of particle acceleration in the heliosphere. Understanding of this phenomenon has become possible because of the development of 3-D views on large and medium-scale dynamical processes occurring in space plasmas.

One of the most frequently discussed points is the 3-D nature of the HCS. So far, we know that the HPS is not planar, it responds to the impact of high-speed streams and flows, and its constant presence in the dynamical solar wind suggests the creation of magnetic islands and other coherent structures. Also, the HCS/HPS conglomerate is a constant source of energetic particles accelerated locally to considerably high (keV-MeV) energies, owing to the development of instabilities and magnetic reconnection. Here we summarize answers to the three main questions regarding the HCS (see Sect. 2)

Q1: *Why are prolonged crossings and, especially, incomplete crossings of the HCS observed?*

First of all, because the HPS in which the HCS embedded exists. Depending on its topology and the manner of its crossing, a spacecraft may stay in the region filled with magnetic islands and current sheets characterized by the variable IMF direction for a shorter or longer time. Secondly, the HCS can possess not just a wavy but a rippled form. In this case, the crossing may be very prolonged because of the existence of numerous magnetic islands filling the ripples.

Q2: *Why do observations often show increases in the energetic ion flux up to MeV/nuc near the HCS?*

Because the dynamical HCS and the surrounding magnetic islands can accelerate and re-accelerate charged particles, owing to the stochastic magnetic reconnection and Fermi mechanisms. The occurrence of magnetic islands and formation of magnetic cavities play a critical role in local particle acceleration in the solar wind.

Q3: *Suprathermal electrons with energies above 70 eV at 1 AU are assumed to originate from the Sun only, and should quickly change the direction of their motion at the HCS.*

Why is the behavior of suprathermal electrons in the vicinity of the HCS so complex and different from what is predicted?

Because the solar corona is not the only source of suprathermal electrons observed in the heliosphere. There is a population of suprathermal electrons created by reconnecting current sheets and dynamical magnetic islands directly in the solar wind. The latter affects the view of PADs of middle-energy suprathermal electrons (typically, with energies from 100 eV to 900 eV). PAD patterns strongly depend on parameters of a particular current sheet and magnetic islands crossed by a spacecraft as well as on the properties of the surrounding solar wind.

The problem of mismatches between the pure IMF identification of the HCS and its identification from PAD spectrograms, problems of observations of heat flux dropouts and dispersionless patterns in PADs, and many others can be solved easily if one takes into account the behavior of electrons accelerated in the HCS/HPS system and magnetic islands. Therefore, although PADs are very helpful in identifying current sheets and, in particular, the HCS, this method should be combined with an analysis of characteristic changes in the IMF and plasma parameters near reconnecting current sheets.

It is important to attract the reader's attention to the point that there is a great practical interest in studying current sheet and magnetic island dynamics. Firstly, unusual (or atypical) energetic particle flux enhancements associated with crossings of magnetic cavities filled with current sheets and magnetic islands can be as dangerous to astronauts and spacecraft equipment as SEP events, since locally-originated energetic particle enhancements possess characteristics similar to SEP events and have energies that overlap with SEPs. Statistics of geostationary communication satellite anomalies show the existence of a source of energetic particles that can be associated neither with ICMEs nor with CIRs, but that can be effective before/after geomagnetic storms (Iucci et al. 2006; Malandraki and Crosby 2018). These features conform fully to characteristics of SMI-filled magnetic cavities observed for a prolonged time either before/after the HCS crossing or before/after CMEs/CIRs that produce geomagnetic storms. One can suggest that this unknown hazardous factor may be SMIs and SMI-produced energetic particle enhancements, which definitely requires further investigations.

Second, SMIs are potentially geoeffective since these are sources of Ultra Low Frequency (ULF) magnetospheric waves caused by the solar wind-magnetosphere interaction (Kozyreva et al. 2007; Romanova and Pilipenko 2009; Shi et al. 2014). Crossings of magnetic cavities filled with magnetic islands can be interpreted as the occurrence of quasi-periodic ULF variations in the IMF and the solar wind density, with a period from minutes to 2 hours (Khabarova et al. 2016). This provides an explanation of the results of prior studies claiming the increased level of ULF oscillations both in the solar wind and geomagnetic field before and after the passage of high-speed streams (Khabarova 2007; Romanova et al. 2007; Khabarova and Dimitrova 2009; Khabarova and Yermolaev 2008). So far, it is known that ULF variations are sources (or a modulation factor) of fluxes of the Van Allen belt's dangerous electrons of MeV energies (e.g., Degeling et al. 2014; Liu et al. 2016), which supports the necessity of the study of the solar wind – magnetosphere connections related to magnetic islands.

There is one more important point concerning the occurrence of current sheets in the heliosphere: these are known to impact the properties of the surrounding solar wind. The stronger a current sheet is, the larger impact can be expected. For example, since most of spacecraft have made their measurements at low heliolatitudes, the occurrence of the HCS near the ecliptic plane may be responsible for observed deviations of the IMF radial dependence from expected (Khabarova and Obridko 2012; Khabarova 2013; Kislov et al. 2015,

2019; Maiewski et al. 2020). Furthermore, high-latitude QCSs formed at the border and within CHs may impact the solar wind speed evolution with heliocentric distance and cause pronounced but spatially confined slowing of the solar wind further from the Earth owing to the inclination of CH borders from high to low heliolatitudes at far heliocentric distances (Khabarova et al. 2018b).

As a final note, it is worthwhile to say that despite the very limited number of spacecraft allowing one to study the structure of the heliosphere and the processes occurring there at different scales, the volume of accumulated observations in the solar wind at different distances and heliolatitudes is enough to make a qualitative leap to the next level of understanding. Currently, this particular branch of space science is approximately at the same level of understanding the material as magnetospheric physics was 20 years ago, and hopefully the results and ideas presented in this review will be useful for future studies of the three-dimensional distribution of currents, dynamical processes associated with current sheets and magnetic islands, as well as for interpreting and modeling particle acceleration and transport in the heliosphere.

It should be admitted that, in this particular scientific branch, all breakthrough results were first obtained from theory and simulations, and observers just followed the suggested lines. The modern understanding of the processes discussed in this review has come from the theory first, especially concerning particle acceleration (see Part II of this review). The producing of magnetic islands by dynamical current sheets was obvious to theoreticians in 1985, and particle acceleration in dynamical magnetic islands was simulated in 1984, but providing observational evidence for these processes in the magnetosphere, and especially in the heliosphere, was substantially delayed for various reasons, including purely technical problems related to the interpretation of one-point measurements.

In part II of this review we discuss theoretical aspects of the physics of current sheets and magnetic islands in space plasmas.

Acknowledgements The authors are grateful to the International Space Science Institute (ISSI) for support of the studies of International Team 405 titled "Current Sheets, Turbulence, Structures and Particle Acceleration in the Heliosphere" (http://www.issibern.ch/teams/structpartaccel/index.html) in 2017–2019. O.K., H.M., R.K., and L.Z. are supported by RSCF grant No. 20-42-04418. O.P. thanks Dr. D. Trotta and Dr. F. Catapano for the friendly and precious conversations on some of the topics discussed in the review. S.S. acknowledges the European Union's Horizon 2020 research and innovation programme under Grant Agreement No. 776262 (AIDA, www.aida-space.eu). J. Le R. acknowledges support from NASA Grant 80NSSC19K027, NSF-DOE grant PHY-1707247, and NSF EPSCoR RII-Track-1 Cooperative Agreement OIA-1655280.

The authors thank the Helioviewer project team (https://helioviewer-project.github.io/). The Helioviewer website images (https://helioviewer.org/) are used in Fig. 11. We thank the HelioWeather project team for providing images and movies at the WSA-ENLIL-DONKI-HELCATS – Solar Wind and CMEs archive (http://www.helioweather.net/archive/2012/03/stb1dej.html). The archive's open-access material is used in Figs. 15 and 22. The Wind and ACE spacecraft data used in Figs. 1, 7, 22, 29, 37 are from https://cdaweb.gsfc.nasa.gov/istp_public/ (thanks to the CDAWeb team). We thank the authors of figures and material used in the review for their tremendous and inspiring work. Figure 13d and Fig. 36c are used under ©ESO 2018. Figure 10b, Fig. 13b, Figs. 23c and 24d are used under the terms of the Creative Commons Attribution 3.0 license. Figure 10a, Fig. 12c, Fig. 15, and Fig. 23d are used under a Creative Commons Attribution 4.0 International License. Figure 3c is reprinted under License Number (LN) 5030790709342, and Fig. 3b – under LN 5030791253352 obtained from https://www.copyright.com. Figure 5: LN 5030800647340; Fig. 6a and Fig. 9a: License LN 5030801081368; Fig. 6b and Fig. 9b: LN 5030801440402. Figure 7a: LN 5030810306882. Figure 8b: LN 5030820100527. Figure 12b: LN 5030861183349. Figure 13a: LN 5030881477005. Figure 13c: LN 5030890789749. Figure 23a: LN 5030901197411; Fig. 23b: LN 5030910243037. Figure 24b: LN 5030911166948 and LN 5030911362867; Fig. 25: LN 5031611008025. Figure 30: LN 5030931339325. Figure 35: LN 5030940784082. Figure 36ab: LN 5030941083300.

Funding Funding is provided by the Russian Science Fundation (RSCF), grant No. 20-42-04418 (contributors: O.K., H.M., R.K., and L.Z.). S.S. is supported by the European Union's Horizon 2020 research and

innovation programme under Grant Agreement No. 776262 (AIDA, www.aida-space.eu). J. Le R. is supported by NASA Grant 80NSSC19K027, NSF-DOE grant PHY-1707247, and NSF EPSCoR RII-Track-1 Cooperative Agreement OIA-1655280.

Data availability All data and material used are from public open-access data depositories and archives (see Acknowledgements for details).

Code availability Not applicable.

Conflicts of interest/Competing interests The authors declare no conflict of interests.

Publisher's Note Springer Nature remains neutral with regard to jurisdictional claims in published maps and institutional affiliations.

References

L. Adhikari, O.V. Khabarova, G.P. Zank, L.-L. Zhao, Astrophys. J. (2019). https://doi.org/10.3847/1538-4357/ab05c6
N. Al-Haddad, I.I. Roussev, C. Möstl et al., Astrophys. J. Lett. (2011). https://doi.org/10.1088/2041-8205/738/2/L18
N. Al-Haddad, S. Poedts, I. Roussev, C.J. Farrugia, W. Yu, N. Lugaz, Astrophys. J. (2019). https://doi.org/10.3847/1538-4357/aaf38d
I. Alexeev, E. Belenkaya, V. Kalegaev, Y. Feldstein, A. Grafe, J. Geophys. Res. (1996). https://doi.org/10.1029/95JA03509
H. Alfvén, Rev. Geophys. (1977). https://doi.org/10.1029/RG015i003p00271
S.K. Antiochos, C.R. DeVore, J.A. Klimchuk, Astrophys. J. (1999). https://doi.org/10.1086/306563
S.K. Antiochos, Z. Mikić, V.S. Titov, R. Lionello, J.A. Linker, Astrophys. J. (2011). https://doi.org/10.1088/0004-637X/731/2/112
V. Archontis, A.W. Hood, Astron. Astrophys. (2010). https://doi.org/10.1051/0004-6361/200913502
C.N. Arge, V.J. Pizzo, J. Geophys. Res. (2000). https://doi.org/10.1029/1999JA000262
L. Arnold, G. Li, X. Li, Y. Yan, Astrophys. J. (2013). https://doi.org/10.1088/0004-637X/766/1/2
C.S. Arridge, in *Magnetotails of Uranus and Neptune Magnetotails in the Solar System*, ed. by A. Keiling, C.M. Jackman, P.A. Delamere. Geophysical Monograph Series, vol. 207 (Wiley, New York, 2015), pp. 119–133. https://doi.org/10.1002/9781118842324.ch7
K. Asai, M. Kojima, M. Tokumaru, A. Yokobe, B.V. Jackson, P.L. Hick, P.K. Manoharan, J. Geophys. Res. (1998). https://doi.org/10.1029/97JA02750
G. Aulanier, T. Török, P. Démoulin, E.E. DeLuca, Astrophys. J. (2010). https://doi.org/10.1088/0004-637X/708/1/314
A.C. Azizabadi, N. Jain, J. Büchner (2020). arXiv:2009.03881
F. Bagenal, Bull. Am. Astron. Soc. **23**, 1152 (1991)
F. Bagenal, in *Encyclopedia of Astronomy and Astrophysics*, ed. by P. Murdin (Institute of Physics Publishing, Bristol, 2001), p. 2322. https://doi.org/10.1888/0333750888/2322
S.M. Bahauddin, S.J. Bradshaw, A.R. Winebarger, Nat. Astron. (2020). https://doi.org/10.1038/s41550-020-01263-2
D.N. Baker, T.I. Pulkinen, V. Angelopoulos, W. Baumjohann, R.L. McPherron, J. Geophys. Res. (1996). https://doi.org/10.1029/95JA03753
D.N. Baker, W.K. Peterson, S. Eriksson, X. Li, J.B. Blake, J.L. Burch, P.W. Daly, M.W. Dunlop, A. Korth, E. Donovan, R. Friedel, T.A. Fritz, H.U. Frey, S.B. Mende, J. Roeder, H.J. Singer, Geophys. Res. Lett. (2002). https://doi.org/10.1029/2002GL015539
D.N. Baker, A.P. Rouillard, L. van Driel-Gesztelyi, P. Démoulin, L.K. Harra, B. Lavraud, J.A. Davies, A. Opitz, J.G. Luhmann, J.-A. Sauvaud, A.B. Galvin, Ann. Geophys. (2009). https://doi.org/10.5194/angeo-27-3883-2009
D. Barnes, J. Geophys. Res. (2020). https://doi.org/10.1029/2019JA027175
W. Baumjohann, R.A. Treumann, in *Basic Space Plasma Physics* (Imperial College Press, London, 1996), pp. 1–340. https://doi.org/10.1142/p015
B. Bavassano, R. Woo, R. Bruno, Geophys. Res. Lett. (1997). https://doi.org/10.1029/97GL01630
A. Bemporad, Astrophys. J. (2008). https://doi.org/10.1086/592377
A. Bemporad, J. Atmos. Sol.-Terr. Phys. (2011). https://doi.org/10.1016/j.jastp.2010.12.007

A. Bemporad, Astrophys. J. (2017). https://doi.org/10.3847/1538-4357/aa7de4
L. Berčič, M. Maksimović, S. Landi, L. Matteini, Mon. Not. R. Astron. Soc. (2019). https://doi.org/10.1093/mnras/stz1007
M.A. Berger, in *Encyclopedia of Complexity and Systems Science*, ed. by R. Meyers (Springer, New York, 2009), p. 558. https://doi.org/10.1007/978-0-387-30440-3
V.S. Beskin, Phys. Usp. (1997). https://doi.org/10.1070/PU1997v040n07ABEH000250
A. Bhardwaj, G.R. Gladstone, P. Zarka, Adv. Space Res. (2001). https://doi.org/10.1016/S0273-1177(01)00280-0
N.H. Bian, E.P. Kontar, Phys. Rev. Lett. (2013). https://doi.org/10.1103/PhysRevLett.110.151101
L. Biermann, A. Schluter, Phys. Rev. (1951). https://doi.org/10.1103/PhysRev.82.863
J. Birn, R. Sommer, K. Schindler, Astrophys. Space Sci. (1975). https://doi.org/10.1007/BF00637005
M.M. Bisi, B.V. Jackson, P.P. Hick et al., J. Geophys. Res. (2008). https://doi.org/10.1029/2008JA013222
M.M. Bisi, B.V. Jackson, A.R. Breen et al., Sol. Phys. (2010). https://doi.org/10.1007/s11207-010-9594-4
J.J. Blanco, J. Rodriguez-Pacheco, M.A. Hidalgo, J. Sequeiros, J. Atmos. Sol.-Terr. Phys. (2006). https://doi.org/10.1016/j.jastp.2006.08.007
A.H. Boozer, Phys. Plasmas (2012). https://doi.org/10.1063/1.4765352
A.L. Borg, M.G.G.T. Taylor, J.P. Eastwood, Ann. Geophys. (2012). https://doi.org/10.5194/angeo-30-761-2012
J.E. Borovsky, J. Geophys. Res. (2008). https://doi.org/10.1029/2007JA012684
G. Borrini, J.M. Wilcox, J.T. Gosling, S.J. Bame, W.C. Feldman, J.M. Wilcox, J. Geophys. Res. (1981). https://doi.org/10.1029/JA086iA06p04565
V. Bothmer, R. Schwenn, Ann. Geophys. (1998). https://doi.org/10.1007/s00585-997-0001-x
J.C. Brandt, F.M. Caputo, Y. Yi, Bull. Am. Astron. Soc. (1992). https://ui.adsabs.harvard.edu/abs/1992AAS..181.9408B/abstract
J.C. Brandt, Y. Yi, C.C. Petersen, M. Snow, Planet. Space Sci. (1997). https://doi.org/10.1016/S0032-0633(97)00049-4
R. Bruno, Earth Space Sci. (2019). https://doi.org/10.1029/2018EA000535
R. Bruno, L.F. Burlaga, A.J. Hundhausen, J. Geophys. Res. (1982). https://doi.org/10.1029/JA087iA12p10339
R. Bruno, V. Carbone, P. Veltri, E. Pietropaolo, B. Bavassano, Planet. Space Sci. (2001). https://doi.org/10.1016/S0032-0633(01)00061-7
J. Büchner, J.-P. Kuska, Adv. Space Res. (1998). https://doi.org/10.1016/S0273-1177(97)00965-4
J. Büchner, L. Zelenyi, J. Geophys. Res. (1989). https://doi.org/10.1029/JA094iA09p11821
A. Buffington, M.M. Bisi, J.M. Clover, P.P. Hick, B.V. Jackson, T.A. Kuchar, Astrophys. J. (2008). https://doi.org/10.1086/529039
R.A. Burger, T.P.J. Krüger, M. Hitge, N.E. Engelbrecht, Astrophys. J. (2008). https://doi.org/10.1086/525039
B.L. Burkholder, A. Otto, P.A. Delamere et al., J. Geophys. Res. (2019). https://doi.org/10.1029/2018JA026132
P.J. Cargill, A.W. Hood, S. Migliuolo, Astrophys. J. (1986). https://doi.org/10.1086/164612
M.L. Cartwright, M.B. Moldwin, J. Geophys. Res. (2008). https://doi.org/10.1029/2008JA013389
M.L. Cartwright, M.B. Moldwin, J. Geophys. Res. (2010). https://doi.org/10.1029/2009JA014271
P.A. Cassak, M.A. Shay, J.F. Drake, Phys. Plasmas (2009). https://doi.org/10.1063/1.3274462
X. Cao, C. Paty, J. Geophys. Res. (2017). https://doi.org/10.1002/2017JA024063
M. Cécere, M.V. Sieyra, H. Cremades et al., Adv. Space Res. (2020). https://doi.org/10.1016/j.asr.2019.08.043
S. Chapman, V. Ferraro, Terr. Magn. Atmos. Electr. (1931). https://doi.org/10.1029/TE036i003p00171
H. Che, J.F. Drake, M. Swisdak, Nature (2011). https://doi.org/10.1038/nature10091
J. Chen, Phys. Plasmas (2017). https://doi.org/10.1063/1.4993929
Y. Chen, Q. Hu, J. le Roux, J. Zheng, J. Phys. Conf. Ser. (2018). https://doi.org/10.1088/1742-6596/1100/1/012006
B. Chen, C. Shen, D.E. Gary et al., Nat. Astron. (2020a). https://doi.org/10.1038/s41550-020-1147-7
C.H.K. Chen, S.D. Bale, J.W. Bonnell et al., Astrophys. J. Suppl. Ser. (2020b). https://doi.org/10.3847/1538-4365/ab60a3
R. Chhiber, M.L. Goldstein, B.A. Maruca et al., Astrophys. J. Suppl. Ser. (2020). https://doi.org/10.3847/1538-4365/ab53d2
A.C.-L. Chian, P.R. Muñoz, Astrophys. J. Lett. (2011). https://doi.org/10.1088/2041-8205/733/2/L34
P.A. Cloutier, C.C. Law, D.H. Crider et al., Geophys. Res. Lett. (1999). https://doi.org/10.1029/1999GL900591
I.J. Cohen, S.J. Schwartz, K.A. Goodrich et al., J. Geophys. Res. (2019). https://doi.org/10.1029/2018JA026197

F. Comeron, L. Kaper, Astron. Astrophys. **338**, 273 (1998). https://ui.adsabs.harvard.edu/abs/1998A&A...338..273C/abstract
L. Comisso, L. Sironi, Astrophys. J. (2019). https://doi.org/10.3847/1538-4357/ab4c33
T.E. Cravens, T.I. Gombosi, Adv. Space Res. (2004). https://ui.adsabs.harvard.edu/abs/2004AdSpR..33.1968C/abstract
N.U. Crooker, D.E. Larson, S.W. Kahler, S.M. Lamassa, H.E. Spence, Geophys. Res. Lett. (2003). https://doi.org/10.1029/2003GL017036
N.U. Crooker, S.W. Kahler, D.E. Larson, R.P. Lin, J. Geophys. Res. (2004). https://doi.org/10.1029/2003JA010278
A. Czechovski, M. Strumnik, J. Grygorczuk, S. Grzedzielski, R. Ratkiewicz, K. Scherer, Astron. Astrophys. (2010). https://doi.org/10.1051/0004-6361/200913542
I.A. Daglis, L.C. Chang, S. Dasso, N. Gopalswamy, O.V. Khabarova, E. Kilpua, R. Lopez, D. Marsh, K. Matthes, D. Nandi, A. Seppälä, K. Shiokawa, R. Thiéblemont, Q. Zong, Ann. Geophys. (2021). https://doi.org/10.5194/angeo-2020-94
R.B. Dahlburg, G. Einaudi, Adv. Space Res. (2003). https://doi.org/10.1016/s0273-1177(03)00317-x
R.B. Dahlburg, J.T. Karpen, J. Geophys. Res. (1995). https://doi.org/10.1029/95JA02496
J.T. Dahlin, J.F. Drake, M. Swisdak, Phys. Plasmas (2017). https://doi.org/10.1063/1.4986211
L. Dai, J.R. Wygant, C.A. Cattel, S. Thaller, K. Kersten, A. Breneman, X. Tang, Geophys. Res. Lett. (2014). https://doi.org/10.1002/2014GL059223
S. Dasso, M.S. Nakwacki, P. Démoulin, C.H. Mrini, Sol. Phys. (2007). https://doi.org/10.1007/s11207-007-9034-2
W. Daughton, V. Roytershteyn, H. Karimabadi et al., Nat. Phys. (2011). https://doi.org/10.1038/nphys1965
L. Davis, Proc. IAU Symp. (1965). https://ui.adsabs.harvard.edu/abs/1965IAUS...22..202D/abstract
C.E. DeForest, W.H. Matthaeus, N.M. Viall, S.R. Cranmer, Astrophys. J. (2016). https://doi.org/10.3847/0004-637X/828/2/66
C.E. DeForest, R.A. Howard, M. Velli, N. Viall, A. Vourlidas, Astrophys. J. (2018). https://doi.org/10.3847/1538-4357/aac8e3
A.W. Degeling, R. Rankin, Q.-G. Zong, J. Geophys. Res. (2014). https://doi.org/10.1002/2013JA019672
T. DeHaas, W. Gekelman, Phys. Plasmas (2017). https://doi.org/10.1063/1.4991413
C.R. DeVore, S.K. Antiochos, Astrophys J. (2008). https://ui.adsabs.harvard.edu/abs/2008ApJ...680..740D/abstract
S. Di Matteo, N.M. Viall, L. Kepko, S. Wallace, C.N. Arge, P. MacNeice, J. Geophys. Res. (2019). https://doi.org/10.1029/2018ja026182
X.-C. Dong, M.W. Dunlop, T.-Y. Wang et al., J. Geophys. Res. (2018). https://doi.org/10.1029/2018JA025292
J.F. Drake, M. Swisdak, H. Che, M.A. Shay, Nature (2006). https://doi.org/10.1038/nature05116
J.F. Drake, M. Opher, M. Swisdak, J.N. Chamoun, Astrophys. J. (2010). https://doi.org/10.1088/0004-637X/709/2/963
S. Du, F. Guo, G.P. Zank, X. Li, A. Stanier, Astrophys. J. (2018). https://doi.org/10.3847/1538-4357/aae30e
E. Dubinin, R. Lundin, W. Riedler, K. Schwingenschuh, J.G. Luhmann, C.T. Russell, L.H. Brace, J. Geophys. Res. (1991). https://doi.org/10.1029/91JA01102
E. Dubinin, M. Fraenz, A. Fedorov, R. Lundin, N. Edberg, F. Duru, O. Vaisberg, Space Sci. Rev. (2011). https://doi.org/10.1007/s11214-011-9831-7
J.P. Eastwood, A. Balogh, M.W. Dunlop, C.W. Smith, J. Geophys. Res. (2002). https://doi.org/10.1029/2001JA009158
J.P. Eastwood, T.D. Phan, F.S. Mozer, M.A. Shay, M. Fujimoto, A. Retinò, M. Hesse, A. Balogh, E.A. Lucek, I. Douras, J. Geophys. Res. (2007). https://doi.org/10.1029/2006JA012158
J.K. Edmondson, B.J. Lynch, Astrophys. J. (2017). https://doi.org/10.3847/1538-4357/aa83ba
J.K. Edmondson, B.J. Lynch, S.K. Antiochos, C.R. DeVore, T.H. Zurbuchen, Astrophys. J. (2009). https://doi.org/10.1088/0004-637X/707/2/1427
J.K. Edmondson, S.K. Antiochos, C.R. DeVore, B.J. Lynch, T.H. Zurbuchen, Astrophys. J. (2010). https://doi.org/10.1088/0004-637X/714/1/517
J. Egedal, W. Daughton, A. Le, A.L. Borg, Phys. Plasmas (2015). https://doi.org/10.1063/1.4933055
N.E. Engelbrecht, Astrophys. J. (2019). https://doi.org/10.3847/1538-4357/aafe7f
J. Enžl, J. Šafránková, Z. Němeček, L. Přech, Astrophys. J. (2017). https://doi.org/10.3847/1538-4357/aa98e0
R.E. Ergun, N. Ahmadi, L. Kromyda et al., Astrophys. J. (2020). https://doi.org/10.3847/1538-4357/ab9ab6
S. Eriksson, D.L. Newman, G. Lapenta, V. Angelopoulos, Plasma Phys. Control. Fusion (2014). https://doi.org/10.1088/0741-3335/56/6/064008
G. Eyink, Astrophys. J. (2015). https://doi.org/10.1088/0004-637X/807/2/137
G. Eyink, A. Lazarian, E. Vishniac, Astrophys. J. (2011). https://doi.org/10.1088/0004-637X/743/1/51

C.J. Eyles, R.A. Harrison, C.J. Davis et al., Sol. Phys. (2009). https://doi.org/10.1007/s11207-008-9299-0
W.C. Feldman, J.R. Asbridge, S.J. Bame, E.E. Fenimore, J.T. Gosling, J. Geophys. Res. (1981). https://doi.org/10.1029/JA086iA07p05408
Y. Feng, M. Kobayashi, T. Lunt, D. Reiter, Plasma Phys. Control. Fusion (2011). https://doi.org/10.1088/0741-3335/53/2/024009
B.P. Filippov, ASP Conf Ser. (1997). http://adsabs.harvard.edu/full/1998ASPC..150..342F
B. Filippov, O. Martsenyuk, A.K. Srivastava, W. Uddin, J. Astrophys. Astron. (2015). https://doi.org/10.1007/s12036-015-9321-5
R.J. Fitzenreiter, K.W. Ogilvie, Heat flux dropouts in the solar wind and Coulomb scattering effects. J. Geophys. Res. (1992). https://doi.org/10.1029/92JA00432
G.D. Fleishman, I.N. Toptygin, in *Cosmic Electrodynamics. Electrodynamics and Magnetic Hydrodynamics of Cosmic Plasmas*. Astrophysics and Space Science Library (Springer, New York, 2013), p. 517. https://doi.org/10.1007/978-1-4614-5782-4_11
G.D. Fleishman, E.P. Kontar, G.M. Nita, D.E. Gary, Astrophys. J. Lett. (2011). https://doi.org/10.1088/2041-8205/731/1/L19
G.D. Fleishman, D.E. Gary, B. Chen, N. Kuroda, S. Yu, G.M. Nita, Science (2020). https://doi.org/10.1126/science.aax6874
T.G. Forbes, J.A. Linker, J. Chen et al., Space Sci. Rev. (2006). https://doi.org/10.1007/s11214-006-9019-8
R.J. Forsyth, V. Bothmer, C. Cid et al., Space Sci. Rev. (2006). https://doi.org/10.1007/s11214-006-9022-0
C. Foullon, C.J. Owen, S. Dasso et al., Sol. Phys. (2007). https://doi.org/10.1007/s11207-007-0355-y
C. Foullon, B. Lavraud, N.C. Wardle et al., Sol. Phys. (2009). https://doi.org/10.1007/s11207-009-9452-4
I. Furno, T.P. Intrator, E.W. Hemsing et al., Phys. Plasmas (2005). https://doi.org/10.1063/1.1894418
H.P. Furth, J. Killeen, M.N. Rosenbluth, Phys. Fluids (1963). https://doi.org/10.1063/1.1706761
A.A. Galeev, M.M. Kuznetsova, L.M. Zelenyi, Space Sci. Rev. (1986). https://doi.org/10.1007/BF00227227
W. Gekelman, E. Lawrence, B. Van Compernolle, Astrophys. J. (2012). https://doi.org/10.1088/0004-637X/753/2/131
W. Gekelman, B. Van Compernolle, T. DeHaas, S. Vincena, Plasma Phys. Control. Fusion (2014). https://doi.org/10.1088/0741-3335/56/6/064002
W. Gekelman, T. DeHaas, W. Daughton et al., Phys. Rev. Lett. (2016). https://doi.org/10.1103/PhysRevLett.116.235101
W. Gekelman, T. DeHaas, P. Pribyl, Astrophys. J. (2018). https://doi.org/10.3847/1538-4357/aa9fec
M.K. Georgoulis, A. Nindos, H. Zhang, Philos. Trans. R. Soc. A (2019). https://doi.org/10.1098/rsta.2018.0094
S.E. Gibson, Living Rev. Sol. Phys. (2018). https://doi.org/10.1007/s41116-018-0016-2
S.I. Glazyrin, A.S. Kuratov, V.Yu. Bychenkov, JETP Lett. (2016). https://doi.org/10.1134/S0021364016040068
T. Gold, J. Geophys. Res. **64**, 1665 (1959)
R. Gold, S. Krimigis, S. Hawkins et al., Space Sci. Rev. (1998). https://doi.org/10.1023/A:1005088115759
W.D. Gonzalez, B.T. Tsurutani, P.S. McIntosh, A.L. Clúa de Gonzalez, Geophys. Res. Lett. (1996). https://doi.org/10.1029/96GL02393
W.D. Gonzalez, B.T. Tsurutani, A.L. Clua de Gonzalez, Space Sci. Rev. (1999). https://doi.org/10.1023/A:1005160129098
N. Gopalswamy, P. Makela, H. Xie, S. Akiyama, S. Yashiro, J. Geophys. Res. (2009). https://doi.org/10.1029/2008JA013686
J. Gosling, V. Pizzo, Space Sci. Rev. (1999). https://doi.org/10.1023/A:1005291711900
J.T. Gosling, J.R. Asbridge, S.J. Bame, W.C. Feldman, E. Hildner, J. Geophys. Res. (1977). https://doi.org/10.1029/JA082i032p05005
J.T. Gosling, R.M. Skoug, D.J. McComas, J.E. Mazur, Astrophys. J. (2004). https://doi.org/10.1086/423368
J.T. Gosling, R.M. Skoug, D.K. Haggerty, D.J. McComas, Geophys. Res. Lett. (2005a). https://doi.org/10.1029/2005GL023357
J.T. Gosling, R.M. Skoug, D.J. McComas, C.W. Smith, J. Geophys. Res. (2005b). https://doi.org/10.1029/2004JA010809
J.T. Gosling, D.J. McComas, R.M. Skoug, C.W. Smith, Geophys. Res. Lett. (2006). https://doi.org/10.1029/2006GL027188
J.T. Gosling, S. Eriksson, D.J. McComas, T.D. Phan, R.M. Skoug, J. Geophys. Res. (2007). https://doi.org/10.1029/2007JA012418
G.A. Graham, I.J. Rae, C.J. Owen et al., J. Geophys. Res. (2017). https://doi.org/10.1002/2016JA023656
A. Greco, W.H. Matthaeus, S. Servidio, P. Chuychai, P. Dmitruk, Astrophys. J. (2009). https://doi.org/10.1088/0004-637X/691/2/L111
A. Greco, S. Perri, S. Servidio, E. Yordanova, P. Veltri, Astrophys. J. Lett. (2016). https://doi.org/10.3847/2041-8205/823/2/L39

A. Greco, W.H. Matthaeus, S. Perri, K.T. Osman, S. Servidio, M. Wan, P. Dmitruk, Space Sci. Rev. (2018). https://doi.org/10.1007/s11214-017-0435-8
E.E. Grigorenko, A.Yu. Malykhin, E.A. Kronberg, Kh.V. Malova, P.W. Daly, J. Geophys. Res. (2015). https://doi.org/10.1002/2015JA021314
E.E. Grigorenko, E.A. Kronberg, P.W. Daly, Cosm. Res. (2017). https://doi.org/10.1134/S0010952517010063
E.E. Grigorenko, S.D. Shuvalov, H.V. Malova, E. Dubinin, V.Yu. Popov, L.M. Zelenyi, J.P. McFadden, J.E.P. Connerney, J. Epsley, J. Geophys. Res. (2018). https://doi.org/10.1002/2017JA024216
E.E. Grigorenko, L.M. Zelenyi, G. DiBraccio, V.N. Ermakov, S.D. Shuvalov, H.V. Malova et al., Geophys. Res. Lett. (2019). https://doi.org/10.1029/2019GL082709
K. Gringauz, V. Bezrukikh, V. Ozerov, R. Rybchinskii, Sov. Phys. Dokl. **5**, 361 (1960). https://ui.adsabs.harvard.edu/abs/1960SPhD....5..361G/abstract
F. Guo, Y.-H. Liu, X. Li, H. Li, W. Daughton, P. Kilian, Phys. Plasmas (2020). https://doi.org/10.1063/5.0012094
H. Gutiérrez, L. Taliashvili, Z. Mouradian, Adv. Space Res. (2013). https://doi.org/10.1016/j.asr.2012.03.008
M. Hamrin, H. Gunell, J. Lindkvist, P.-A. Lindqvist, R.E. Ergun, B.L. Giles, J. Geophys. Res. (2018). https://doi.org/10.1002/2017JA024826
H. Hasegawa, B.U.Ö. Sonnerup, Q. Hu, T. Nakamura, J. Geophys. Res. (2014). https://doi.org/10.1002/2013JA019180
L.-N. Hau, B.U.Ö. Sonnerup, J. Geophys. Res. (1999). https://doi.org/10.1029/1999JA900002
S.G. Heinemann, M. Temmer, C.J. Farrugia et al., Sol. Phys. (2019). https://doi.org/10.1007/s11207-019-1515-6
P. Helander, C.D. Beidler, T.M. Bird et al., Plasma Phys. Control. Fusion (2012). https://doi.org/10.1088/0741-3335/54/12/124009
A.K. Higginson, B.J. Lynch, Astrophys. J. (2018). https://doi.org/10.3847/1538-4357/aabc08
A.K. Higginson, S.K. Antiochos, C.R. DeVore, P.F. Wyper, T.H. Zurbuchen, Astrophys. J. Lett. (2017). https://doi.org/10.3847/2041-8213/aa6d72
C. Ho, B. Tsurutani, R. Sakurai, B. Goldstein, A. Balogh, J. Phillips, Astron. Astrophys. (1996). https://ui.adsabs.harvard.edu/abs/1996AA...316..346H/abstract
M. Hofstadter, A. Simon, S. Atreya et al., Planet. Space Sci. (2019). https://doi.org/10.1016/j.pss.2019.06.004
M. Hoshino, A. Nishida, T. Yamamoto, S. Kokubun, Geophys. Res. Lett. (1994). https://doi.org/10.1029/94GL02094
S. Hosteaux, E. Chané, B. Decraemer, D.-C. Talpeanu, S. Poedts, Astron. Astrophys. (2018). https://doi.org/10.1051/0004-6361/201832976
Q. Hu, Sol. Phys. (2017). https://doi.org/10.1007/s11207-017-1134-z
Q. Hu, B.U.Ö. Sonnerup, J. Geophys. Res. (2003). https://doi.org/10.1029/2002JA009323
Q. Hu, J. Qiu, B. Dasgupta, A. Khare, G.M. Webb, Astrophys. J. (2014). https://doi.org/10.1088/0004-637X/793/1/53
Y.-M. Huang, L. Comisso, A. Bhattacharjee, Astrophys. J. (2017). https://doi.org/10.3847/1538-4357/aa906d
W.J. Hughes, D.G. Sibeck, J. Geophys. Res. (1987). https://doi.org/10.1029/GL014i006p00636
A.J. Hundhausen, in *Coronal Expansion and Solar Wind. Physics and Chemistry in Space*, vol. 5 (Springer, Berlin, 1972), pp. 121–158. https://doi.org/10.1007/978-3-642-65414-5_5
A.J. Hundhausen, in *The Many Faces of the Sun, Scientific Highlights of the Solar Maximum Mission*, ed. by K.T. Strong, J.L.R. Saba, B.M. Haisch, J. Schmelz (Springer, New York, 1999), p. 143. https://doi.org/10.1007/978-1-4612-1442-7_5
F.M. Ipavich, A.B. Galvin, G. Gloeckler, D. Hovestadt, B. Klecker, M. Scholer, Geophys. Res. Lett. (1984). https://doi.org/10.1029/GL011i005p00504
N. Iucci, L.I. Dorman, A.E. Levitin, A.V. Belov, E.A. Eroshenko, N.G. Ptitsyna, G. Villoresi, G.V. Chizhenkov, L.I. Gromova, M. Parisi, M.I. Tyasto, V.G. Yanke, Adv. Space Res. (2006). https://doi.org/10.1016/j.asr.2005.03.028
K. Iwai, D. Shiota, M. Tokumaru, K. Fujiki, M. Den, Y. Kubo, Earth Planets Space (2019). https://doi.org/10.1186/s40623-019-1019-5
C.M. Jackman, C.S. Arridge, N. Andre, F. Bagenal, J. Birn, M.P. Freeman, X. Jia, A. Kidder, S.E. Milan, A. Radioti, J.A. Slavin, M.F. Vogt, M. Volwerk, A.P. Walsh, Space Sci. Rev. (2014a). https://doi.org/10.1007/s11214-014-0060-8
C.M. Jackman, J.A. Slavin, M.G. Kivelson, D.J. Southwood, N. Achilleos, M.F. Thomsen, G.A. DiBraccio, J.P. Eastwood, M.P. Freeman, M.K. Dougherty, M.F. Vogt, J. Geophys. Res. Space Phys. (2014b). https://doi.org/10.1002/2013JA019388
B.V. Jackson, P.P. Hick, A. Buffington, M.M. Bisi, J.M. Clover, Ann. Geophys. (2009). https://doi.org/10.5194/angeo-27-4097-2009

M. Janvier, P. Démoulin, S. Dasso, Sol. Phys. (2014). https://doi.org/10.1007/s11207-014-0486-x
Y.-D. Jia, M.R. Combi, K.C. Hansen, T.I. Gombosi, J. Geophys. Res. (2007). https://doi.org/10.1029/2006JA012175
X. Jia, K.C. Hansen, T.I. Gombosi, M.G. Kivelson, G. Tóth, D.L. DeZeeuw, A.J. Ridley, J. Geophys. Res. (2012). https://doi.org/10.1029/2012JA017575
L. Jian, C.T. Russell, J.G. Luhmann, R.M. Skoug, Sol. Phys. (2006). https://doi.org/10.1007/s11207-006-0132-3
L.K. Jian, C.T. Russell, J.G. Luhmann, R.M. Skoug, J.T. Steinberg, Sol. Phys. (2008). https://doi.org/10.1007/s11207-008-9204-x
L.K. Jian, C.T. Russell, J.G. Luhmann, A.B. Galvin, P.J. MacNeice, Sol. Phys. (2009). https://doi.org/10.1007/s11207-009-9445-3
L.K. Jian, C.T. Russell, J.G. Luhmann, P.J. MacNeice, D. Odstrčil, P. Riley, J.A. Linker, R.M. Skoug, J.T. Steinberg, Sol. Phys. (2011). https://doi.org/10.1007/s11207-011-9858-7
L.K. Jian, J.G. Luhmann, C.T. Russell, A.B. Galvin, Sol. Phys. (2019). https://doi.org/10.1007/s11207-019-1416-8
G. Jones, A. Balogh, T. Horbury, Nature (2000). https://doi.org/10.1038/35007011
R. Kataoka, T. Ebisuzaki, K. Kusano, D. Shiota, S. Inoue, T.T. Yamamoto, M. Tokumaru, J. Geophys. Res. (2009). https://doi.org/10.1029/2009JA014167
O.V. Khabarova, Sun Geosph. (2007). http://adsabs.harvard.edu/abs/2007SunGe...2...33K
O.V. Khabarova, Astron. Rep. (2013). https://doi.org/10.1134/S1063772913110024
O.V. Khabarova, S. Dimitrova, Sun Geosph. (2009). http://adsabs.harvard.edu/abs/2009SunGe...4...60K
O. Khabarova, V. Obridko, Astrophys. J. (2012). https://doi.org/10.1088/0004-637X/761/2/82
O.V. Khabarova, Yu.I. Yermolaev, J. Atmos. Sol.-Terr. Phys. (2008). https://doi.org/10.1016/j.jastp.2007.08.024
O.V. Khabarova, G.P. Zank, Astrophys. J. (2017). https://doi.org/10.3847/1538-4357/aa7686
O. Khabarova, G. Zastenker, Sol. Phys. (2011). https://doi.org/10.1007/s11207-011-9719-4
O. Khabarova, G.P. Zank, G. Li, J.A. le Roux, G.M. Webb, A. Dosch, O.E. Malandraki, Astrophys. J. (2015). https://doi.org/10.1088/0004-637X/808/2/181
O. Khabarova, G.P. Zank, G. Li, O.E. Malandraki, J.A. le Roux, G.M. Webb, Astrophys. J. (2016). https://doi.org/10.3847/0004-637X/827/2/122
O.V. Khabarova, H.V. Malova, R.A. Kislov, L.M. Zelenyi, V.N. Obridko, A.F. Kharshiladze, M. Tokumaru, J.M. Sokół, S. Grzedzielski, K. Fujiki, Astrophys. J. (2017a). https://doi.org/10.3847/1538-4357/836/1/108
O.V. Khabarova, G.P. Zank, O.E. Malandraki, G. Li, J.A. le Roux, G.M. Webb, Sun Geosph. (2017b). http://adsabs.harvard.edu/abs/2017SunGe..12...23K
O.V. Khabarova, O.E. Malandraki, G.P. Zank, G. Li, J.A. le Roux, G.M. Webb, Proc. Int. Astron. Union (2018a). https://doi.org/10.1017/S1743921318000285
O.V. Khabarova, V.N. Obridko, R.A. Kislov, H.V. Malova, A. Bemporad, L.M. Zelenyi, V.D. Kuznetsov, A.F. Kharshiladze, Plasma Phys. Rep. (2018b). https://doi.org/10.1134/S1063780X18090064
O. Khabarova, V. Zharkova, Q. Xia, O.E. Malandraki, Astrophys. J. Lett. (2020). https://doi.org/10.3847/2041-8213/ab8cb8
O. Khabarova, T. Sagitov, R. Kislov, G. Li (2021). arXiv:2101.02804
K. Khurana, M. Kivelson, V. Vasyliunas, N. Krupp, J. Woch, A. Lagg, B. Mauk, W. Kurth, in *Jupiter. The Planet, Satellites and Magnetosphere*, ed. by F. Bagenal, T.E. Dowling, W.B. McKinnon (Cambridge University Press, Cambridge, 2004), p. 593
E. Kilpua, H.E.J. Koskinen, T.I. Pulkkinen, Living Rev. Sol. Phys. (2017). https://doi.org/10.1007/s41116-017-0009-6
Y.J. Kim, R.-Y. Kwon, J. Chae, J. Korean Astron. Soc. (2020). https://ui.adsabs.harvard.edu/abs/2020JKAS...53....1K/abstract
D. Kirtley, J.T. Slough, M. Pfaff, Ch. Pihl, Steady operation of an electromagnetic plasmoid thruster. Semantic Scholar (2011). https://www.semanticscholar.org/paper/STEADY-OPERATION-OF-AN-ELECTROMAGNETIC-PLASMOID-Kirtley-Slough/5e063e730bbaa3022de5d0dc8ca415e795dfa76c. Accessed 7 October 2020
R.A. Kislov, Kh.V. Malova, I.Yu. Vas'ko, Moscow Univ. Phys. Bull. (2013). https://doi.org/10.3103/S0027134913010104
R.A. Kislov, O. Khabarova, H.V. Malova, J. Geophys. Res. (2015). https://doi.org/10.1002/2015JA021294
R.A. Kislov, O.V. Khabarova, H.V. Malova, Astrophys. J. (2019). https://doi.org/10.3847/1538-4357/ab0dff
I.N. Kitiashvili, A.G. Kosovichev, N.N. Mansour, A.A. Wray, Astrophys. J. (2015). https://doi.org/10.1088/0004-637X/809/1/84
M.G. Kivelson, F. Bagenal, in *Encyclopedia of the Solar System*, ed. by L.-A. McFadden, P.R. Weissman, T.V. Johnson, 2nd edn. (Academic Press, Cambridge, 2007), p. 519. https://doi.org/10.1016/B978-012088589-3/50032-3

G. Kowal, A. Lazarian, E.T. Vishniac, K. Otmianowska-Mazur, Nonlinear Process. Geophys. (2012). https://doi.org/10.5194/npg-19-297-2012
O. Kozyreva, V. Pilipenko, M.J. Engebretson, K. Yumoto, J. Watermann, N. Romanova, Planet. Space Sci. (2007). https://doi.org/10.1016/j.pss.2006.03.013
A.M. Krymskii, T.K. Breus, N.F. Ness, M.H. AcuÑa, Space Sci. Rev. (2000). https://doi.org/10.1023/A:1005206515578
J. Kuijpers, H.U. Frey, L. Fletcher, Space Sci. Rev. (2015). https://doi.org/10.1007/s11214-014-0041-y
S. Kumar, R. Bhattacharyya, B. Dasgupta, M.S. Janaki, Phys. Plasmas (2017). https://doi.org/10.1063/1.4996013
Y. Kuramitsu, T. Moritaka, Y. Sakawa et al., Nat. Commun. (2018). https://doi.org/10.1038/s41467-018-07415-3
V.D. Kuznetsov, A.W. Hood, Sol. Phys. (1997). https://doi.org/10.1023/A:1004907300442
V.D. Kuznetsov, A.W. Hood, Adv. Space Res. (2000). https://doi.org/10.1016/S0273-1177(99)01097-2
V.D. Kuznetsov, A.I. Osin, Phys. Lett. A (2018). https://doi.org/10.1016/j.physleta.2018.05.029
V.D. Kuznetsov, A.I. Osin, Phys. Lett. A (2020). https://doi.org/10.1016/j.physleta.2020.126346
R.-Y. Kwon, A. Vourlidas, D. Webb, Astrophys. J. (2016). https://doi.org/10.3847/0004-637X/826/1/94
C.C. Lalescu, Y.-K. Shi, G.L. Eyink, T.D. Drivas, E.T. Vishniac, A. Lazarian, Phys. Rev. Lett. (2015). https://doi.org/10.1103/PhysRevLett.115.025001
A. Lampasi, G. Maffia, F. Alladio, L. Boncagni, F. Causa, E. Giovannozzi, L.A. Grosso, A. Mancuso, P. Micozzi, V. Piergotti, G. Rocchi, A. Sibio, B. Tilia, V. Zanza, Energies (2016). https://doi.org/10.3390/en9070508
L.J. Lanzerotti, R.E. Gold, K.A. Anderson, T.P. Armstrong, R.P. Lin, S.M. Krimigs, M. Pick, E.C. Roelof, E.T. Sarris, G.M. Simnett, Astron. Astrophys. Suppl. Ser. (1992). https://ui.adsabs.harvard.edu/abs/1992A&AS...92..349L/abstract
G. Lapenta, A.L. Restante, Ann. Geophys. (2008). https://doi.org/10.5194/angeo-26-3049-2008
G. Lapenta, S. Markidis, M.V. Goldman, D.L. Newman, Nat. Phys. (2015). https://doi.org/10.1038/nphys3406
G. Lapenta, F. Pucci, V. Olshevsky, S. Servidio, L. Sorriso-Valvo, D.L. Newman, M.V. Goldman, J. Plasma Phys. (2018). https://doi.org/10.1017/S002237781800003X
A. Lazarian, E.T. Vishniac, Astrophys. J. (1999). https://doi.org/10.1086/307233
A. Lazarian, L. Vlahos, G. Kowal, H. Yan, A. Beresnyak, E.M. de Gouveia Dal Pino, Space Sci. Rev. (2012). https://doi.org/10.1007/s11214-012-9936
A. Lazarian, G.L. Eyink, A. Jafari, G. Kowal, H. Li, S. Xu, E.T. Vishniac, Phys. Plasmas (2020). https://doi.org/10.1063/1.5110603
J.A. le Roux, G.P. Zank, G.M. Webb, O.V. Khabarova, Astrophys. J. (2015). https://doi.org/10.1088/0004-637x/801/2/112
J.A. le Roux, G.P. Zank, G.M. Webb, O.V. Khabarova, Astrophys. J. (2016). https://doi.org/10.3847/0004-637X/827/1/47
J.A. le Roux, G.P. Zank, O.V. Khabarova, Astrophys. J. (2018). https://doi.org/10.3847/1538-4357/aad8b3
J.A. Le Roux, G.M. Webb, O.V. Khabarova, L.-L. Zhao, L. Adhikari, Astrophys. J. (2019). https://doi.org/10.3847/1538-4357/ab521f
J.A. Le Roux, G.M. Webb, O.V. Khabarova, K.T. Van Eck, L.-L. Zhao, L. Adhikari, J. Phys. Conf. Ser. (2020). https://doi.org/10.1088/1742-6596/1620/1/012008
J.-O. Lee, K.-S. Cho, K.-S. Lee, I.-H. Cho, J. Lee, Yu. Miyashita, Y.-H. Kim, R.-S. Kim, S. Jang, Astrophys. J. (2020). https://doi.org/10.3847/1538-4357/ab799a
J. Lemaire, M. Roth, Planet. Space Sci. (1981). https://doi.org/10.1016/0032-0633(81)90075-1
B. Lembege, R. Pellat, Phys. Fluids (1982). https://doi.org/10.1063/1.863677
R.P. Lepping, J.A. Slavin, M. Hesse, J.A. Jones, A. Szabo, J. Geomagn. Geoelectr. (1996). https://doi.org/10.5636/jgg.48.589
G. Li, Astrophys. J. Lett. (2008). https://doi.org/10.1086/525847
Y. Li, J. Lin, Sol. Phys. (2012). https://doi.org/10.1007/s11207-012-9956-1
G. Li, B. Miao, Q. Hu, G. Qin, Phys. Rev. Lett. (2011). https://doi.org/10.1103/PhysRevLett.106.125001
J. Lin, S.R. Cranmer, C.J. Farrugia, J. Geophys. Res. (2008). https://doi.org/10.1029/2008JA013409
J. Lin, N.A. Murphy, Ch. Shen, J.C. Raymond, K.K. Reeves, J. Zhong, N. Wu, Y. Li, Space Sci. Rev. (2015). https://doi.org/10.1007/s11214-015-0209-0
M.G. Linton, J. Geophys. Res. (2006). https://doi.org/10.1029/2006JA011891
M.G. Linton, S.K. Antiochos, Astrophys. J. (2005). https://doi.org/10.1086/429585
M.G. Linton, M.B. Moldwin, J. Geophys. Res. (2009). https://doi.org/10.1029/2008JA013660
M.G. Linton, R.B. Dahlburg, S.K. Antiochos, Astrophys. J. (2001). https://doi.org/10.1086/320974
S. Lion, O. Alexandrova, A. Zaslavsky, Astrophys. J. (2016). https://doi.org/10.3847/0004-637X/824/1/47

Y.D. Liu, Z. Yang, R. Wang, J.G. Luhmann, J.D. Richardson, N. Lugaz, Astrophys. J. Lett. (2014). https://doi.org/10.1088/2041-8205/793/2/L41
H. Liu, Q.-G. Zong, X.-Z. Zhou, J. Geophys. Res. Space Phys. (2016). https://doi.org/10.1002/2016JA022706
G. Lu, S.W.H. Cowley, S.E. Milan, D.G. Sibeck, R.A. Greenwald, T. Moretto, J. Atmos. Sol.-Terr. Phys. (2002). https://doi.org/10.1016/S1364-6826(01)00080-3
S. Lu, Q. Lu, L. Yu, X. Wang, J. Geophys. Res. Space Phys. (2015). https://doi.org/10.1002/2015JA021213
N. Lugaz, I.I. Roussev, J. Atmos. Sol.-Terr. Phys. (2011). https://doi.org/10.1016/j.jastp.2010.08.016
N. Lugaz, M. Temmer, Y. Wang, C.J. Farrugia, Sol. Phys. (2017). https://doi.org/10.1007/s11207-017-1091-6
J.G. Luhmann, N. Gopalswamy, L.K. Jian, N. Lugaz, Sol. Phys. (2020). https://doi.org/10.1007/s11207-020-01624-0
A.T.Y. Lui, C.I. Meng, S.I. Akasofu, Geophys. Res. Lett. (1978). https://doi.org/10.1029/GL005i004p00279
A.T.Y. Lui, B.J. Anderson, K. Takahashi, L.J. Zanetti, R.W. McEntire, T.A. Potemra, R.E. Lopez, D.M. Klumpar, E.M. Greene, R. Strangeway, J. Geophys. Res. (1992). https://doi.org/10.1029/91JA02401
A.T.Y. Lui, D.G. Sibeck, T. Phan, V. Angelopoulos, J. McFadden, C. Carlson, D. Larson, J. Bonnell, K.-H. Glassmeier, S. Frey, Geophys. Res. Lett. (2008). https://doi.org/10.1029/2007GL032933
A.R. Macneil, M.J. Owens, R.T. Wicks, M. Lockwood, S.N. Bentley, M. Lang, Mon. Not. R. Astron. Soc. (2020). https://doi.org/10.1093/mnras/staa951
E.V. Maiewski, R.A. Kislov, O.V. Khabarova, H.V. Malova, V.Yu. Popov, A.A. Petrukovich, L.M. Zelenyi, Astrophys. J. (2020). https://doi.org/10.3847/1538-4357/ab712c
O.E. Malandraki, N.B. Crosby, in *Solar Particle Radiation Storms Forecasting and Analysis*, ed. by O.E. Malandraki, N.B. Crosby. Series: Astrophysics and Space Science Library (Springer, New York, 2018), p. 1. https://www.springer.com/gp/book/9783319600505
O. Malandraki, E.T. Sarris, P. Trochoutsos, Ann. Geophys. (2000). https://doi.org/10.1007/s00585-000-0129-4
O.E. Malandraki, R.G. Marsden, C. Tranquille, R.J. Forsyth, H.A. Elliott, L.J. Lanzerotti, A. Geranios, J. Geophys. Res. (2007). https://doi.org/10.1029/2006JA011876
O.E. Malandraki, R.G. Marsden, C. Tranquille, R.J. Forsyth, H.A. Elliot, A. Geranios, Ann. Geophys. (2008). https://doi.org/10.5194/angeo-26-1029-2008
O. Malandraki, O. Khabarova, R. Bruno, G.P. Zank, G. Li, B. Jackson, M.M. Bisi, A. Greco, O. Pezzi, W. Matthaeus, A.G. Chasapis, S. Servidio, H. Malova, R. Kislov, F. Effenberger, J. le Roux, Y. Chen, Q. Hu, E. Engelbrecht, Astrophys. J. (2019). https://doi.org/10.3847/1538-4357/ab289a
F. Malara, L. Primavera, P. Veltri, J. Geophys. Res. (1996). https://doi.org/10.1029/96JA01637
H.V. Malova, V.Yu. Popov, E.E. Grigorenko, A.A. Petrukovich, D. Delcourt, A.S. Sharma, O.V. Khabarova, L.M. Zelenyi, Astrophys. J. (2017). https://doi.org/10.3847/1538-4357/834/1/34
Kh.V. Malova, V.Yu. Popov, O.V. Khabarova, E.E. Grigorenko, A.A. Petrukovich, L.M. Zelenyi, Cosm. Res. (2018). https://doi.org/10.1134/S0010952518060060
W. Manchester IV, B. Van Der Holst, J. Phys. (2017). https://doi.org/10.1088/1742-6596/900/1/012015
F. Mariani, B. Bavassano, U. Villante, N.F. Ness, J. Geophys. Res. (1973). https://doi.org/10.1029/JA078i034p08011
S. Markidis, P. Henri, G. Lapenta, A. Divin, M. Goldman, D. Newman, E. Laure, Phys. Plasmas (2013). https://doi.org/10.1063/1.4817286
Y. Matsumoto, T. Amano, T.N. Kato, M. Hoshino, Science (2015). https://doi.org/10.1126/science.1260168
W.H. Matthaeus, S.L. Lamkin, Phys. Fluids (1985). https://doi.org/10.1063/1.865147
W.H. Matthaeus, S.L. Lamkin, Phys. Fluids (1986). https://doi.org/10.1063/1.866004
W.H. Matthaeus, J.J. Ambrosiano, M.L. Goldstein, Phys. Rev. Lett. (1984). https://doi.org/10.1103/PhysRevLett.53.1449
W.H. Matthaeus, M. Wan, S. Servidio, A. Greco, K.T. Osman, S. Oughton, P. Dmitruk, Philos. Trans. R. Soc. A (2015). https://doi.org/10.1098/rsta.2014.0154
J.C. Maxwell, Philos. Mag. (1861). https://doi.org/10.1080/14786431003659180
D.J. McComas, J.T. Gosling, J.L. Phillips, S.J. Bame, J. Geophys. Res. (1989). https://doi.org/10.1029/JA094iA06p06907
D.J. McComas, J.T. Gosling, J.L. Phillips, J. Geophys. Res. (1992). https://doi.org/10.1029/91JA02370
D.J. McComas, J.T. Gosling, C.M. Hammond, M.B. Moldwin, J.L. Phillips, R.J. Forsyth, J. Geophys. Res. (1994). https://doi.org/10.1029/94GL01077
R.L. McNutt Jr., Rev. Geophys. Suppl. (1991). https://ui.adsabs.harvard.edu/abs/1991RvGeo..29S.985M/abstract
V.G. Merkin, J.G. Lyon, S.L. McGregor, D.M. Pahud, Geophys. Res. Lett. (2011). https://doi.org/10.1029/2011GL047822
B. Miao, B. Peng, G. Li, Ann. Geophys. (2011). https://doi.org/10.5194/angeo-29-237-2011

A.V. Milovanov, L.M. Zelenyi, in *Solar System Plasmas in Space and Time*, ed. by J.L. Burch, J.H. Waite (AGU, Washington DC, 1994), p. 43
A.V. Milovanov, L.M. Zelenyi, Astrophys. Space Sci. (1999). https://doi.org/10.1023/A:1002450525201
O.V. Mingalev, O.V. Khabarova, H.V. Malova, I.V. Mingalev, R.A. Kislov, M.N. Mel'nik, P.V. Setsko, L.M. Zelenyi, G.P. Zank, Sol. Syst. Res. (2019). https://doi.org/10.1134/S0038094619010064
M.B. Moldwin, W.J. Hughes, J. Geophys. Res. (1991). https://doi.org/10.1029/91JA01167
M.B. Moldwin, J.L. Phillips, J.T. Gosling, E.E. Scime, D.J. MacComas, S.J. Bame, A. Balogh, R.J. Forsyth, J. Geophys. Res. (1995). https://doi.org/10.1029/95JA01123
A.L. Moser, P.M. Bellan, Nature (2012). https://doi.org/10.1038/nature10827
T. Mulligan, A.A. Reinard, B.J. Lynch, J. Geophys. Res. Space Phys. (2013). https://doi.org/10.1002/jgra.50101
P.A. Muñoz, J. Büchner, Astrophys. J. (2018). https://doi.org/10.3847/1538-4357/aad5e9
T. Murata, H. Matsumoto, H. Kojima, A. Fujita, T. Nagai, T. Yamamoto, R.R. Anderson, Geophys. Res. Lett. (1995). https://doi.org/10.1029/95GL01514
Z.E. Musielak, S.T. Suess, Astrophys. J. (1988). https://doi.org/10.1086/166483
R. Nakamura, W. Baumjohann, Y. Asano, A. Runov, A. Balogh, C.J. Owen, A.N. Fazakerley, M. Fujimoto, B. Klecker, H. Reme, J. Geophys. Res. Space Phys. (2006). https://doi.org/10.1029/2006JA011706
N.F. Ness, J. Geophys. Res. (1965). https://doi.org/10.1029/JZ070i013p02989
N.F. Ness, L.F. Burlaga, J. Geophys. Res. (2001). https://doi.org/10.1029/2000JA000118
M.B. Niedner Jr., J.C. Brandt, Astrophys. J. (1978). https://ui.adsabs.harvard.edu/abs/1978ApJ...223..655N/abstract
K. Nishida, N. Nishizuka, K. Shibata, Astrophys. J. Lett. (2013). https://doi.org/10.1088/2041-8205/775/2/L39
M. Nosé, A.T.Y. Lui, S. Ohtani, B.H. Mauk, R.W. McEntire, D.J. Williams, T. Mukai, K. Yumoto, J. Geophys. Res. (2000). https://doi.org/10.1029/1999JA000318
D. Odstrcil, Adv. Space Res. (2003). https://doi.org/10.1016/S0273-1177(03)00332-6
D. Odstrčil, V.J. Pizzo, J. Geophys. Res. (1999). https://doi.org/10.1029/1998JA900019
J.S. Oishi, M.-M. Mac Low, D.C. Collins, M. Tamura, Astrophys. J. Lett. (2015). https://doi.org/10.1088/2041-8205/806/1/L12
M. Oka, T. Obara, N.V. Nitta, S. Yashiro, D. Shiota, K. Ichimoto, Earth Planets Space (2021). https://doi.org/10.1186/s40623-021-01362-y
D.M. Oliveira, A.A. Samsonov, Adv. Space Res. (2018). https://doi.org/10.1016/j.asr.2017.10.006
W.P. Olsen, Adv. Space Res. (1982). https://doi.org/10.1016/0273-1177(82)90084-9
S. Oughton, W.H. Matthaeus, P. Dmitruk, Astrophys. J. (2017). https://doi.org/10.3847/1538-4357/aa67e2
M.J. Owens, Sol. Phys. (2009). https://doi.org/10.1007/s11207-009-9442-6
M. Owens, N. Crooker, M. Lockwood, J. Geophys. Res. (2013). https://doi.org/10.1002/jgra.50259
C. Pagel, N.U. Crooker, D.E. Larson, Geophys. Res. Lett. (2005). https://doi.org/10.1029/2005GL023043
E.V. Panov, J. Buchner, M. FräNz, A. Korth, S.P. Savin, H. RèMe, K.-H. FornaçOn, J. Geophys. Res. Space Phys. (2008). https://doi.org/10.1029/2006JA012123
E. Parker, Astrophys. J. (1958). https://doi.org/10.1086/146579
E.N. Parker, Astrophys. J. (1979). https://doi.org/10.1086/157150
E.I. Parkhomenko, H.V. Malova, E.E. Grigorenko, V.Yu. Popov, A.A. Petrukovich, D.C. Delcourt, E.A. Kronberg, P.W. Daly, L.M. Zelenyi, Phys. Plasmas (2019). https://doi.org/10.1063/1.5082715
E.G. Pavlos, O.E. Malandraki, O.V. Khabarova, L.P. Karakatsanis, G.P. Pavlos, G. Livadiotis, Entropy (2019). https://doi.org/10.3390/e21070648
F. Pecora, A. Greco, Q. Hu, S. Servidio, A. Chasapis, W.H. Matthaeus, Astrophys. J. Lett. (2019). https://doi.org/10.3847/2041-8213/ab32d9
F. Pecora, S. Servidio, A. Greco, W.H. Matthaeus, Astron. Astrophys. (2021). https://doi.org/10.1051/0004-6361/202039639
O. Pezzi, F. Malara, S. Servidio, F. Valentini, T.N. Parashar, W.H. Matthaeus, P. Veltri, Phys. Rev. (2017). https://doi.org/10.1103/PhysRevE.96.023201
O. Pezzi, S. Servidio, D. Perrone, F. Valentini, L. Sorriso-Valvo, A. Greco, W.H. Matthaeus, P. Veltri, Phys. Plasmas (2018). https://doi.org/10.1063/1.5027685
O. Pezzi, Y. Yang, F. Valentini, S. Servidio, A. Chasapis, W.H. Matthaeus, P. Veltri, Phys. Plasmas (2019). https://doi.org/10.1063/1.5100125
V.J. Pizzo, J. Geophys. Res. (1982). https://doi.org/10.1029/JA087iA06p04374
V.J. Pizzo, J. Geophys. Res. (1994). https://doi.org/10.1029/93ja03474
J.J. Podesta, J. Geophys. Res. (2017). https://doi.org/10.1002/2016JA023629
A.S. Potapov, Astrophys. Space Sci. (2018). https://doi.org/10.1007/s10509-018-3304-3
L. Primavera, F. Malara, S. Servidio, G. Nigro, P. Veltri, Astrophys. J. (2019). https://doi.org/10.3847/1538-4357/ab29f5

F. Pucci, S. Servidio, L. Sorriso-Valvo, V. Olshevsky, W.H. Matthaeus, F. Malara, M.V. Goldman, D.L. Newman, G. Lapenta, Astrophys. J. (2017). https://doi.org/10.3847/1538-4357/aa704f
F. Pucci, W.H. Matthaeus, A. Chasapis, S. Servidio, L. Sorriso-Valvo, V. Olshevsky, D.L. Newman, M.V. Goldman, G. Lapenta, Astrophys. J. (2018). https://doi.org/10.3847/1538-4357/aadd0a
K.P. Raju, B.J.I. Bromage, S.A. Chapman, G. Del Zanna, Astron. Astrophys. (2005). https://doi.org/10.1051/0004-6361:20042179
R. Ramstad, D.A. Brain, Y. Dong et al., Nat. Astron. (2020). https://doi.org/10.1038/s41550-020-1099-y
A.F. Rappazzo, W.H. Matthaeus, D. Ruffolo, M. Velli, S. Servidio, Astrophys. J. (2017). https://doi.org/10.3847/1538-4357/aa79f2
M. Riazantseva, V. Budaev, L. Rakhmanova, G. Zastenker, Yu. Yermolaev, I. Lodkina, J. Šafránková, Z. Němeček, L. Přech, J. Plasma Phys. (2017). https://doi.org/10.1017/S0022377817000502
J.D. Richardson, J. Atmos. Sol.-Terr. Phys. (2011). https://doi.org/10.1016/j.jastp.2010.06.005
I.G. Richardson, Living Rev. Sol. Phys. (2018). https://doi.org/10.1007/s41116-017-0011-z
J.D. Richardson, E.C. Stone, A.C. Cummings et al., Geophys. Res. Lett. (2006). https://doi.org/10.1029/2006GL027578
P. Riley, J. Atmos. Sol.-Terr. Phys. (2007). https://doi.org/10.1016/j.jastp.2006.06.008
P. Riley, J.A. Linker, Z. Mikic, J. Geophys. Res. (2002). https://doi.org/10.1029/2001JA000299
D.A. Roberts, P.A. Keiter, M.L. Goldstein, J. Geophys. Res. (2005). https://doi.org/10.1029/2004JA010541
N. Romanova, V. Pilipenko, Acta Geophys. (2009). https://doi.org/10.2478/s11600-008-0064-4
N. Romanova, V. Pilipenko, N. Crosby, O. Khabarova, Bulg. J. Phys. **34**, 2 (2007). http://citeseerx.ist.psu.edu/viewdoc/summary?doi=10.1.1.574.5774
E. Romashets, M. Vandas, I.S. Veselovsky, J. Atmos. Sol.-Terr. Phys. (2010). https://doi.org/10.1016/j.jastp.2010.10.010
Z.J. Rong, S. Barabash, Y. Futaana, G. Stenberg, T.L. Zhang, W.X. Wan, Y. Wei, X.-D. Wang, L.H. Chai, J. Zhong, J. Geophys. Res. Space Phys. (2014). https://doi.org/10.1002/2014JA020461
Z.J. Rong, S. Barabash, G. Stenberg et al., J. Geophys. Res. (2015). https://doi.org/10.1002/2014JA020973
M. Ruderman, COSPAR Colloq. Ser. (1990). https://doi.org/10.1016/B978-0-08-040780-7.50046-4
M.S. Ruderman, Phys. Plasmas (1998). https://doi.org/10.1063/1.872927
A. Runov, V. Sergeev, R. Nakamura et al., Geophys. Res. Lett. (2003). https://doi.org/10.1029/2002GL016730
A. Runov, V. Sergeev, R. Nakamura et al., Planet. Space Sci. (2005). https://doi.org/10.1016/j.pss.2004.09.049
V.A. Runov, R. Sergeev, W. Nakamura et al., Ann. Geophys. (2006). https://doi.org/10.5194/angeo-24-247-2006
C.T. Russell, T. Mulligan, Adv. Space Res. (2002). https://doi.org/10.1016/S0273-1177(01)00588-9
M. Ryutova, in *Physics of Magnetic Flux Tubes*. Astrophysics and Space Science Library, vol. 455 (Springer, Switzerland, 2018), pp. 1–349. https://ui.adsabs.harvard.edu/abs/2018ASSL..455.....R/abstract
C. Sauty, K. Tsinganos, Astron. Astrophys. (1994). https://ui.adsabs.harvard.edu/abs/1994A&A...287..893S
K.H. Schatten, Rev. Geophys. Space Phys. (1971). https://doi.org/10.1029/RG009i003p00773
K. Schindler, in *A Self-Consistent Theory of the Tail of the Magnetosphere in Earth's Magnetospheric Processes*, ed. by B.M. McCormac. Astrophysics and Space Science Library, vol. 32 (Springer, Dordrecht, 1972), p. 200. https://doi.org/10.1007/978-94-010-2896-7_21
S.J. Schwartz, R.L. Kessel, C.C. Brown, L.J.C. Woolliscroft, M.W. Dunlop, Ch.J. Farrugia, D.S. Hall, J. Geophys. Res. (1988). https://doi.org/10.1029/JA093iA10p11295
S.J. Schwartz, E. Henley, J. Mitchell, V. Krasnoselskikh, Phys. Rev. Lett. (2011). https://doi.org/10.1103/PhysRevLett.107.215002
V. Sergeev, D. Mitchell, C. Russell, D. Williams, J. Geophys. Res. (1993). https://doi.org/10.1029/93JA01151
V.A. Sergeev, T.I. Pulkkinen, R.J. Pellinen, J. Geophys. Res. (1996). https://doi.org/10.1029/95JA03192
S. Servidio, W.H. Matthaeus, M.A. Shay, P.A. Cassak, P. Dmitruk, Phys. Rev. Lett. (2009). https://doi.org/10.1103/PhysRevLett.102.115003
S. Servidio, F. Valentini, D. Perrone, A. Greco, F. Califano, W. Matthaeus, P. Veltri, J. Plasma Phys. (2015). https://doi.org/10.1017/S0022377814000841
A.S. Sharma, R. Nakamura, A. Runov et al., Ann. Geophys. (2008). https://doi.org/10.5194/angeo-26-955-2008
C. Shen, X. Li, M. Dunlop, Q.Q. Shi, Z.X. Liu, E. Lucek, Z.Q. Chen, J. Geophys. Res. (2007). https://doi.org/10.1029/2005JA011584
F. Shen, Yu. Wang, C. Shen, X. Feng, Sol. Phys. (2019). https://doi.org/10.1007/s11207-017-1129-9
Q.Q. Shi, M.D. Hartinger, V. Angelopoulos et al., J. Geophys. Res. (2014). https://doi.org/10.1002/2013JA019551
D. Shiota, R. Kataoka, Space Weather (2016). https://doi.org/10.1002/2015SW001308
D. Shiota, R. Kataoka, Y. Miyoshi et al., Space Weather (2014). https://doi.org/10.1002/2013SW000989

K.D.C. Simunac, A.B. Galvin, C.J. Farrugia et al., Sol. Phys. **281**, 423 (2012). https://doi.org/10.1007/s11207-012-0156-9
G. Siscoe, D. Odstrcil, J. Geophys. Res. (2008). https://doi.org/10.1029/2008JA013142
G.L. Siscoe, N.U. Crooker, G.M. Erickson, B.U.O. Sonnerup, K.D. Siebert, D.R. Weimer, W.W. White, N.C. Maynard, in *Global Geometry of Magnetospheric Currents Inferred from MHD Simulations Magnetospheric Current Systems*, ed. by Sh.-I. Ohtani, R. Fujii, M. Hesse, R.L. Lysak. Geophysical Monograph, vol. 118 (American Geophysical Union, Washington DC, 2000), p. 41. https://doi.org/10.1029/GM118p0041
T. Siversky, V. Zharkova, J. Plasma Phys. (2009). https://doi.org/10.1017/S0022377809008009
J.A. Slavin, Adv. Space Res. (2004). https://doi.org/10.1016/j.asr.2003.02.019
J.A. Slavin, S.M. Krimigis, M.H. Acuña et al., Space Sci. Rev. (2007). https://doi.org/10.1007/s11214-007-9154-x
J.A. Slavin, M.H. Acuña, B.J. Anderson et al., Science (2008). https://doi.org/10.1126/science.1159040
V.A. Slemzin, F.F. Goryaev, D.G. Rodkin, Yu.S. Shugay, S.V. Kuzin, Plasma Phys. Rep. (2019). https://doi.org/10.1134/S1063780X19100076
J. Slough, G. Votroubek, C. Pihl, Nucl. Fusion (2011). https://doi.org/10.1088/0029-5515/51/5/053008
M. Snow, J.C. Brandt, Y. Yi, C.C. Petersen, H. Mikuz, Planet. Space Sci. (2004). https://doi.org/10.1016/j.pss.2003.10.001
B.V. Somov, in *Plasma Astrophysics*, ed. by S.N. Shore. Astrophysics and Space Science Library, vol. 341 (Springer, New York, 2006), p. 223. https://doi.org/10.1007/978-0-387-68894-7_14
B.V. Somov, T. Kosugi, Astrophys. J. (1997). https://doi.org/10.1086/304449
C.P. Sonett, I.J. Abrams, The distant geomagnetic field. 3. Disorder and shocks in the magnetopause. J. Geophys. Res. **68**(5), 1233–1263 (1963)
H.-Q. Song, Y. Chen, G. Li, X.-L. Kong, Sh-W. Feng, Phys. Rev. X (2012). https://doi.org/10.1103/PhysRevX.2.021015
B.U.Ö. Sonnerup, M. Guo, Geophys. Res. Lett. (1996). https://doi.org/10.1029/96GL03573
A.M. Sorba, N.A. Achilleos, P. Guio, C.S. Arridge, N. Sergis, M.K. Dougherty, J. Geophys. Res. (2018). https://doi.org/10.1029/2018JA025764
L. Sorriso-Valvo, D. Perrone, O. Pezzi, F. Valentini, S. Servidio, I. Zouganelis, P. Veltri, J. Plasma Phys. (2018). https://doi.org/10.1017/S0022377818000302
A.K. Srivastava, S.K. Mishra, P. Jelínek, Astrophys. J. (2019). https://doi.org/10.3847/1538-4357/ab4a0c
K. Steed, C.J. Owen, P. Démoulin, S. Dasso, J. Geophys. Res. (2011). https://doi.org/10.1029/2010JA015940
J.E.H. Stevenson, C.E. Parnell, E.R. Priest, A.L. Haynes, Astron. Astrophys. (2015). https://doi.org/10.1051/0004-6361/201424348
Š. Štverák, M. Maksimovic, P.M. Trávníček et al., J. Geophys. Res. (2009). https://doi.org/10.1029/2008JA013883
S.T. Suess, J. Geophys. Res. **93**(A6), 5437–5445 (1988). https://doi.org/10.1029/JA093iA06p05437
S.T. Suess, Y.-K. Ko, R. von Steiger, R.L. Moore, J. Geophys. Res. (2009). https://doi.org/10.1029/2008JA013704
X. Sun, T.P. Intrator, L. Dorf, J. Sears, I. Furno, G. Lapenta, Phys. Rev. Lett. (2010). https://doi.org/10.1103/PhysRevLett.105.255001
R. Susino, A. Bemporad, S. Krucker, Astrophys. J. (2013). https://doi.org/10.1088/0004-637X/777/2/93
L. Svalgaard, J.M. Wilcox, Sol. Phys. (1975). https://doi.org/10.1007/BF00154083
Sh. Takasao, A. Asai, H. Isobe, K. Shibata, Astrophys. J. (2016). https://doi.org/10.3847/0004-637X/828/2/103
T. Tamano, Sol. Phys. (1991). https://doi.org/10.1007/BF00148747
L.C. Tan, Astrophys. J. (2020). https://doi.org/10.3847/1538-4357/abb086
B.B. Tang, X.C. Guo, C. Wang, Y.Q. Hu, J.R. Kan, J. Geophys. Res. (2009). https://doi.org/10.1029/2009JA014325
W.-L. Teh, S. Eriksson, B.U.Ö. Sonnerup et al., Geophys. Res. Lett. (2010). https://doi.org/10.1029/2010GL045056
A. Tenerani, A.F. Rappazzo, M. Velli, F. Pucci, Astrophys. J. (2015). https://doi.org/10.1088/0004-637X/801/2/145
J.A. Tessein, W.H. Matthaeus, M. Wan, K.T. Osman, D. Ruffolo, J. Giacalone, Astrophys. J. Lett. (2013). https://doi.org/10.1088/2041-8205/776/1/L8
J.A. Tessein, D. Ruffolo, W.H. Matthaeus, M. Wan, J. Giacalone, M. Neugebauer, Astrophys. J. (2015). https://doi.org/10.1088/0004-637X/812/1/68
M. Tokumaru, Proc. Jpn. Acad. Ser. B (2013). https://doi.org/10.2183/pjab.89.67
M. Tokumaru, M. Kojima, K. Fujiki, M. Yamashita, A. Yokobe, J. Geophys. Res. (2003). https://doi.org/10.1029/2002JA009574
M. Tokumaru, D. Satonaka, K. Fujiki et al., Sol. Phys. (2017). https://doi.org/10.1007/s11207-017-1066-7

T. Török, B. Kliem, Astrophys. J. (2005). https://doi.org/10.1086/462412
L. Trenchi, R. Bruno, R. D'Amicis, M.F. Marcucci, D. Telloni, Ann. Geophys. (2013). https://doi.org/10.5194/angeo-31-1333-2013
D.A. Uzdensky, R.M. Kulsrud, Phys. Plasmas (2000). https://doi.org/10.1063/1.1308081
D.A. Uzdensky, N.F. Loureiro, Phys. Rev. Lett. (2016). https://doi.org/10.1103/PhysRevLett.116.105003
A. Vaivads, G. Andersson, S.D. Bale et al., Exp. Astron. (2012). https://doi.org/10.1007/s10686-011-9233-6
F. Valentini, D. Perrone, S. Stabile et al., New J. Phys. (2016). https://doi.org/10.1088/1367-2630/18/12/125001
J.A. Van Allen, W.Ch. Lin, J. Geophys. Res. (1960). https://doi.org/10.1029/JZ065i009p02998
B. Van Compernolle, W. Gekelman, Phys. Plasmas (2012). https://doi.org/10.1063/1.4755949
M. Vandas, E. Romashets, A. Geranios, Ann. Geophys. (2010). https://doi.org/10.5194/angeo-28-1581-2010
I.Y. Vasko, H.V. Malova, A.V. Artemyev, L.M. Zelenyi, Planet. Space Sci. (2012). https://doi.org/10.1016/j.pss.2012.09.010
I.Y. Vasko, A.V. Artemyev, V.Y. Popov, H.V. Malova, Phys. Plasmas (2013). https://doi.org/10.1063/1.4792263
O.P. Verkhoglyadova, G.P. Zank, G. Li, Phys. Rep. (2015). https://doi.org/10.1016/j.physrep.2014.10.004
S.N. Vernov, I.A. Savenko, P.I. Shavrin, Geomagn. Aeron. (1962). https://doi.org/10.1016/0032-0633(63)90080-1
I.S. Veselovsky, A.N. Zhukov, O.A. Panasenco, Sol. Syst. Res. (2002). https://doi.org/10.1023/A:1014281729043
M.R. Voelzke, Earth Moon Planets (2005). https://doi.org/10.1007/s11038-006-9073-y
M. Volwerk, G.H. Jones, T. Broiles et al., J. Geophys. Res. (2017). https://doi.org/10.1002/2017JA023861
B. Vršnak, G. Poletto, E. Vujić et al., Astron. Astrophys. (2009). https://doi.org/10.1051/0004-6361/200810844
F.L. Waelbroeck, Nucl. Fusion (2009). https://doi.org/10.1088/0029-5515/49/10/104025
M. Wan, W.H. Matthaeus, S. Servidio, S. Oughton, Phys. Plasmas (2013). https://doi.org/10.1063/1.4945631
M. Wan, A.F. Rappazzo, W.H. Matthaeus, S. Servidio, S. Oughton, Astrophys. J. (2014). https://doi.org/10.1088/0004-637X/797/1/63
Y.-M. Wang, N.R. Sheeley, Astrophys. J. (1990). https://doi.org/10.1086/168805
Y.M. Wang, N.R. Sheeley, Astrophys. J. (1992). https://doi.org/10.1086/171430
S. Wang, L.C. Lee, C.Q. Wei, S.-I. Akasofu, Sol. Phys. (1988). https://doi.org/10.1007/BF00148579
S. Wang, Y.F. Liu, H.N. Zheng, Sol. Phys. (1997). https://doi.org/10.1023/A:1004959828537
Y. Wang, B. Wang, C. Shen, F. Shen, N. Lugaz, J. Geophys. Res. (2014). https://doi.org/10.1002/2013JA019537
J.M. Wang, H.Q. Feng, G.Q. Zhao, Astrophys. J. (2018). https://doi.org/10.3847/1538-4357/aaa131
D.F. Webb, T.A. Howard, Sol. Phys. (2012). https://doi.org/10.12942/lrsp-2012-3
D.F. Webb, J. Burkepile, T.G. Forbes, P. Riley, J. Geophys. Res. (2003). https://doi.org/10.1029/2003JA009923
E.J. Weber, L. Davis Jr., Astrophys. J. (1967). https://doi.org/10.1086/149138
S. Wedemeyer-Böhm, E. Scullion, O. Steiner, L.R. van der Voort, J. de la Cruz Rodriguez, V. Fedun, R. Erdélyi, Nature (2012). https://doi.org/10.1038/nature11202
G.R. Werner, D.A. Uzdensky, M.C. Begelman, B. Cerutti, K. Nalewajko, Mon. Not. R. Astron. Soc. (2018). https://doi.org/10.1093/mnras/stx2530
J.M. Wilcox, Space Sci. Rev. (1968). https://doi.org/10.1007/BF00227565
J.M. Wilcox, N.F. Ness, J. Geophys. Res. (1965). https://doi.org/10.1029/JZ070i023p05793
J.M. Wilcox, P.H. Scherrer, J.T. Hoeksema, Science (1980). https://doi.org/10.1126/science.209.4456.603
D.M. Willis, Rev. Geophys. (1971). https://doi.org/10.1029/RG009i004p00953
D. Winterhalter, E.J. Smith, M.E. Burton, D.J. McComas, J. Geophys. Res. (1994). https://doi.org/10.1029/93JA03481
A.M. Wold, M.L. Mays, A. Taktakishvili, L.K. Jian, D. Odstrcil, P. MacNeice, J. Space Weather Space Clim. (2018). https://doi.org/10.1051/swsc/2018005
J.R. Wygant, C.A. Cattell, R. Lysak et al., J. Geophys. Res. (2005). https://doi.org/10.1029/2004JA010708
Q. Xia, V. Zharkova, Astron. Astrophys. (2018). https://doi.org/10.1051/0004-6361/201833599
Q. Xia, V. Zharkova, Astron. Astrophys. (2020). https://doi.org/10.1051/0004-6361/201936420
X. Xu, F. Wei, X. Feng, J. Geophys. Res. (2011). https://doi.org/10.1029/2010JA016159
M. Yamauchi, A.T.Y. Lui, Phys. Plasmas (1997). https://doi.org/10.1063/1.872600
Z.H. Yao, D. Grodent, L.C. Ray et al., J. Geophys. Res. (2017). https://doi.org/10.1002/2017JA024060
A.R. Yeates, A.J.B. Russell, G. Hornig, Proc. R. Soc. (2015). https://doi.org/10.1098/rspa.2015.0012
Yu.I. Yermolaev, M.Yu. Yermolaev, G.N. Zastenker, L.M. Zelenyi, A.A. Petrukovich, J.-A. Sauvau, Planet. Space Sci. (2005). https://doi.org/10.1016/j.pss.2004.09.044

Y. Yi, J.C. Brandt, C.E. Randall, M. Snow, Astron. J. (1994). https://ui.adsabs.harvard.edu/abs/1994AJ....107.1591Y/abstract
Y. Yi, R.J. Walker, T. Ogino, J.C. Brandt, J. Geophys. Res. (1996). https://ui.adsabs.harvard.edu/abs/1996JGR...10127585Y/abstract
G.P. Zank, J.A. le Roux, G.M. Webb, A. Dosch, O. Khabarova, Astrophys. J. (2014). https://doi.org/10.1088/0004-637X/797/1/28
G.P. Zank, P. Hunana, P. Mostafavi et al., Astrophys. J. (2015). https://doi.org/10.1088/0004-637X/814/2/137
L. Zelenyi, A. Artemyev, in *Microphysics of Cosmic Plasmas*, ed. by A. Balogh, A. Bykov, P. Cargill, R. Dendy, T. Dudok de Wit, J. Raymond. Space Sciences Series of ISSI (Springer, Boston, 2013), p. 365. https://doi.org/10.1007/978-1-4899-7413-6_14
L.M. Zelenyi, A.V. Milovanov, Sov. Astron. (1992). https://ui.adsabs.harvard.edu/abs/1992SvA....36...74Z/abstract
L.M. Zelenyi, A.V. Milovanov, Phys. Usp. (2004). https://doi.org/10.1070/PU2004v047n08ABEH001705
L. Zelenyi, O. Vaisberg, Cosm. Res. **20**, 604 (1982). https://ui.adsabs.harvard.edu/abs/1982KosIs..20..604Z/abstract
L.M. Zelenyi, D. Delcourt, H.V. Malova, A.S. Sharma, V.Yu. Popov, A.A. Bykov, Adv. Space Res. (2002). https://doi.org/10.1016/S0273-1177(02)00427-1
L.M. Zelenyi, H.V. Malova, V.Yu. Popov, D. Delcourt, A.S. Sharma, Nonlinear Process. Geophys. (2004). https://doi.org/10.5194/npg-11-579-2004
L. Zelenyi, A. Artemyev, H. Malova, A.V. Milovanov, G. Zimbardo, Phys. Lett. A (2008a). https://doi.org/10.1016/j.physleta.2008.08.035
L. Zelenyi, A. Artemiev, H. Malova, V. Popov, J. Atmos. Sol.-Terr. Phys. (2008b). https://doi.org/10.1016/j.jastp.2007.08.019
L.M. Zelenyi, Kh.V. Malova, A.V. Artemyev, V.Yu. Popov, A.A. Petrukovich, Plasma Phys. Rep. (2011). https://doi.org/10.1134/S1063780X1102005X
L. Zelenyi, H. Malova, E. Grigorenko, V. Popov, Phys. Usp. (2016). https://doi.org/10.3367/UFNe.2016.09.037923
L. Zelenyi, H. Malova, E. Grigorenko, V. Popov, D. Delcourt, Plasma Phys. Control. Fusion (2019). https://doi.org/10.1088/1361-6587/aafbbf
L.M. Zelenyi, H.V. Malova, E.E. Grigorenko, V.Yu. Popov, E.M. Dubinin, Geophys. Res. Lett. (2020). https://doi.org/10.1029/2020GL088422
T.L. Zhang, C.T. Russell, W. Zambelli, Z. Vörös, C. Wang, J.B. Cao, L.K. Jian, R.J. Strangeway, M. Balikhin, W. Baumjohann, M. Delva, M. Volwerk, K.-H. Glassmeier, Geophys. Res. Lett. (2008). https://doi.org/10.1029/2008GL036120
T.L. Zhang, W. Baumjohann, W.L. Teh, R. Nakamura, C.T. Russell, J.G. Luhmann, K.H. Glassmeier, E. Dubinin, H.Y. Wei, A.M. Du, Q.M. Lu, S. Wang, M. Balikhin, Geophys. Res. Lett. (2012a). https://doi.org/10.1029/2012GL054236
T.L. Zhang, Q.M. Lu, W. Baumjohann et al., Science (2012b). https://doi.org/10.1126/science.1217013
X.-J. Zhang, Q. Ma, A.V. Artemyev, W. Li, W.S. Kurth, B.H. Mauk, G. Clark, F. Allegrini, D.J. Gershman, S.J. Bolton, J. Geophys. Res. (2020). https://doi.org/10.1029/2020JA027957
L.-L. Zhao, G.P. Zank, O.V. Khabarova, S. Du, Y. Chen, L. Adhikari, Q. Hu, Astrophys. J. (2018). https://doi.org/10.3847/2041-8213/aaddf6
L.-L. Zhao, G.P. Zank, L. Adhikari et al., Astrophys. J. Suppl. Ser. (2020). https://doi.org/10.3847/1538-4365/ab4ff1
V.V. Zharkova, M. Gordovskyy, Astrophys. J. (2004). https://doi.org/10.1086/381966
V.V. Zharkova, M. Gordovskyy, Space Sci. Rev. (2005). https://doi.org/10.1007/s11214-006-6027-7
V. Zharkova, O. Khabarova, Astrophys. J. (2012). https://doi.org/10.1088/0004-637X/752/1/35
V. Zharkova, O. Khabarova, Ann. Geophys. (2015). https://doi.org/10.5194/angeo-33-457-2015
V. Zharkova, Q. Xia, Astron. Astrophys. (2021). https://doi.org/10.1051/0004-6361/202039220
V. Zhdankin, D.A. Uzdensky, J.C. Perez, S. Boldyrev, Astrophys. J. (2013). https://doi.org/10.1088/0004-637X/771/2/124
J. Zheng, Q. Hu, Astrophys. J. (2018). https://doi.org/10.3847/2041-8213/aaa3d7
G.P. Zhou, C.J. Xiao, J.X. Wang, M.S. Wheatland, H. Zhao, Astron. Astrophys. (2011). https://doi.org/10.1051/0004-6361/201015726
X. Zhou, J. Büchner, M. Bárta, W. Gan, S. Liu, Astrophys. J. (2015). https://doi.org/10.1088/0004-637X/815/1/6
M. Zhou, P. Bhat, N.F. Loureiro, D.A. Uzdensky, Phys. Rev. Res. (2019). https://doi.org/10.1103/PhysRevResearch.1.012004
P. Zhu, Z. Wang, J. Chen, X. Yan, R. Liu, Ann. Geophys. (2019). https://doi.org/10.5194/angeo-37-325-2019
A.N. Zhukov, I.S. Veselovsky, S. Koutchmy, C. Delannée, Astron. Astrophys. (2000). https://ui.adsabs.harvard.edu/abs/2000A&A...353..786Z/abstract

G. Zimbardo, J. Geophys. Res. (1989). https://doi.org/10.1029/JA094iA07p08707
Q.-G. Zong, B. Wilken, G.D. Reeves et al., J. Geophys. Res. (1997). https://doi.org/10.1029/97JA00076
E.G. Zweibel, M. Yamada, Proc. R. Soc. A (2016). https://doi.org/10.1098/rspa.2016.0479